NTNU
Norwegian University of
Science and Technology

Validation of Nonlinear Hydrodynamic Load Models for a Monopile in Long-Crested Waves

Pratim Jayesh Patel

Marine Technology
Submission date: June 2018
Supervisor: Erin Bachynski, IMT

Norwegian University of Science and Technology
Department of Marine Technology

Preface

This Master Thesis has been written during the Spring semester 2018 at the Department of Marine Technology, NTNU. The Master Thesis marks the culmination of my M.Sc. in Marine Technology, with a specialization in hydrodynamics. The thesis has been carried out in cooperation with Department of Marine Technology and the NOWITECH project, and has been supervised by Associate Professor Erin Bachynski.

The topic for the thesis is dynamics of offshore wind turbines with monopile support, which is a topic that is highly relevant at time of writing as the offshore wind industry is rapidly growing. This topic has involved work within the areas marine hydrodynamics and marine structures, which are usually closely related. The reader of this Master Thesis is therefore assumed to be familiar with hydrodynamics, or fluid dynamics, statistical methods and structural dynamics.

Both experimental test results, which were provided by the NOWITECH project, and simulations with the computer software SIMA RIFLEX have been treated in this work. This has at times been very demanding as the amount of data to be treated has been overwhelming. However, looking back at the experience, it has been very rewarding and given me a great learning outcome. I have obtained new insight into the topics of this Master Thesis that I am sure can be applied to many related applications, and will be valuable in working life.

Trondheim, 11 June 2018

Pratim Patel

Pratim Jayesh Patel

Acknowledgements

I would like to express my outmost gratitude to my Supervisor Erin Bachynski. She has an impressive wealth of knowledge and has given valuable guidance throughout the Master Thesis, helping me even outside working hours. She has shown nothing but patience and kindness even at less productive times on my part.

I would also like to thank all my friends at the Department of Marine Technology. My time studying in Trondheim has been the time of my life. There has been times of hard work and despair, but there has been even more times of happiness. The memories I have made here are invaluable to me.

Lastly, I would like to thank my Mother Sonal, Brother Jatin, Tara Ba, Aunt Ninni, Uncle Kashyap and Aunt Lissbeth for the patience, love and support they have shown me throughout my studies.

P.J.P

Abstract

This Master Thesis studies an offshore wind turbine supported by a monopile structure. Model tests for a fully flexible monopile were carried out in the Ocean Basin facility at SINTEF Ocean in August 2017, through the NOWITECH project. This thesis examines selected results from the experiments and introduces numerical simulations for comparison to the experimental results. For the numerical simulations the software SIMA RIFLEX, a finite element solver for static and dynamic analysis of slender marine structures, is utilized. The main focus has been put on validation of hydrodynamic load models, both linear and nonlinear, that can describe the response from the experiments, both on a statistical level and for single events.

A literature review regarding nonlinear hydrodynamic load models and ringing responses is performed. The literature review focuses on observations of ringing responses and the mechanisms that lead to ringing.

A beam element model was built in SIMA and presented by the Supervisor as a starting point to this thesis. The model was calibrated based on available decay tests from the experiments to have the same system damping ratio (0.47%) and first mode eigenfrequency (1.42 rad/s) as the experimental model. The damping ratio was estimated as 0.47%, which is considered to be relatively low compared to similar monopile supported offshore wind turbines in full scale, where damping ratios have been found up to 2.8%. An eigenvalue analysis was also conducted to confirm the eigenfrequencies found from the decay tests. The eigenvalue analysis also conveniently provided the modal shapes of the three first bending modes.

Regular wave tests were treated to establish the RAOs for first, second and third order. The first-order RAOs displayed a reasonable behaviour with good agreement between the simulated and experimental. The second order RAO also showed good agreement between the simulated and experimental results, except for one wave period, T = 9 s, where a strong over-prediction was made in the simulations. For the simulations of the regular wave tests, Morison's equation with linear kinematics was used together with the MacCamy-Fuchs correction for diffraction. However, only linear diffraction is accounted for by this method. The over-prediction may be a result of not taking second order diffraction effects into account in the simulations. The third order RAOs were of an order of magnitude lower than the first and second order RAOs. Thus, some uncertainty due to accuracy of measurements were connected to the third order RAOs.

A repeatability analysis for the experiments was performed for nine repeated irregular wave tests. The repeatability analysis revealed through the coefficient of variation that the random error connected to global maxima for the moment response was below 10%, indicating quite good repeatability. A considerably larger random error, far above 10%, was connected to the repetition of the magnitude of single event maxima. The coefficient of variation was also considered for the maximum wave amplitude at two different wave probes. This revealed that both global maxima and single event maxima were repeated quite well, with coefficient of variation below 10%.

A parameter study on the damping was initiated as the damping in the system, estimated from the decay tests was very low. Realistic damping ratios were found in the literature and considered. It is found that the originally estimated damping ratio is likely to not be representative of the system damping when the structure is subjected to waves. This is suggested based on the simulations with linear theory overestimating the response from the experimental tests, which is contradictory to what is found in the literature when considering extreme sea states. If a more realistic damping ratio of 1.1% is accepted as the damping ratio for the structure, it is found that linear wave kinematics with Wheeler stretching is the most appropriate method for describing the energy in the response from the experimental tests.

Ringing responses were identified in the experimental tests and were in agreement with how the phenomenon is described in the literature. It is found in the experiments that ringing responses are initiated by large, steep wave events. The ringing events characteristically have a large amplification from the steady state response and decays with the eigenfrequency for some periods. Clear ringing events were not found in the simulations. More likely than not, higher order than second order theory must be considered to properly describe the ringing phenomenon.

Sammendrag

Denne masteroppgaven tar for seg en offshore vindturbin støttet av en monopæl-struktur. I august 2017 ble det utført modelltester i Havbassenget ved SINTEF OCEAN på en fleksibel monopæl, gjennom NOWITECH-prosjektet. Denne masteroppgaven studerer enkelte resultater fra forsøkene og sammenligner de med resultater fra tilsvarende numeriske simuleringer. Programvaren SIMA RIFLEX, som anvender elementmetoden for statisk of dynamisk analyse av slanke marine strukturer, har blitt brukt for simuleringene. Hovedfokuset har blitt satt på å validere lineære og ulineære hydrodynamiske lastmodeller som kan beskrive strukturresponsen fra forsøkene, både på et statistisk nivå og for enkelthendelser.

En litteraturstudie som omfatter ulineære hydrodynamiske lastmodeller og ringing respons, som er en sterk høyfrekvent transient respons som er bekymringsverdig for ULS design, har blitt utført. Fokuset i litteraturstudien er lagt på observasjoner av ringing og hvilke mekanismer som eksiterer det.

En bjelkeelementmodell, laget i SIMA ble gitt av veileder ved oppstart av masteroppgaven. Simuleringsmodellen ble kalibrert ut i fra tilgjengelig data for "decay test" fra eksperimentene til å ha likt dempingsforhold (0.47%) og lik første mode egenfrekvens (1.42 rad/s). Dempingsforholdet ble ansett som lavt i forhold til lignende fullskala offshore vindturbiner støttet av en monopæl-struktur, hvor dempingsforhold på opp til 2.8% har blitt funnet. En egenverdianalyse ble også utført for å bekrefte egenfrekvensene estimert fra "decay test". Egenverdianalysen ga også de modale svingningsmønstrene for de tre første modene.

Testene med regulære bølger ble brukt til å finne RAO for første, andre og tredje orden. Førsteordens RAO viste en fornuftig respons, hvor det var god overenstemmelse mellom de simulerte og eksperimentelle resultatene. Andreordens RAO viste også god overenstemmelse mellom simuleringer og eksperimenter, bortsett fra ved $T = 9$ s, hvor simuleringene overestimerte responsen kraftig. Morisons ligning har blitt brukt til å simulere bølgelastene for de regulære testene sammen med MacCamy-Fuchs korreksjon for diffraksjon. Kun førsteordens diffraksjon blir tatt med i beregningen. Overestimeringen skjer sannsynligvis fordi andreordens diffraksjon ikke er tatt med i simuleringene. Tredjeordens RAO var en størrelsesorden lavere i verdi enn første- og andreordens RAO. På grunn av sensitivitet i forhold til nøyaktigheten av målingene er det vanskelig å konkludere angående gyldigheten av tredjeordens RAO.

En repeterbarhetsanalyse for eksperimentene ble utført for ni tester med irregulær bølger. Gjennom variasjonskoeffisienten ble det funnet at repeterbarheten av globale maksimum for moment respons var under 10% . En større variasjonskoeffisient, langt over 10% ble funnet for lokale maksimum for enkelthendelser. Variasjonskoeffisienten for bølgeamplitude ble funnet til å være under 10% for både globale og lokale maksimum, som indikerer god repeterbarhet.

En parameterstudie på dempingsforholdet ble utført ettersom den estimerte dempingen i systemet fra ”decay test” var veldig lav. Mer realistisk demping ble funnet i litteraturen. Ut i fra resultatene blir det antydet at det opprinnelig estimerte dempingsforholdet sannsynligvis ikke representerte dempingsforholdet når strukturen er utsatt for bølger. Dette blir foreslått ettersom simuleringene med lineær bølgeteori overestimerer responsen fra de eksperimentelle testene, noe som motstrider hva som blir funnet i litteraturen når ekstremsjøtilstander blir vurdert. Hvis et mer realistisk dempingsforhold blir akseptert til å gjelde, blir det konkludert med at lineær bølgeteori med Wheeler-strekking er den metoden for bølgekinematikk som beskriver energien i responsen fra de eksperimentelle testene best.

Ringing respons blir identifisert i de eksperimentelle testene og i enighet med litteraturen blir det funnet at ringing responsene blir satt i gang av en høy, bratt bølge. Ringing responsene har karakteristisk en høy amplifikasjon av responsen før den gradvis synker eksponentielt med egenfrekvensen. Klare tilfeller av ringing har ikke blitt funnet i simuleringene, til og med ikke med andreordens bølgeteori. Det virker dermed sannsynlig at lastmodeller av høyere orden må brukes for å beskrive ringing respons.

Contents

Preface i

Acknowledgements iii

Abstract v

Sammendrag vii

List of Tables xiv

List of Figures xix

Nomenclature xxi

1 Introduction 1
- 1.1 Background and Motivation . . . 1
- 1.2 Thesis Objectives . . . 3
- 1.3 Structure of the Report . . . 4

2 Related Literature 5

3 Structural Dynamics 9
- 3.1 Mass Matrix . . . 10
- 3.2 Damping Matrix . . . 11
- 3.3 Newmark-Beta Method for Time Integration . . . 12
- 3.4 Decay Test . . . 13
- 3.5 Eigenvalue Analysis . . . 14
- 3.6 Simulation Model . . . 15

4 Wave Kinematics and Load Models **19**
4.1 Potential Flow Theory 19
4.1.1 First-Order Potential Flow Theory 21
4.1.2 Second order Potential Flow Theory 24
4.2 Morison's Equation 25
4.2.1 MacCamy-Fuchs Correction for Diffraction 26
4.3 Stretching of Wave Kinematics 27
4.3.1 Simple Extrapolation 27
4.3.2 Wheeler Stretching 28
4.4 FNV Model 29
4.5 Added Mass and Drag Coefficients 30

5 Stochastic Processes **33**
5.1 Autocorrelation Function and Spectral Density Function 34
5.2 Statistical Description of Waves 37
5.2.1 Wave Spectra 38
5.3 Structural Response Statistics 39

6 Experimental Test and Simulation Procedure **41**
6.1 Scaling 42
6.2 Filtering 44
6.3 Model Calibration Tests 46
6.4 Regular Waves 48
6.5 Irregular Waves 50
6.6 Wave Generation for Simulations 55

7 Results and Discussion **59**
7.1 Calibration of Simulation Model 59
7.2 Regular Wave Results 63
7.3 Irregular Wave Results 66
7.3.1 Repeatability Analysis 66
7.3.2 Parameter Study on the Damping 69
7.3.3 Ringing Responses 73

8 Concluding Remarks **79**
8.1 Recommendations for Further Work 81

Bibliography **83**

Appendices I

A RAOs from Regular Wave Tests III

A.1 Mudline Moment RAOs III
A.2 Waterline Moment RAOs V

B Spectra for Irregular Wave Test Damping Parameter Study VII

B.1 Spectra for Test No. 35010 VII
B.2 Spectra for Test No. 36010 X
B.3 Spectra for Test No. 37010 XII
B.4 Spectra for Test No. 38010 XIV
B.5 Spectra for Test No. 38020 XVI
B.6 Spectra for Test No. 38030 XVIII
B.7 Spectra for Test No. 38040 XX
B.8 Spectra for Test No. 38110 XXII
B.9 Spectra for Test No. 38120 XXIV
B.10 Spectra for Test No. 38130 XXVI
B.11 Spectra for Test No. 38140 XXVIII
B.12 Spectra for Test No. 38150 XXX
B.13 Spectra for Test No. 38160 XXXII
B.14 Spectra for Test No. 38170 XXXIV
B.15 Spectra for Test No. 38180 XXXVI
B.16 Spectra for Test No. 39010 XXXVIII

C Ringing Events XLI

C.1 Ringing Event in Test No. 37010 XLI
C.2 Ringing Event in Test No. 38030 XLIII
C.3 Ringing Event in Test No. 38170 XLIV
C.4 Ringing Event in Test No. 38180 XLVI
C.5 Ringing Event in Test No. 38110 XLVII

List of Tables

3.1 Newmark-Beta parameters used for dynamic analysis in SIMA 13

3.2 Overview of the supernodes with their respective coordinates and boundary conditions 17

3.3 Overview of the lines connected by supernodes and the respective line lengths in meters 17

6.1 Froude scaling of selected physical parameters 43

6.2 Overview of calibrated regular waves with wave height, H [m], wave period, T [s], and start and end times of signal, t_1 [s] and t_2 [s] 48

6.3 Overview of the test numbers and their corresponding calibrated wave numbers for the regular wave tests, as well as K_C number, added mass and drag coefficients for each test 49

6.4 Overview of calibrated irregular waves with significant wave height, H_s [m] and peak period, T_p [s] 51

6.5 Overview of the test numbers and their corresponding calibrated wave numbers for the irregular wave tests, as well as K_C number, added mass and drag coefficients for each test 52

6.6 First mode damping ratios (λ_1 [%]) and stiffness-proportional damping coefficients (α_1) for the parameter study 54

6.7 Overview of the file length and time series end time [s] for the sampled waves elevation time series for regular waves to be implemented in SIMA 57

7.1 Eigenfrequencies for the three first modes ω_n [rad/s], with error in percent relative to experimental decay test, and corresponding eigenperiod T_n [s] 62

7.2 Overview of the global maxima [Nm], time of occurrence of global maxima [s] and local maxima [Nm] (at time of base case global maxima) for the mudline and waterline moment in the repeated tests 67
7.3 Overview of the global maxima [m], time of occurrence of global maxima [s] and local maxima [m] (at time of base case global maxima) for the surface elevation measured at wave probe 7 and wave probe 15 in the repeated tests 68
7.4 Coefficient of variation in percent for the maximum mudline and waterline moment, as well as the maximum surface elevation at wave probe 7 and wave probe 15 in the repeated tests for both global and local maxima . . . 68

List of Figures

2.1 Surface elevation (top) and tension response (bottom) showing a typical occurrence of ringing due to a steep wave event following from relatively calm sea. Taken from Faltinsen et al. (1995). 6

3.1 Sketch of the three first modal shapes in bending of a cantilever beam (increasing mode from left to right) 15
3.2 Simulation model, as modelled in SIMA 16
3.3 Definitions of the different definitions used to describe the system topology in SIMA. Taken from SINTEF Ocean (2017*b*) 18

4.1 Example of surface elevation according to second-order potential flow theory (yellow) as a sum of the first-order wave elevation (blue) and the second-order correction (red) 25
4.2 Simple extrapolation of the wave kinematics above the mean surface level 28
4.3 Wheeler stretching, where the linear wave potential is stretched above mean surface level and compressed below mean surface level 28
4.4 Selection of wake amplification factor, ψ, as a function of the ratio of K_C and C_{DS} for smooth (solid line) and rough cylinder (dotted line). Taken from DNV GL (2017). 31
4.5 Selection of added mass coefficient, C_A, as a function of K_C for smooth (solid line) and rough cylinder (dotted line). Taken from DNV GL (2017). 32

6.1 The four main types of filters: lowpass (a), highpass (b), bandpass (c) and bandstop (d). The dotted line represents an ideal filter, while the solid line represents a more realistic filter. 44
6.2 50-year contour line and selected sea states (the four smallest sea states are not considered in this work). Taken from Thys (2017). 50

6.3 Set-up of wave probes for regular and irregular wave tests, when the structure is installed at blink (coordinate $(0, 0)$). Taken from Thys (2017). . . . 55
6.4 Sampled surface elevation for SIMA based on measurements from experiments, exemplified for a regular wave 56

7.1 Waterline moment spectrum for experimental decay tests, where the structure was excited by a hit around the middle of the tower 60
7.2 Waterline moment spectrum for simulated decay tests, where the structure was excited by a hit around the middle of the tower 60
7.3 Comparison between experimental and simulated waterline moment decay time series, where the structure was excited by a hit around the middle of the tower 61
7.4 Comparison between experimental and simulated waterline moment decay time series, where the structure was excited by a hit at the top of the tower 61
7.5 Modal shapes and corresponding eigenfrequencies for the first three bending modes from the eigenvalue analysis 62
7.6 1^{st} order RAO for mudline moment from regular waves (steepness 1/30) . 63
7.7 1^{st} order RAO for mudline moment from regular waves (steepness 1/40) . 63
7.8 2^{nd} order RAO for mudline moment from regular waves (steepness 1/30) 64
7.9 2^{nd} order RAO for mudline moment from regular waves (steepness 1/40) 64
7.10 3^{rd} order RAO for mudline moment from regular waves (steepness 1/30) . 64
7.11 3^{rd} order RAO for mudline moment from regular waves (steepness 1/40) . 64
7.12 Mudline moment for test CE20040 (wave steepness 1/30), showing overestimation of simulated response 65
7.13 Mudline moment for test CE21091 (wave steepness 1/30), showing overestimation of simulated response at third order 66
7.14 Mudline moment for test CE21091 (wave steepness 1/30), showing a well estimated simulated response 66
7.15 Mudline moment spectra for the four different simulated wave kinematics models compared to the experimental test. Simulations with damping ratio 0.47%. 70
7.16 Waterline moment spectra for the four different simulated wave kinematics models compared to the experimental test. Simulations with damping ratio 0.47%. 70
7.17 Mudline moment spectra for the four different simulated wave kinematics models compared to the experimental test. Simulations with damping ratio 0.68%. 70

7.18 Waterline moment spectra for the four different simulated wave kinematics models compared to the experimental test. Simulations with damping ratio 0.68%. 70
7.19 Mudline moment spectra for the four different simulated wave kinematics models compared to the experimental test. Simulations with damping ratio 0.89%. 71
7.20 Waterline moment spectra for the four different simulated wave kinematics models compared to the experimental test. Simulations with damping ratio 0.89%. 71
7.21 Mudline moment spectra for the four different simulated wave kinematics models compared to the experimental test. Simulations with damping ratio 1.10%. 71
7.22 Waterline moment spectra for the four different simulated wave kinematics models compared to the experimental test. Simulations with damping ratio 1.10%. 71
7.23 Surface elevation (blue) and waterline moment (red), showing a ringing event from the experiments in test number 37010 74
7.24 Waterline moment from simulation with linear theory at the time of the ringing event from the experiments in test number 37010 75
7.25 Waterline moment from simulation with simple extrapolation at the time of the ringing event from the experiments in test number 37010 75
7.26 Waterline moment from simulation with Wheeler stretching at the time of the ringing event from the experiments in test number 37010 75
7.27 Waterline moment from simulation with second-order theory at the time of the ringing event from the experiments in test number 37010 75
7.28 Surface elevation (blue) and waterline moment (red), showing a series of ringing events the experiments in test number 38180 76
7.29 Waterline moment from simulation with linear theory at the time of the ringing event from the experiments in test number 38180 76
7.30 Waterline moment from simulation with simple extrapolation at the time of the ringing event from the experiments in test number 38180 76
7.31 Waterline moment from simulation with Wheeler stretching at the time of the ringing event from the experiments in test number 38180 76

A.1 1^{st} order RAO for mudline moment from regular waves (steepness 1/30) . III
A.2 1^{st} order RAO for mudline moment from regular waves (steepness 1/40) . III
A.3 2^{nd} order RAO for mudline moment from regular waves (steepness 1/30) IV

A.4 2^{nd} order RAO for mudline moment from regular waves (steepness 1/40) IV
A.5 3^{rd} order RAO for mudline moment from regular waves (steepness 1/30) . IV
A.6 3^{rd} order RAO for mudline moment from regular waves (steepness 1/40) . IV
A.7 1^{st} order RAO for waterline moment from regular waves (steepness 1/30) V
A.8 1^{st} order RAO for waterline moment from regular waves (steepness 1/40) V
A.9 2^{nd} order RAO for waterline moment from regular waves (steepness 1/30) V
A.10 2^{nd} order RAO for waterline moment from regular waves (steepness 1/40) V
A.11 3^{rd} order RAO for waterline moment from regular waves (steepness 1/30) VI
A.12 3^{rd} order RAO for waterline moment from regular waves (steepness 1/40) VI

B.1 Simulated response spectra for the four different methods of generating wave kinematics compared with experimental test spectra for all damping ratios in the parameter study for irregular waves VII

C.1 Surface elevation (blue) and waterline moment (red), showing a ringing event from the experiments in test number 37010 XLI
C.2 Waterline moment from simulation with linear theory at the time of the ringing event from the experiments in test number 37010 XLII
C.3 Waterline moment from simulation with simple extrapolation at the time of the ringing event from the experiments in test number 37010 XLII
C.4 Waterline moment from simulation with Wheeler stretching at the time of the ringing event from the experiments in test number 37010 XLII
C.5 Waterline moment from simulation with second-order theory at the time of the ringing event from the experiments in test number 37010 XLII
C.6 Surface elevation (blue) and waterline moment (red), showing a ringing event from the experiments in test number 38030 XLIII
C.7 Waterline moment from simulation with linear theory at the time of the ringing event from the experiments in test number 38030 XLIII
C.8 Waterline moment from simulation with simple extrapolation at the time of the ringing event from the experiments in test number 38030 XLIII
C.9 Waterline moment from simulation with Wheeler stretching at the time of the ringing event from the experiments in test number 38030 XLIV
C.10 Waterline moment from simulation with second-order theory at the time of the ringing event from the experiments in test number 38030 XLIV
C.11 Surface elevation (blue) and waterline moment (red), showing a ringing event from the experiments in test number 38170 XLIV

C.12 Waterline moment from simulation with linear theory at the time of the ringing event from the experiments in test number 38170 XLV
C.13 Waterline moment from simulation with simple extrapolation at the time of the ringing event from the experiments in test number 38170 XLV
C.14 Waterline moment from simulation with Wheeler stretching at the time of the ringing event from the experiments in test number 38170 XLV
C.15 Waterline moment from simulation with second-order theory at the time of the ringing event from the experiments in test number 38170 XLV
C.16 Surface elevation (blue) and waterline moment (red), showing a series of ringing events the experiments in test number 38180 XLVI
C.17 Waterline moment from simulation with linear theory at the time of the ringing event from the experiments in test number 38180 XLVI
C.18 Waterline moment from simulation with simple extrapolation at the time of the ringing event from the experiments in test number 38180 XLVI
C.19 Waterline moment from simulation with Wheeler stretching at the time of the ringing event from the experiments in test number 38180 XLVII
C.20 Surface elevation (blue) and waterline moment (red), showing a series of ringing events the experiments in test number 38110 XLVII
C.21 Waterline moment from simulation with linear theory at the time of the ringing event from the experiments in test number 38110 XLVIII
C.22 Waterline moment from simulation with simple extrapolation at the time of the ringing event from the experiments in test number 38110 XLVIII
C.23 Waterline moment from simulation with Wheeler stretching at the time of the ringing event from the experiments in test number 38110 XLVIII

Nomenclature

Acronyms

FEM	Finite Element Method
FFT	Fast Fourier Transform
FNV	Faltinsen, Newman, Vinje (load model)
ISSC	International Ship and Offshore Structures Congress
ITTC	International Towing Tank Conference
JONSWAP	Joint North Sea Wave Observation Project
NOWITECH	Norwegian Research Centre for Offshore Wind Technology
PM	Pierson-Moskowitz (wave spectrum)
RAO	Response Amplitude Operator
TLP	Tension-Leg Platform
TMA	Texel, Marsen, Arsloe (wave spectrum)
ULS	Ultimate Limit State

Greek Symbols

α	JONSWAP parameter
α_1	Rayleigh mass-proportional damping coeffcient
α_2	Rayleigh stiffness-proportional damping coeffcient

β	Newmark-Beta integration parameter
Δt	Time step
δ	Logarithmic decrement
ϵ_j	Random phase angle
γ	JONSWAP peakedness parameter
γ	Newmark-Beta integration parameter
λ	Scaling factor
λ	Wave length
λ_i	Modal damping
μ_X	Mean value
ν	Fluid kinematic viscosity
ω	Wave frequency
ω_c	Cut-off frequency
ω_i	Modal eigenfrequency
ω_n	Natural frequency
ω_p	Peak wave frequency
ϕ	Velocity potential
$\Phi(\omega, h)$	TMA spectrum water depth parameter
ϕ_0	Incident wave potential
ϕ_1	First-order wave potential
ϕ_2	Second-order wave potential
ϕ_D	Diffraction potential
$\psi(K_C)$	Wake amplification factor
ρ	Water density

σ	JONSWAP parameter
σ_X	Standard deviation
τ	Time shift
ξ	Damping ratio (logarithmic decrement)
ζ	Free surface elevation
ζ_a	Wave amplitude

Matrices and Vectors

$\boldsymbol{B}$	System linear damping matrix
$\boldsymbol{K}$	Global stiffness matrix
$\boldsymbol{M}$	Mass matrix
$\boldsymbol{N}$	Shape functions for displacements
$\boldsymbol{n}$	Normal vector
$\boldsymbol{V}$	Velocity vector
$\ddot{\vec{r}}$	Nodal acceleration vector
$\dot{\vec{r}}$	Nodal velocity vector
$\vec{\Phi}$	Eigenvector
$\vec{a}$	Butterworth filter vector of coefficients
$\vec{b}$	Butterworth filter vector of coefficients
$\vec{r}$	Nodal displacement vector
$\vec{R}^{ext}$	External load vector
$\vec{R}^{int}$	Internal reaction force vector
$\vec{u}$	System displacement vector

Superscripts

A	Projected area

A	Wave amplitude
C_A	Added mass coefficient
C_D	Drag coefficient
C_M	Inertia coefficient
C_v	Coefficient of variation
D	Diameter
dF	Force per unit length
F_g	Gravity force
F_i	Inertia force
F_D	Diffraction loads
F_{exc}	Potential flow excitation loads
F_{FK}	Froude-Kriloff loads
Fn	Froude number
$G(\omega)$	Filter gain
H	Wave height
$H(z)$	Discrete time filter transfer function
H_s	Significant wave height
J_1	First-order Bessel function
K_C	Keulegan-Carpenter number
R_{XX}	Autocorrelation function
Re	Reynolds number
S_{XX}	Spectral density function
T	Wave period
T_n	Modal eigenperiod

T_p	Peak wave period
U	Fluid particle velocity amplitude
u_α	Horizontal acceleration
V_p	Phase velocity
$X(t)$	Stochastic process
Y_1	Second-order Bessel function

Subscripts

$\bar{x}$	Sample mean value
$\ddot{r}$	Moving body acceleration
$\dot{r}$	Moving body velocity
a	Cylinder radius
a_1	Horizontal partical acceleration
g	Gravtiational constant
h	Water depth
k	Wave number
m_k	Spectral moments
p	Pressure
p_a	Atmospheric pressure
p_d	Dynamic pressure
p_s	Static pressure
s_x	Sample standard deviation
u	Horizontal partical velocity
v_r	Relative velocity
a	Radius

Chapter 1

Introduction

1.1 Background and Motivation

The focus on renewable energy solutions is growing and it is projected that the use of offshore wind turbines to generate power will be a dominant part of the renewable energy portfolio in the future as the cumulative installed offshore wind capacity has increased exponentially since the early 2000's (WindEurope 2017). The first offshore wind farm was installed in 1991 and significant developments have been made since then, with regards to e.g. aerodynamic efficiency, power output, drivetrain and substructure concepts, as well as wind turbine and structure size. As the access to larger wind resources are found further offshore, there is a drive to push the offshore wind industry towards larger turbines and deeper water depths. However, to access larger wind resources one must dimension the structures for larger loads, as both the wind and wave loads will intuitively be larger.

When considering substructures for offshore wind turbines, floating substructures such as spar, semi-submersible and tension-leg platforms are reasonable solutions for deep water, with the first commercial floating wind farm (Hywind) having been installed outside Peterhead, Scotland, with a spar solution. However, at intermediate water depths bottom-fixed solutions, such as monopiles, gravity based support and jacket structures are usually more feasible. In 2016 monopiles made up around 81% of the cumulative market share for grid-connected offshore wind sub-structures. Understanding the dynamic responses of a monopile is therefore of large interest in the offshore wind industry. The wave loads on a monopile structure become more significant as the diameter of the monopile increases and the water depth increases. In addition the structural resonance frequencies are pushed lower towards the primary wave excitation frequencies.

Model tests for a fully flexible monopile were carried out in the Ocean Basin facility at SINTEF Ocean in August 2017. This was a part of the NOWITECH research cooperation on offshore wind technology co-financed by the Research Council of Norway, industry and research partners (NOWITECH 2017). The model tests were carried out to investigate second-order loads, slamming loads and ringing responses. A 5 MW bottom-fixed supported wind turbine, with monopile diameter $D = 7m$ at water depth $h = 30m$ was tested. The design of the wind turbine was based on the NREL 5MW reference wind turbine (Jonkman et al. 2009) and the monopile was based on the OC3 design (Jonkman & Musial 2010). The monopile was subjected to wave loads and had no aerodynamic loading. Drag disks were used as a substitute for a model scale wind turbine, and represented the aerodynamic damping one would get from a wind turbine, as well as the heavy top mass.

A monopile supported wind turbine is characterized by a long slender structure with almost uniform circular pipe cross-sections. This implies that the structural design is very simple. However, the weight of the wind turbine introduces a relatively large top mass which is concentrated at a high location, implying that structural dynamics could be very important. In severe waves, the monopile structure may be vulnerable to ringing and springing responses. Springing is a steady-state response to sum-frequency wave effects, while ringing is a high frequency transient response, which is of concern in the industry when considering extreme responses for ULS. Ringing was first observed in the 1990's for TLPs. In the same decade developments on theory for describing the phenomenon was made. Thus, a lot of research concerning ringing responses has been conducted for large platform structures.

Ringing has not been studied as extensively for offshore wind monopile structures. This thesis aims to identify ringing responses and the mechanisms leading to the responses for a monopile structure for an offshore wind turbine, as well as exploring load models that can describe the phenomena, having model test data as a reference. The thesis also aims to validate selected experimental results of the NOWITECH monopile and set some measure of the random error connected to the NOWITECH experiments.

1.2 Thesis Objectives

A closer examination of the results of the NOWITECH model tests will include comparisons of numerical simulations with the model test responses. In order to understand the validation more completely, an uncertainty analysis based on repeatability in the model tests will be used to set some error bounds within which the predictions of the numerical model will be considered valid. Several hydrodynamic load models and sets of structural model parameters will be considered in the validation process.

The main objectives for this Master Thesis are listed below.

- Literature review regarding ringing responses and nonlinear hydrodynamic load models for large-diameter monopile wind turbines.
- Further development of a beam element model of the NOWITECH monopile in the simulation software SIMA (at full scale). The simulation model should be validated against the model scale experimental model through the available decay test data in wet conditions. Selection of added mass and drag coefficients for preliminary comparisons with the model tests should also be considered.
- Repeatability analysis of the long-crested wave tests to establish uncertainty bounds for validation.
- Statistical analysis of the obtained measured data. Identification of particularly interesting wave events from long-crested wave time series and identification of ringing responses.
- Filtering and importing of the measured wave elevation for selected long-crested wave time series, and comparison of the response with a Morison model with different types of integration up to the free surface, considering both first- and second-order waves.
- Validation of the obtained responses - either event-by-event or on a statistical level. Uncertainty in the model properties may be addressed through a numerical parameter study.

1.3 Structure of the Report

The main part of this Master Thesis is divided into eight chapters. Appendices are included after the main part and include results that have not been included in the main part of the thesis.

Chapter 2 gives an overview of related literature with focus on ringing responses and the mechanisms leading to ringing. This is mainly discussed in form of load models and wave parameters.

Chapter 3 describes the theoretical background of the structural dynamics used to describe the monopile structure. Emphasis has been put on how the structural dynamics is defined and solved in the simulation software, SIMA RIFLEX. A brief overview of the properties of the beam element simulation model and how it is implemented in SIMA RIFLEX is also presented.

Wave kinematics and load models relevant for this work are presented in Chapter 4. This includes linear wave theory, stretching techniques for linear theory, second-order wave theory, Morison's equation and the FNV formulation for third-order loads. The method used for selection of added mass and drag coefficients is also presented.

An overview of relevant theoretical background of stochastic processes is given in Chapter 5. This theoretical background is further used as a basis when the statistical description of waves and structural response statistics are considered.

Chapter 6 addresses scaling laws relevant for experimental model tests where wave loads are studied. Filtering is also discussed as it is highly relevant for post-processing of data. Furthermore the methodology of the experimental tests and simulations is presented. This includes model calibration tests, i.e. decay test and eigenvalue analysis, regular wave tests and irregular wave tests.

The results from the analyses are presented in Chapter 7. The results are presented as comparisons between the experimental tests and the corresponding simulations. The validity of the simulations against the experiments is discussed, as well as the uncertainties in the experimental tests following from repeated tests.

Concluding remarks and recommendations for further work are given in Chapter 8.

Chapter 2

Related Literature

Gurley & Kareem (1998) state that significant interest is shown in identifying the mechanisms that lead to ringing as this response phenomena can lead to extreme loads significant for the structural integrity. In some cases it may also have negative consequences for the fatigue life of a structure, although this is debated. Definitions of both ringing and springing are given as these terms are commonly interchanged. Springing is defined as a steady-state high-frequency response in the vertical and/or bending modes, in particular seen for TLPs and gravity based structures. Springing behaviour is common in both mild and severe sea states and is induced by second order wave effects at the sum frequencies. Ringing is a strong high-frequency transient response observed also in the vertical and/or bending modes. It is only seen in severe sea states and is triggered by a high, steep wave event. However, according to Faltinsen et al. (1995) ringing is not an effect due to breaking waves or slamming, even though the impulsive response may resemble that of a slamming event. Ringing may certainly occur as a result of breaking waves but breaking waves are not a criteria to trigger ringing. The transient response decays to steady state exponentially, which depends on the damping of the system. Thus, a higher level of damping in the system can result in a quicker decay of the response, but cannot prevent ringing from occurring.

Ringing is observed for marine structures as structural deflections at natural frequencies substantially higher than the dominant wave frequencies and cannot be explained by traditional theories of wave diffraction (Faltinsen et al. 1995). Bachynski & Moan (2014) establish that marine structures with natural periods in the range of 1-5 s are susceptible to ringing. Offshore wind turbines with monopile support typically have natural frequency of the 1^{st} mode in the range 0.25-0.6 Hz (de Ridder et al. 2011), corresponding to natural periods of about 1.5-4 s.

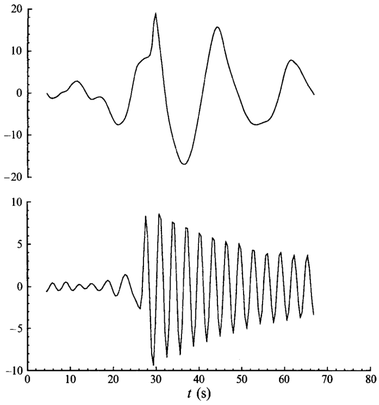

Figure 2.1: Surface elevation (top) and tension response (bottom) showing a typical occurrence of ringing due to a steep wave event following from relatively calm sea. Taken from Faltinsen et al. (1995).

Bachynski & Moan (2014) have summed up some of the hydrodynamic criteria for ringing loads that have been described in the literature. These criteria are reproduced here.

1. Presence of surface-piercing columns
2. Low Keulegan-Carpenter number $K_C < 5$ ($K_C = UT/D$, where U is the fluid particle velocity amplitude, T is the wave period and D is the diameter of the surface-piercing column) (fluid loading dominated by inertial loads)
3. Low diameter-wavelength (D/λ) ratio (linear diffraction is not significant): $D/\lambda < 0.2$ (alternatively: $ka < 0.63$, where $k = 2\pi/\lambda$ and $a = D/2$)
4. Wave height comparable to cross-sectional structure dimensions

Chaplin et al. (1997) did analyses of two series of experiments with a vertical cylinder in the inertia regime in steep non-breaking waves. The stiffness of the cylinder was varied to achieve natural frequencies 3-11 times the dominant wave frequency. It is established that springing can be calculated based on the sum-frequency excitation predicted by second-order diffraction programs. On the other side, there is a lot of uncertainty connected to theoretical and numerical predictions of ringing as the physical mechanisms that lead to ringing are not fully understood. Peak loads could not be predicted by using a Morison model, with the deviation between measurements and the Morison model increasing with wave steepness. Better agreement was achieved by slender-body corrections to Morison's equation, which improves the accuracy of the inertia term when considering potential flow loads. The Morison model is in general used to estimate the forces on slender structures and calculates the excitation force as a sum of inertia forces and viscous forces (Morison et al. 1950).

Schløer et al. (2016) makes the point that nonlinear waves are generally steeper than linear waves. Thus nonlinear waves are more likely to induce ringing responses of a structure. Linear theory applied with Wheeler stretching may better approximate the extreme loads but it is concluded that it is necessary to consider nonlinear wave loads. The use of nonlinear waves is in particular critical for fatigue analyses, as nonlinear waves contribute more to the fatigue damage compared to linear loads.

The FNV theory was developed by Faltinsen et al. (1995) to give a better estimate of loads due to regular long waves with large amplitudes of the same order as the cylinder radius (A/a = $\mathcal{O}(1)$, where A is the wave amplitude and a is the cylinder radius). Moreover, the waves are assumed to be long compared to both the wave amplitude ($kA << 1$) and cylinder radius ($ka << 1$). The FNV theory includes second order and third order loads. In particular the third order load is thought to give a good estimate for the mechanisms leading to ringing. The theory is applicable for deep water, which is presumably not highly relevant for monopile substructures for offshore wind turbines, which are usually located in intermediate water depths (15-50 m) from a hydrodynamic point of view (Bachynski et al. 2017). The FNV theory was extended to be valid for irregular waves by Newman (1996), making it more applicable for real wave conditions.

The FNV formulation is not believed to be consistent with respect to sum/difference frequency terms. Moreover, a secondary load cycle, i.e. a secondary oscillation in the loading which starts one quarter period after the main peak in the loading has passed, was first observed by Grue et al. (1993). This is not predicted by the FNV formulation. Many experimental results have been performed in order to validate the FNV model (e.g. Krokstad et al. (1998) and Stansberg (1997)), and the consensus is that FNV overpredicts the second order loads, while the third-order component compares well to full diffraction theory of third order. Johannessen (2012) proposes an alternate implementation of FNV for irregular waves (with the direct implementation following from Newman (1977)) taking into account the cut-off frequency of the spectrum and presence of low-frequency components. This is done by introducing a bandwidth parameter which effectively limits the interaction of different frequency components. This mitigates the problem of FNV not being consistent for sum/difference frequency terms, so that only sum-frequency terms are implemented. The implementations prove to be well suited for a gravity-based structure.

Recent developments have been made to generalize the FNV formulation. Kristiansen & Faltinsen (2017) generalize the FNV method to finite water depth. Moreover, arbitrary higher order wave theory or numerically calculated wave kinematics may be used in the generalized method. In their work the generalized method is applied with wave kinematics from Stokes third- and fifth-order wave theory.

Chapter 3

Structural Dynamics

When considering a bottom-fixed monopile, the structural dynamics are studied for a flexible structure. Computation of the structural dynamics is done with time-domain finite element method (FEM) analysis applied with SINTEF Ocean's software SIMA RIFLEX, where RIFLEX is the finite element solver, and SIMA is the workbench, or user interface. The software will hereafter be referred to as SIMA. This section is very closely based on the RIFLEX Theory Manual (SINTEF Ocean 2017*a*) (the documentation is only available with the software).

The monopile is modelled with beam elements as these elements typically manage to capture deflections and bending of long slender structures very well. The beam theory in SIMA is nonlinear and based on the following assumptions:

1. A plane section normal to the longitudinal axis remains plane and normal to the longitudinal axis
2. Lateral contraction caused by axial elongation is neglected
3. Shear deformations due to lateral loading are accounted for by modifying the bending stiffness
4. St. Venants torsion model is applied
5. Torsional warping resistance is neglected
6. Coupling between torsion and bending is accounted for by a second order approximation of torsion and bending curvature but the coupling is not reflected in the

stiffness matrix

The governing equation for the structural dynamics is found through virtual work considerations, where it is required that the virtual work done by external loads (body forces and surface tractions) are balanced by the sum of the virtual work of inertial, dissipative and internal forces (Bell 2013).

$$\begin{aligned}\vec{u} &= \boldsymbol{N}\vec{r}\\ \boldsymbol{M}\ddot{\vec{r}} + \boldsymbol{B}\dot{\vec{r}} + \vec{R}^{int} &= \vec{R}^{ext}\end{aligned} \tag{3.1}$$

where $\vec{u}$ is the system displacement vector, $\boldsymbol{N}$ are the shape functions of the displacements, $\vec{r}$ is the nodal displacement vector, $\boldsymbol{M}$ is the system mass matrix, $\boldsymbol{B}$ is the system linear damping matrix, $\vec{R}^{int}$ is the internal reaction force vector and $\vec{R}^{ext}$ is the external load vector. Both the internal reaction force vector and external load vector are generally nonlinear functions of the nodal displacement vector. The internal reaction forces can have nonlinearities related to geometric stiffness, if there is contribution from axial forces to transverse stiffness, or nonlinear material properties. For linear material properties and no nonlinear geometric stiffness contributions, the internal reaction forces typically reduce to a stiffness force, described by the global stiffness matrix $\boldsymbol{K}$ and the nodal displacement vector. This is reasonable for a monopile structure where relatively small displacements compared to its dimensions can be expected.

$$\vec{R}^{int} = \boldsymbol{K}\vec{r} \tag{3.2}$$

The system for the structural dynamics then reduces to a multi-degree of freedom mass ($\boldsymbol{M}$) - spring ($\boldsymbol{B}$) - damper ($\boldsymbol{K}$) system.

3.1 Mass Matrix

The system mass matrix, $\boldsymbol{M} = \boldsymbol{M}^S + \boldsymbol{M}^H(r)$, is a sum of the structural mass matrix and the displacement-dependent hydrodynamic mass matrix, accounting for the structural acceleration terms in the Morison equation (to be further discussed in Section 4.2) as added mass contributions. The mass matrix is defined as a consistent mass matrix, i.e. using the same shape functions as the stiffness matrix. The mass matrix will generally not be diagonal due to this formulation as it would be with a lumped mass formulation. In this case, since the stiffness matrix will contain non-diagonal terms, no significant computational benefits will arise by defining a lumped mass matrix when considering time-domain integration schemes for the dynamic equation. Nevertheless, using a consistent mass matrix generally gives better accuracy than using a lumped mass matrix when using an implicit integration method, e.g. as described in Section 3.3.

3.2 Damping Matrix

The system linear damping matrix, **B**, is generally a sum of the internal structural damping matrix and hydrodynamic damping matrix. It is expected that the hydrodynamic damping for the monopile structure is very low, or negligible, so that the damping in the system is governed by the structural damping. The structural damping is often described well by the Rayleigh structural damping formulation. This formulation establishes the structural damping of a system as a linear combination of the mass and stiffness matrices.

$$\boldsymbol{B} = \alpha_1 \boldsymbol{M} + \alpha_2 \boldsymbol{K} \tag{3.3}$$

where α_1 and α_2 are the mass-proportional and stiffness-proportional damping coefficients respectively. Introducing the structural damping in such a way that it is of computational convenience and the Rayleigh damping matrix becomes orthogonal with respect to its eigenvectors. From this it follows that the modal damping λ_i becomes a function of the modal eigenfrequency ω_i and the damping coefficients.

$$\lambda_i = \frac{1}{2}\left[\frac{\alpha_1}{\omega_i} + \alpha_2 \omega_i\right] \tag{3.4}$$

The damping coefficients apply to all global degrees of freedom and therefore Equation 3.4 describes an overall damping of the system relative to critical damping. Damping in axial, bending and torsional degree of freedom can be specified individually by specifying individual damping coefficients for each degree of freedom.

If the damping ratio and eigenfrequency is known for at least two modal shapes, the two coefficients α_1 and α_2 can be determined as

$$\begin{aligned}\alpha_1 &= \frac{2\omega_1\omega_2}{\omega_2^2 - \omega_1^2}(\lambda_1\omega_2 - \lambda_2\omega_1) \\ \alpha_2 &= \frac{2(\omega_2\lambda_2 - \omega_1\lambda_1)}{\omega_2^2 - \omega_1^2}\end{aligned} \tag{3.5}$$

From Equation 3.3 it is seen that the mass-proportional damping is effective for low frequencies, while the stiffness proportional damping is effective for high frequencies. However, for the monopile structure in this work the mass-proportional damping could introduce more damping at low frequencies than what is reasonable. Therefore, the structural damping is taken as pure stiffness-proportional damping, setting $\alpha_1 = 0$. In SIMA the structural damping is implemented by the stiffness-proportional damping coefficient α_2. The coefficient is determined by Equation 3.6. In this work emphasis has been put on damping the first mode of the structure, which is assumed to be the mode for which the majority of the response will be concentrated around. Thus, α_2 is determined by considering the first bending mode of the structure.

$$\alpha_2 = \frac{2\lambda_1}{\omega_1} \tag{3.6}$$

λ_1 and ω_1 are determined from the decay test, described in Section 3.4, where λ_1 is set equal to ξ.

3.3 Newmark-Beta Method for Time Integration

The Newmark-Beta method is a numerical method for time integration of differential equations, and is the method applied in SIMA to solve the governing equation for the structural dynamics in Equation 3.1. The governing equation is discretized in the time domain and solved in steps with equal time spacing Δt, i.e. at times $t = \{t_0, t_1 = t_0 + \Delta t, t_2 = t_0 + 2\Delta t, ..., t_n = t_0 + n\Delta t\}$. The Newmark-Beta method is an implicit method, so that when solving for the displacements and velocities at time step $n+1$ ($\vec{r}_{n+1}$ and $\dot{\vec{r}}_{n+1}$), terms for the accelerations in the current time step ($\ddot{\vec{r}}_{n+1}$) will appear on the right side of the equations.

$$\begin{aligned} \dot{\vec{r}}_{n+1} &= \dot{\vec{r}}_n + (1-\gamma)\ddot{\vec{r}}_n \Delta t + \gamma \ddot{\vec{r}}_{n+1} \Delta t \\ \vec{r}_{n+1} &= \vec{r}_n + \dot{\vec{r}}_n \Delta t + (\frac{1}{2} - \beta)\ddot{\vec{r}}_n (\Delta t)^2 + \beta \ddot{\vec{r}}_{n+1} (\Delta t)^2 \end{aligned} \tag{3.7}$$

where β and γ control the numerical stability and numerical damping of the method, with $\gamma > 0.5$, $\gamma = 0.5$ and $\gamma < 0.5$ giving positive, no and negative numerical damping respectively. The method is unconditionally stable for $2\beta \geq \gamma \geq 0.5$, which is valid for any value of the time step Δt (Gavin 2016).

The parameters for the Newmark-Beta method applied in SIMA for this work is presented in Table 3.1.

Table 3.1: Newmark-Beta parameters used for dynamic analysis in SIMA

Δt	0.1 s
β	0.256
γ	0.505

From the chosen value of γ it is seen that some numerical damping has been chosen. It is important not to introduce too large numerical damping as this typically comes at the expense of accuracy.

As iteration is required when using the Newmark-Beta method for the governing finite element equation in Equation 3.1, SIMA applies Newton-Raphson iteration. This is not elaborated here, but the method can be found in e.g. SINTEF Ocean (2017*a*).

3.4 Decay Test

A decay test is widely used in order to obtain structural or rigid body natural frequencies and system damping. For the bottom fixed monopile structure, the decay test will regard the structural natural frequencies and structural damping. The structure is given an initial static displacement away from its equilibrium, and then released to oscillate freely. When free oscillations are regarded, there should be no external excitation forces on the system after being released from initial displacement. For a monopile structure the decay test is usually performed for the fore-aft and side-side bending modes.

The natural frequencies can be obtained by studying the time series of the decay, or more effectively studied in the frequency-domain by performing a FFT.

The structural damping can be determined by different approaches. If the damping is assumed to be linear, the method of logarithmic decrement can be applied. Otherwise, if the damping has contributions from viscous effects, typically both linear and quadratic damping are desirable to determine. The method of logarithmic decrement is covered here as it is the method used in this work for determining structural damping, while a method for determining linear and quadratic damping can be studied in Bachynski (2014). The method of logarithmic decrement is a well established theory, but has in this work been based on the notation in Ahmed & Kandagal (2016). The free decay is assumed to be described on the form

$$x(t) = A\sin(\omega_d t + \phi)e^{-\xi\omega_n t} \tag{3.8}$$

Suppose the time series has $N + 1$ peaks, the first peak value is denoted x_1 and the last peak value is denoted x_{N+1} such that the last peak is located N periods of oscillation, T, after the first peak. Then the logarithmic decrement is given as

$$\delta = \frac{1}{N}\ln\left[\frac{x_1}{x_{N+1}}\right] \tag{3.9}$$

From this the damping ratio, i.e. the ratio between actual damping in the system and critical damping, is found as

$$\xi = \frac{\delta}{\sqrt{4\pi^2 + \delta^2}} \tag{3.10}$$

3.5 Eigenvalue Analysis

If free harmonic oscillations of an undamped system is considered $\vec{R}^{ext} = \vec{0}$ and $\boldsymbol{B} = \boldsymbol{0}$ so that the governing finite element equation in Equation 3.1 reduces to

$$\boldsymbol{M}\ddot{\vec{r}} + \boldsymbol{K}\vec{r} = \vec{0} \tag{3.11}$$

The motion of the system is assumed to be oscillatory with the same frequency for all points on the structure. The motion is then described by

$$\vec{r} = \vec{\Phi}\sin(\omega t) \tag{3.12}$$

The solution of Equation 3.11 is given by

$$(-\boldsymbol{M}\omega^2 + \boldsymbol{K})\vec{\Phi}\sin(\omega t) = \vec{0} \tag{3.13a}$$

$$(\boldsymbol{K} - \omega^2\boldsymbol{M})\vec{\Phi} = \vec{0} \tag{3.13b}$$

Equation 3.13b is referred to as an eigenvalue problem, where $\vec{\Phi}$ is the eigenvector that determines the mode of oscillation and ω is the natural frequency of the corresponding mode.

SIMA solves the eigenvalue problem through an eigenvalue analysis, for which it is possible to specify the number of modes to solve for. In this work the first three modal shapes were desirable to solve for. Figure 3.1 shows a sketch of the three first modal shapes in bending for a cantilever beam (Tejada 2009), which the bottom fixed monopile can be simplified as. It is expected that the modal shapes obtained from the eigenvalue analysis are very similar to those shown in the figure.

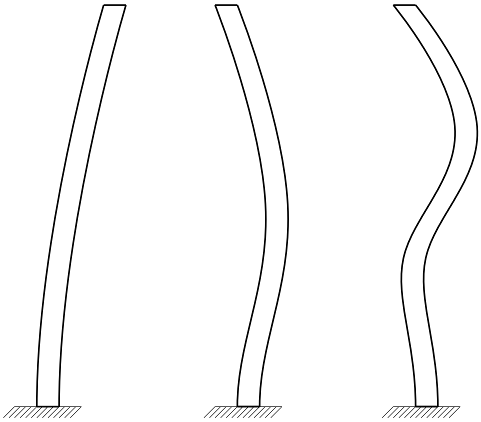

Figure 3.1: Sketch of the three first modal shapes in bending of a cantilever beam (increasing mode from left to right)

3.6 Simulation Model

As results from experiments are to be compared to numerical results, a well functioning simulation model is required. The simulation model has been built as a beam element model, which is appropriate for a slender structure, such as a monopile. A model was presented by the Supervisor as a starting point. However, verification and tuning of model properties had to be performed. The simulation model is built to resemble the actual structural model used in the experimental tests as closely as possible. Figure 3.2 shows a 3D-view picture of the how the simulation model is built in SIMA. The figure shows a monopile structure with uniform cross-section extending from the sea bottom through the still sea surface (transition between shaded and clear colours). Even though the area of the monopile is uniform along its length, the mass and stiffness properties are not equal along the length of the monopile. The reason for this is that the experimental model had measuring devices connected to it. The tower is connected to the monopile at the sea surface, and it has has varying cross-sections along its length, as well as varying mass and stiffness properties. The last components of the model are the drag disks, which are introduced to provide aerodynamic damping to the system. This is to resemble the aerodynamic damping provided by the wind turbine blades during environmental conditions with no wind. Since the flow around the blades of a wind turbine is associated with the Reynolds number, there are issues with scaling when attempting to take both Reynolds number and Froude number into account. Scaling is further discussed in Section 6.1. The introduction of drag disks simplifies the problem and reduces the cost compared to using a model wind turbine and blades. In this case, since the focus is put on wave induced loads and no wind loads are included in the experiments, drag disks were a reasonable solution.

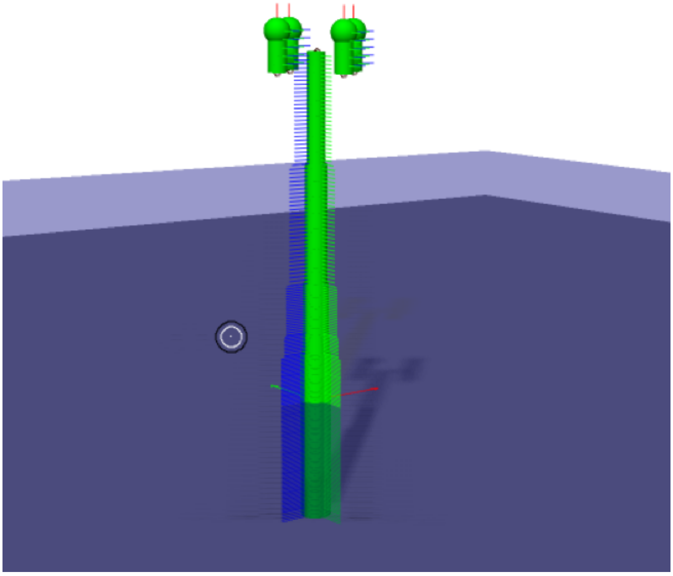

Figure 3.2: Simulation model, as modelled in SIMA

A brief overview of how the beam element model is defined in SIMA is summarized, although the modelling of the structure has not been the focus in this project thesis. For details beyond what is presented here about SIMA modelling, the reader is advised to seek out RIFLEX User Guide (SINTEF Ocean 2017*b*) (the documentation is only available with the computer software).

The topology of the system is defined by *supernodes*. Supernodes are connected by *lines*. The system topology is then uniquely determined by supernodes and lines. Boundary conditions are defined at supernodes and each supernode is classified as fixed or prescribed with respect to each degree of freedom, free (all degrees of freedom) or slaved with respect to which supernode. An overview of the supernodes used for the modelling is shown in

Table 3.2. The coordinates are defined with respect to a coordinate system placed in the centre of the monopile and at the mean water level. The drag disk nodes are connected rigidly to the structure, as they are slaved to the Nacelle supernode at both ends.

Table 3.2: Overview of the supernodes with their respective coordinates and boundary conditions

Supernode name	Boundary condition	Coordinate (x,y,z)
Nacelle_SN	Free	(0.0 , 0.0 , 87.6)
Seabed_SN	Free	(0.0 , 0.0 , -30.0)
UnderSoilSpring_SN	Fixed	(0.0 , 0.0 , -50.0)
DragDisk_1	Slaved (to Nacelle_SN)	(11.4 , 0.0 , 82.6)
DragDisk_1top	Slaved (to Nacelle_SN)	(11.4 , 0.0 , 92.6)
DragDisk_2	Slaved (to Nacelle_SN)	(-11.4 , 0.0 , 82.6)
DragDisk_2_top	Slaved (to Nacelle_SN)	(-11.4 , 0.0 , 92.6)
DragDisk_3	Slaved (to Nacelle_SN)	(0.0 , 11.4 ,82.6)
DragDisk_3_top	Slaved (to Nacelle_SN)	(0.0 , 11.4 , 92.6)
DragDisk_4	Slaved (to Nacelle_SN)	(0.0 , -11.4 , 82.6)
DragDisk_4_top	Slaved (to Nacelle_SN)	(0.0 , -11.4 , 92.6)
diskL	Free	(0.0 , 0.0 , 82.6)

An overview of how the different lines are defined is presented in Table 3.3.

Table 3.3: Overview of the lines connected by supernodes and the respective line lengths in meters

Line name	Line type	Supernode end 1	Supernode end 2	Line length
soilSpring	SoilSpring_LT	Seabed_SN	UnderSoilSpring_SN	20.0
tower	Tower_LT	diskL	Seabed_SN	112.6
towup	tipLT	Nacelle_SN	diskL	5.0
DragDiskLine5	DragDisk_LT	DragDisk_1	DragDisk_1top	10.0
DragDiskLine6	DragDisk_LT	DragDisk_2	DragDisk_2_top	10.0
DragDiskLine7	DragDisk_LT	DragDisk_3	DragDisk_3_top	10.0
DragDiskLine8	DragDisk_LT	DragDisk_4	DragDisk_4_top	10.0

Lines are as previously mentioned connected by two supernodes, and the table specifies which supernode is at the first and second end of the lines respectively. The line length follows from the absolute distance between the supernodes in question. For the simulation model in this work, all lines are defined vertically, i.e. by supernodes that have the same x- and y-coordinates. Each line is given its unique name. However, if a line has the same properties, it can take the same line type, as is the case for the drag disks, which are distributed symmetrically and thus have the same line length. This is convenient in terms of the system topology description.

Each line type is further divided into segments, which have uniform cross-section. Each segment is then divided into a number of elements of uniform length. These will be the finite elements. Figure 3.3 shows how the system definitions are built with regards to topology.

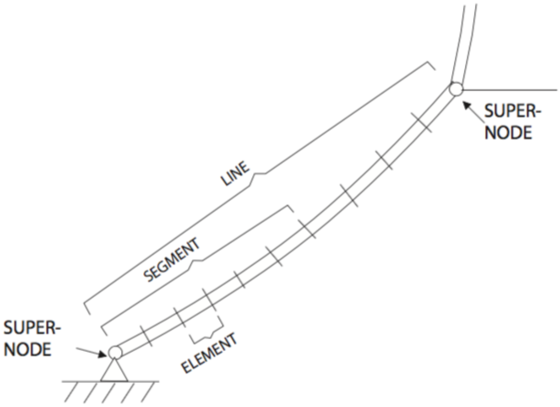

Figure 3.3: Definitions of the different definitions used to describe the system topology in SIMA. Taken from SINTEF Ocean (2017*b*)

All line types in this work have the same cross-section types. These are *generic axisymmetric pipes*, which can be defined with different properties, e.g. mass coefficient, external area, internal area, gyration radius, stiffness properties and damping properties. The finite elements defined as axisymmetric pipes are beam elements. It should be noted that the tower of an offshore wind turbine is usually defined from the sea surface and up, rather than the sea bed and up. The tower line in Table 3.3 has been defined from the seabed and up but this is only a modelling convention to limit the number of supernodes. The part of the structure from the sea surface and down is otherwise usually referred to as sea pile or monopile.

The drag disks must be given a mass to simulate the typically heavy top mass of a wind turbine. This is done by assigning a component nodal body to the end of the drag disk line type. The mass is set to 83975 kg (full scale) for each drag disk to be consistent with the model scale experiments.

Chapter 4

Wave Kinematics and Load Models

The external loads on a monopile supported wind turbine may come from several sources, e.g. waves, wind, current, soil-structure interaction effects, etc. Here, the focus is put solely on wave loads to investigate the response. A suitable wave theory must be chosen in order to calculate the wave loads on a structure. The choice of wave kinematics to be implemented are crucial in order to describe the response realistically. Both viscous effects and potential flow effects may be important in determining the wave-induced loads on a monopile (Faltinsen 1990). The potential flow loads include wave diffraction and radiation around the structure, while the viscous effects must be understood in terms of viscous drag, i.e. frictional effects, and viscous pressure drag, i.e. pressure forces due to separated flow. Both linear and second-order wave kinematics are considered for potential flow theory, as well as stretching techniques for linear theory. Nonlinear load models are also considered. This chapter is largely based on the work of Newman (1977) and Faltinsen (1990). Thus, for extensive details on the approach these two textbooks should be studied.

4.1 Potential Flow Theory

Potential theory assumes incompressible and inviscid fluid and irrotational flow. A velocity potential ϕ is defined to describe the velocity $\boldsymbol{V}(x, y, z, t) = (u, v, w)$ at time t and at a point $\boldsymbol{x} = (x, y, z)$ in a Cartesian coordinate system fixed in space. Thus it follows by definition that $\boldsymbol{V} = \boldsymbol{\nabla}\phi$. Due to the incompressibility of water, $\boldsymbol{\nabla V} = 0$, the velocity potential has to satisfy what is referred to as the Laplace equation.

$$\boldsymbol{\nabla}^2\phi = \frac{\partial^2\phi}{\partial x^2} + \frac{\partial^2\phi}{\partial y^2} + \frac{\partial^2\phi}{\partial z^2} = 0 \tag{4.1}$$

The pressure is obtained through the unsteady Bernoulli equation, where the only external force field is gravity and $z = 0$ is the mean free surface level. It is further assumed that the pressure at the free surface is the atmospheric pressure p_a.

$$p - p_a = -\rho g z - \rho\frac{\partial\phi}{\partial t} - \frac{\rho}{2}\boldsymbol{\nabla}\boldsymbol{\phi}^2 \tag{4.2}$$

The first term on the right hand side in Equation 4.2 is the hydrostatic pressure, while the last two terms are the dynamic linear and quadratic pressure.

Boundary conditions must be specified in the fluid domain. Typically the boundary conditions are specified as *kinematic boundary conditions* and *dynamic free-surface condition*. A kinematic boundary condition is specified for the sea bottom so that no fluid enters or leaves the sea bottom, which is referred to as impermeability. In effect there shall be no fluid flow normal to the sea bottom at the sea bottom.

$$\frac{\partial\phi}{\partial n} = 0 \qquad \text{on sea bottom} \tag{4.3}$$

For a body moving in the fluid, the kinematic boundary condition is also specified as an impermeability condition. Compared to Equation 4.3 the body can generally have a velocity $\boldsymbol{U}$, which is accounted for in Equation 4.4. The right hand side reduces to zero for a body fixed in space.

$$\frac{\partial\phi}{\partial n} = \boldsymbol{U}\cdot\boldsymbol{n} \qquad \text{on body surface} \tag{4.4}$$

The final kinematic boundary condition is specified for the free surface, which specifies that a fluid particle on the free surface $z = \zeta(x, y, t)$ remains there. Thus, the material derivative of $z - \zeta(x, y, z, t) = 0$ must be zero: $\frac{D[z-\zeta(x,y,z,t)]}{Dt} = 0$.

$$\frac{\partial\zeta}{\partial t} + \frac{\partial\phi}{\partial x}\frac{\partial\zeta}{\partial x} + \frac{\partial\phi}{\partial y}\frac{\partial\zeta}{\partial y} - \frac{\partial\phi}{\partial z} = 0 \qquad \text{on } z = \zeta(x, y, t) \tag{4.5}$$

The dynamic free-surface condition is specified by the water pressure being equal to the constant atmospheric pressure, and thus follows from Equation 4.2.

$$g\zeta + \frac{\partial \phi}{\partial t} + \frac{1}{2}\left(\left(\frac{\partial \phi}{\partial x}\right)^2 + \left(\frac{\partial \phi}{\partial y}\right)^2 + \left(\frac{\partial \phi}{\partial z}\right)^2\right) = 0 \quad \text{on } z = \zeta(x,y,t) \tag{4.6}$$

All that is stated up to this point is general for solving various higher order potential flow theories.

4.1.1 First-Order Potential Flow Theory

Both the free-surface condition in Equation 4.5 and Equation 4.6 are nonlinear and it is not known where the free surface is before the problem is solved. It is therefore useful to linearize the free-surface conditions which is what defines first-order potential flow theory, also known as linear wave theory or Airy wave theory, A perturbation approach is applied for the velocity potential and free surface elevation, where $\varepsilon = k\zeta_a$ is a measure of the wave nonlinearities.

$$\begin{aligned} \phi &= \underbrace{\tilde{\phi}_1 \varepsilon}_{\phi_1} + \underbrace{\tilde{\phi}_2 \varepsilon^2}_{\phi_2} + \underbrace{\tilde{\phi}_3 \varepsilon^3}_{\phi_3} + ... \\ \zeta &= \underbrace{\tilde{\zeta}_1 \varepsilon}_{\zeta_1} + \underbrace{\tilde{\zeta}_2 \varepsilon^2}_{\zeta_2} + \underbrace{\tilde{\zeta}_3 \varepsilon^3}_{\zeta_3} + ... \end{aligned} \tag{4.7}$$

The expressions in Equation 4.7 are substituted into the Laplace equation and boundary conditions, using Taylor expansion of the boundary conditions around the mean boundary configuration. Thus, the body motions and free-surface displacements are functions of power of ε and solutions can be found for each order. For first-order potential flow theory ε is assumed small and terms $\mathcal{O}(\varepsilon^n),\ n > 1$, are suppressed. Equation 4.5 and Equation 4.6 are linearized from the instantaneous free surface $z = \zeta(x,y,t)$ to the mean free surface $z = 0$.

$$\frac{\partial \zeta}{\partial t} = \frac{\partial \phi}{\partial z} \quad \text{on } z = 0 \quad \text{(kinematic condition)} \tag{4.8a}$$

$$g\zeta + \frac{\partial \phi}{\partial t} = 0 \quad \text{on } z = 0 \quad \text{(dynamic condition)} \tag{4.8b}$$

By differentiating Equation 4.8b with respect to time and combining with Equation 4.8a the combined free-surface condition is obtained for the velocity potential.

$$\frac{\partial^2 \phi}{\partial t^2} + g\frac{\partial \phi}{\partial z} = 0 \quad \text{on } z = 0 \tag{4.9}$$

The solution for the velocity potential, where x is a coordinate along the direction of propagation and z is the vertical coordinate defined positive upward, is found to be

$$\phi = \frac{g\zeta_a}{\omega} \frac{\cosh k(z+h)}{\cosh kh} \cos(\omega t - kx) \tag{4.10}$$

where g is the gravitational constant, ω is the circular frequency for which the velocity potential oscillates with (wave frequency), h is the water depth, $k = \frac{\omega}{V_p}$ is the wave number also defined by the wave length λ as $k = \frac{2\pi}{\lambda}$ and $V_p = \frac{\omega}{k}$ is the phase velocity which is the velocity a wave propagates with, i.e. for an observer moving with this velocity, the wave will appear steady-state. For Equation 4.10 to satisfy the free-surface condition it follows that

$$\omega^2 = gk \tanh kh \tag{4.11}$$

which is the frequency dispersion relation and relates the wave frequency and wave number. From this it is seen that the phase velocity becomes $V_p = \sqrt{\frac{g}{k} \tanh kh}$, from which it is evident that water waves are dispersive, i.e. longer waves (smaller wave number) will travel faster than shorter waves.

The first-order potential flow theory is valid for small amplitude waves with wave slope $k\zeta_a << 1$. The incident surface elevation for a propagating linearized wave is given by

$$\zeta(x,t) = \zeta_a \sin(\omega t - kx) \tag{4.12}$$

The pressure, assuming the ambient pressure to be $p_a = 0$, can be found from the linearized Bernoulli equation from Equation 4.2.

$$p = -\rho g z - \rho \frac{\partial \phi}{\partial t} = p_s + p_d \tag{4.13}$$

p_s is the static pressure and p_d is the dynamic pressure.

4.1.1.1 Wave Diffraction

After finding the potential for the incoming waves for the first-order potential flow assumption now referred to as ϕ_0 and given by Equation 4.10, it is desirable to find the solution of the wave-body interaction problem in terms of a velocity potential ϕ. With the assumption of linearity, the superposition principle is valid. Thus, the physical effects following the wave-body interactions can be divided into two sub-problems, referred to as the *diffraction problem* and *radiation problem*. In the diffraction problem the structure can be thought of as being fixed in all six degrees of freedom and interacting with the waves. In the radiation problem there are no incoming waves and the structure is forced to oscillate in its six degrees of freedom. The radiation problem will not be covered any further as it is related to the body generating waves, which is not very relevant for the bottom fixed monopile structure.

For the diffraction problem the velocity potential is described by the sum of the incident wave potential ϕ_0 and a diffraction potential ϕ_D.

$$\phi(x,y,z,t) = \phi_0(x,y,z,t) + \phi_D(x,y,z,t) \tag{4.14}$$

In related work (e.g. Faltinsen et al. (1995)) the potential in the diffraction problem is described with a different notation. The total potential is called the diffraction potential which is a sum of the incident wave potential and a scattering potential, so that $\phi_D = \phi_I + \phi_S$. Even though the notation is different, the physical meaning of the terms is equal to those in Equation 4.14. By comparison $\phi = \phi_D$, $\phi_0 = \phi_I$ and $\phi_D = \phi_S$ when comparing the two notations term by term. The latter convention is used when regarding the FNV model in Section 4.4.

The potential ϕ satisfies the impermeability condition for the body, as specified in Equation 4.4 for zero body velocity.

$$\frac{\partial \phi}{\partial n} = \frac{\partial(\phi_0 + \phi_D)}{\partial n} = 0 \qquad \text{on body surface} \tag{4.15}$$

The flow due to the incident wave potential (ϕ_0) penetrates the body as if it was not there, which causes loads on the body called Froude-Kriloff loads. To satisfy body impermeability the presence of the body causes a flow associated with the diffraction potential (ϕ_D), which causes loads on the body called diffraction loads. ϕ_D is not known but oscillates the opposite way of the incident waves, as seen from the impermeability condition. The sum of the two load components define the excitation loads on the body. The loads are obtained by dynamic pressure integration of the two potentials respectively, along the mean wetted body surface S_{0B} for each degree of freedom $k \in [1,6]$

$$F_{exc,k} = \underbrace{-\iint_{S_{0B}} \rho \frac{\partial \phi_0}{\partial t} n_k dS}_{\text{Froude-Kriloff loads}} \underbrace{-\iint_{S_{0B}} \rho \frac{\partial \phi_D}{\partial t} n_k dS}_{\text{Diffraction loads}} = F_{FK,k} + F_{D,k} \tag{4.16}$$

4.1.2 Second order Potential Flow Theory

Dean & Dalrymple (1984) uses the perturbation approach described in Equation 4.7, with $\varepsilon = k\zeta_a$, and applies this with the dynamic free surface condition from Equation 4.6 and kinematic free surface condition from Equation 4.5 on the free surface $z = \zeta(x, y, t)$. This differs from the first-order potential flow theory where the free surface conditions were linearized about the mean free surface $z = 0$. The dynamic and kinematic free surface conditions are combined into the combined free surface condition on the free surface $z = \zeta(x, y, t)$ and used to solve for the second order potential ϕ_2. The first order potential ϕ_1 is known from the solution of first-order potential flow theory and is not altered with additional terms with this approach. Terms of order $\mathcal{O}(\varepsilon^n),\ n > 2$, are suppressed to be consistent with second order theory. For the complete derivation of the second order velocity potential and surface elevation, Dean & Dalrymple (1984) should be studied. The results for the total velocity potential (given in Equation 4.17) and surface elevation (given in Equation 4.18) consistent to second order are reproduced here, for waves propagating in the x-direction.

$$\begin{aligned}\phi = \phi_1 + \phi_2 =& \frac{g\zeta_a}{\omega}\frac{\cosh k(z+h)}{\cosh kh} cos(\omega t - kx) \\ &+ \frac{3}{8}\zeta_a^2\omega\frac{\cosh 2k(z+h)}{\sinh^4 kh}\sin 2(\omega t - kx)\end{aligned} \tag{4.17}$$

$$\zeta = \zeta_1 + \zeta_2 = \zeta_a\cos(\omega t - kx) + \frac{1}{4}k\zeta_a^2\frac{\cosh kh}{\sinh^3 kh}(2 + \cosh 2kh)\cos 2(\omega t - kx) \tag{4.18}$$

The dispersion relation given in Equation 4.11 for first-order theory is valid also for second-order theory. However, the dispersion relation for third order will have a correction.

When having included terms of order $\mathcal{O}(\varepsilon^2)$, the boundary conditions are satisfied better than with first-order theory, and the error in the approximation is of order $\mathcal{O}(\varepsilon^3)$.

An example for the surface elevation for second-order potential flow theory, with $\zeta_a = 5\ m$, $T = 10\ s$ and $h = 30m$ is shown in Figure 4.1. When comparing the second-order surface elevation to the first-order surface elevation it is seen that the wave height is equal, but the crest height is higher and the trough depth is shallower. In addition the shape of the crests are steeper and the shape of the troughs are rounder than the first-order crests and troughs respectively. The shape of the second-order waves are closer to real surface waves, especially for large waves, as the first-order waves are usually only a good representation of small-amplitude waves.

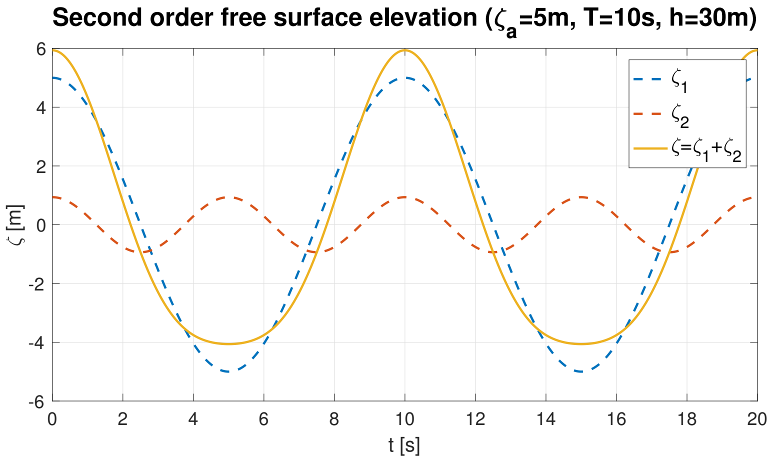

Figure 4.1: Example of surface elevation according to second-order potential flow theory (yellow) as a sum of the first-order wave elevation (blue) and the second-order correction (red)

4.2 Morison's Equation

Morison's equation is often used to estimate the loads on a slender structure in long waves, i.e. the diameter of the structure is small compared to the wave length, usually defined by $D < 0.2\lambda$. Morison's equation estimates the horizontal force on a fixed vertical circular cylinder (can also be used for other cross-sections with small modifications) as a sum of an inertia force and a drag force. The Morison force per unit length on a section dz of the cylinder is presented.

$$dF = \rho(1 + C_A)Aa_1dz + \frac{1}{2}\rho C_D D|u|udz = dF_M + dF_D \tag{4.19}$$

C_A and C_D denote the added mass and drag coefficients respectively, while u and a_1 are the horizontal wave particle velocity and acceleration respectively, taken at the midpoint of the cross-section. A is the projected area, which has normal vector parallel to u and a_1, and D is the diameter of the cylinder. The inertia force dF_M represents the Froude-Kriloff force. In the long-wave approximation (large λ/D) where diffraction effects are negligible the inertia term will be a good representation of the potential theory excitation force in Equation 4.16 as diffraction effects will be small. The relation between the added mass coefficient and the inertia coefficient is generally expressed as $C_M = 1 + C_A$, where C_M is the inertia coefficient. In the long wave limit, the value of the inertia coefficient can be shown to be $C_M = 2$, through comparison with the potential theory excitation force for a cylinder in long waves. The drag force dF_D represents the viscous effects. In particular the drag coefficient, but also the inertia coefficient, is dependent on many parameters and must generally be determined empirically, which is why the Morison equation is often referred to as semi-empirical. A formulation of Morison's equation taking into account that a body may be moving in the waves also exists, so that Equation 4.19 is modified with a relative velocity ($v_r = u - \dot{r}$, where $\dot{r}$ is the velocity of the moving body) and the acceleration due to body motions ($\ddot{r}$) is included (DNV GL 2017).

$$dF = -\rho C_A A\ddot{r}dz + \rho(1 + C_A)Aa_1 dz + \frac{1}{2}\rho C_D D|v_r|v_r dz \tag{4.20}$$

Equation 4.19 must be integrated over the water depth to obtain the total force on the vertical cylinder. A discussion may arise whether it should be integrated from the sea bottom (z=-d) up to the free surface $z = \zeta(t)$ or to the mean surface level (z=0). This is further regarded when discussing stretching of the wave potential.

4.2.1 MacCamy-Fuchs Correction for Diffraction

For large-volume structures, where the wave length is no longer large compared to the diameter (or characteristic length), i.e. for practical purposes $D < 0.2\lambda$ is no longer true, Morison's theory is inaccurate since diffraction effects must be taken into account. MacCamy & Fuchs (1954) introduced a correction of the inertia term for finite water depths. For better readability, the derivation is also presented in Chakrabarti (1987) with slightly different notation. The horizontal force is given as a function of ka, where a is the cylinder radius, which equivalently to the diameter-wavelength ratio gives an indication of the importance of the diffraction.

$$dF = \frac{4\rho g\zeta_a}{k}\frac{\cosh k(z+h)}{\cosh kh}\frac{1}{\sqrt{A_1(ka)}}cos(\omega t - \alpha) = C_M \rho \pi a^2 \dot{u}_\alpha \tag{4.21}$$

where

$$\begin{gathered} A_1(ka) = [J_1{}'(ka)]^2 + [Y_1{}'(ka)]^2 \\ \alpha = \tan^{-1}\frac{J_1{}'(ka)}{Y_1{}'(ka)} \end{gathered} \tag{4.22}$$

$J_1(ka)$ and $Y_1(ka)$ are the first order Bessel functions of first and second kind. The prime in Equation 4.22 denote differentiation. These functions of order n make up the general solution $y = a_1 J_n(x) + a_2 Y_n(x)$ to the differential equation $x^2 y'' + ny' + (x^2 - n^2)y = 0$. The mathematical description of wave-cylinder interaction generally includes Bessel functions. These functions are described in more detail in Chakrabarti (1987). As seen from Equation 4.21, the term is compared to the Morison equation so that the horizontal acceleration, u_α and inertia coefficient C_M are given by Equation 4.23 and Equation 4.24 respectively.

$$u_\alpha = gk\zeta_a \frac{\cosh k(z+h)}{\cosh kh} cos(\omega t - \alpha) \tag{4.23}$$

$$C_M = \frac{4}{\pi (ka)^2 \sqrt{A_1}} \tag{4.24}$$

4.3 Stretching of Wave Kinematics

Stretching of wave kinematics refers to methods of describing linear wave kinematics at the free surface $z = \zeta$, rather than at the mean water level $z = 0$, for which it is originally found at. This introduces a non-linear extension of the linear theory. There are in practice many ways of performing stretching, but *simple extrapolation* and *Wheeler stretching* will be covered in more detail. Both stretching methods are built-in methods in SIMA, and are applied when attempting to validate the wave forces on the monopile from the experimental tests.

4.3.1 Simple Extrapolation

The most simple stretching technique is the constant extrapolation of the wave kinematics. The first-order wave kinematics are kept constant from the mean surface level and up to the free surface. Thus, under a wave crest (or positive surface elevation in general) the mean surface level ($z = 0$) solutions for the pressure and velocities are applied, while under a wave trough (or negative surface elevation in general) the wave kinematics are used for the actual z-coordinate since the wave kinematics are valid for negative z-coordinates $z \leq 0$. The simple extrapolation stretching technique is illustrated in Figure 4.2. The dotted black lines indicate the first-order potential, while the solid black lines indicate the actual potential when stretching is accounted for, at a wave crest and wave trough respectively.

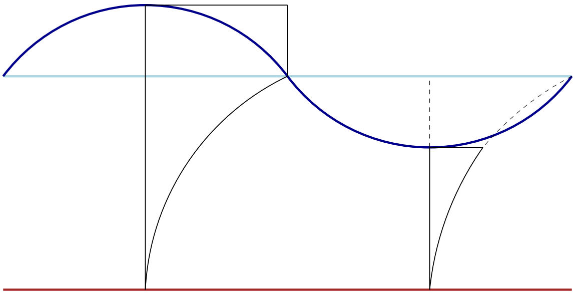

Figure 4.2: Simple extrapolation of the wave kinematics above the mean surface level

4.3.2 Wheeler Stretching

Wheeler (1970) introduced a stretching technique where the linear wave kinematics is shifted from the mean water level $z = 0$ to the actual free surface $z = \zeta$. This is commonly referred to as *Wheeler stretching* and in contrast to the simple extrapolation technique previously described, the wave potential keeps it form for z-coordinates below the free surface, as illustrated by Figure 4.3.

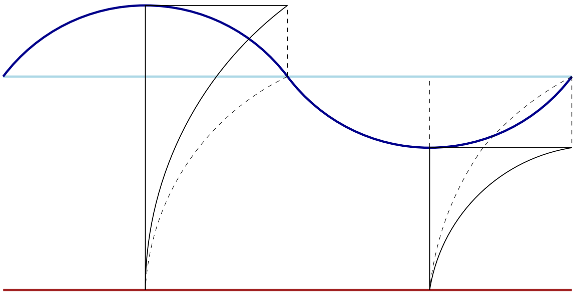

Figure 4.3: Wheeler stretching, where the linear wave potential is stretched above mean surface level and compressed below mean surface level

The actual stretching of the wave kinematics with Wheeler stretching comes in the form of stretching the vertical coordinate in the wave potential from Equation 4.10. The stretched vertical coordinate z' is given by

$$z' = (z - \zeta)\frac{h}{h + \zeta} \tag{4.25}$$

where $-h < z < 0$ and $-h < z' < \zeta$. h is the water depth and ζ is the free surface elevation given by Equation 4.12. By applying Wheeler stretching a non-linear extension of the first-order wave kinematics is obtained when integrating to find the horizontal forces on e.g. a monopile structure. Terms of order $\mathcal{O}(\zeta_a^2)$ will appear in the expression for the horizontal force, which are clearly non-linear.

4.4 FNV Model

The FNV formulation, named after the original authors Faltinsen, Newman and Vinje, describes the inertia load consistently up to the third order by utilizing the first and second order wave potentials. As described in Chapter 2, the theory assumes deep water, waves of amplitude similar to the cross-section of a vertical cylinder, and long waves such that the wave length is long compared to both the wave amplitude and the cylinder radius. These assumptions are formally summed up as $\zeta_a/a = \mathcal{O}(1)$, $k\zeta_a << 1$ and $ka << 1$ respectively, for a regular wave with amplitude ζ_a and wave number k interacting with a fixed vertical cylinder with radius a. A perturbation expansion is justified by the assumption of a large wave length compared to the wave amplitude and the perturbation approach is thus applied, analogous to what is described in Equation 4.7. Viscous effects are neglected and potential flow is assumed. Hence, if comparing to Morison's equation, only the inertia term is regarded.

For details on the derivation of the FNV formulation, the original paper (Faltinsen et al. 1995) should be visited. Only a brief overview is summarized here. An inner domain with length scales comparable to the cylinder radius a and an outer domain with length scales comparable to the wave length λ is regarded. In the linear analysis the total potential is given as $\phi_D = \phi_I + \phi_S$, where both potentials are described as the real value of the complex forms. Moreover, the scattering potential is defined for both the inner and outer domain. Next, the nonlinear scattering potential ψ is defined, which includes terms of third order in combinations of ζ_a and a. Terms of fourth order are omitted. The resulting potential is given by $\phi = \phi_D + \psi$, i.e. as a sum of the linear and second-order potentials. From the total potential, the forces are found by integrating the fluid pressure. The theory was extended to irregular waves by Newman (1996) and the results for irregular waves are reproduced here with the notation based on Krokstad et al. (1998).

$$\begin{aligned} F_{FNV} &= F_1 + F_2 + F_3 \\ &= 2\pi\rho a^2 \int_{-\infty}^{0} u_t dz \\ &+ 2\pi\rho a^2 \left. u_t \right|_{z=0} \zeta^{(1)} + \pi\rho\, a^2 \int_{-h}^{0} w u_z dz \\ &+ \pi\rho a^2 \zeta^{(1)} \left. \left(u_{tz}\zeta^{(1)} + w u_z - \frac{2}{g} u_t w_t \right) \right|_{z=0} \\ &+ \pi\rho \frac{a^2}{g} u^2 u_t|_{z=0} \beta(h/a) \end{aligned} \tag{4.26}$$

h is the cylinder draft, i.e. water depth for a bottom fixed cylinder, ω is the circular frequency of the waves, $\zeta^{(1)}$ is the first order wave elevation and u and w are the first-order particle velocity components.

$$\beta(h/a) = \int_{0}^{(h/a} [3\Psi_1(Z) + 4\Psi_2(Z)] dZ \tag{4.27}$$

where Ψ_1 and Ψ_2 are defined in Newman (1996). $\beta(h/a) \to 4$ when $h/a \to \infty$, i.e. when the draft of the cylinder is much longer than the radius.

4.5 Added Mass and Drag Coefficients

As the structure is subjected to loads in water, it is important to determine the added mass of the wet cross-sections. As the loads on the monopile structure is typically described by the Morison equation in Equation 4.19, it also is important to determine the drag coefficient of the wet cross-sections. As a starting point to tune the simulation model properties to be equal to the experimental test properties the added mass and drag coefficients have been determined through the approach described in DNV GL (2017).

For high Reynolds number ($Re > 10^6$), which is typically the case for a structure subjected to ocean waves where the kinematic viscosity is $\nu \sim \mathcal{O}(10^{-6})$, the drag coefficient is dependent on the Keulegan-Carpenter (K_C) number and the surface roughness of the monopile. The K_C number describes the importance of drag forces over inertia forces in an oscillatory flow.

$$K_C = \frac{UD}{T} \tag{4.28}$$

where U is the amplitude of the oscillatory fluid velocity, D is the member diameter and T is the period of oscillation.

For smooth members the drag coefficient is taken as $C_{DS} = 0.65$. A correction is made to the drag coefficient for $K_C < 12$, through the wake amplification factor $\psi(K_C)$. Equation 4.30 is illustrated by Figure 4.4.

$$C_D = C_{DS} \cdot \psi(K_C) \tag{4.29}$$

where

$$\psi(K_C) = \begin{cases} C_\pi + 0.10(K_C - 12) & 2 \leq K_C < 12 \\ C_\pi - 1.00 & 0.75 \leq K_C < 2 \\ C_\pi - 1.00 - 2.00(K_C - 0.75) & K_C \leq 0.75 \end{cases} \tag{4.30a}$$

$$C_\pi = 1.50 - 0.024(\frac{12}{C_{DS}} - 10) \tag{4.30b}$$

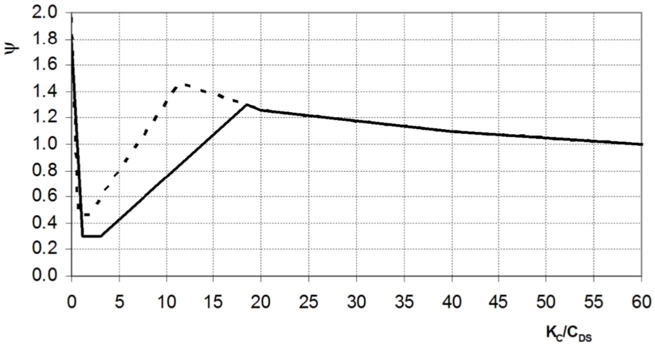

Figure 4.4: Selection of wake amplification factor, ψ, as a function of the ratio of K_C and C_{DS} for smooth (solid line) and rough cylinder (dotted line). Taken from DNV GL (2017).

The added mass coefficient for a smooth cylinder with $C_{DS} = 0.65$ is also dependent on the K_C number. Equation 4.31 is illustrated by Figure 4.5, where $C_M = 1 + C_A$.

$$C_A = \begin{cases} 1 & KC < 3 \\ \max \begin{Bmatrix} 1.0 - 0.044(K_C - 3) \\ 0.6 \end{Bmatrix} & KC \geq 3 \end{cases} \tag{4.31}$$

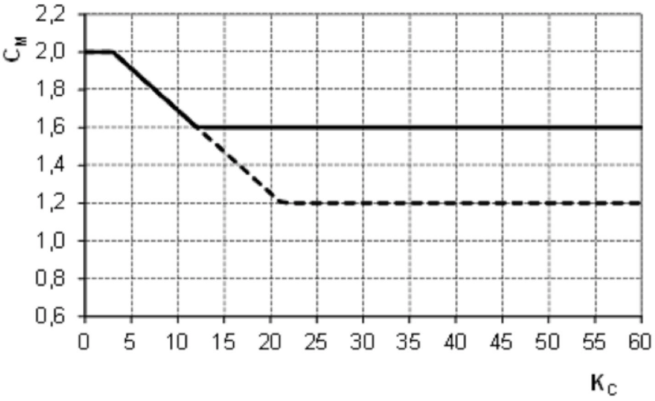

Figure 4.5: Selection of added mass coefficient, C_A, as a function of K_C for smooth (solid line) and rough cylinder (dotted line). Taken from DNV GL (2017).

In order to determine the values of the drag and added mass coefficients, it is necessary to determine the K_C number. As both the diameter of the monopile, $D = 7\ m$, and the period of the wave, T, are known parameters, only the amplitude of the velocity, U, must be considered. By assuming first-order potential flow theory the horizontal velocity follows from the potential in Equation 4.10.

$$u(x,z,t) = \frac{\partial \phi}{\partial x} = \omega \zeta_a \frac{\cosh(k(z+h))}{\sinh(kh)} \sin(\omega t - kx) \tag{4.32}$$

The maximum velocity amplitude is given for $z = 0$ and the maximum velocity is rewritten by application of the dispersion relation in Equation 4.11.

$$u_{\max} = \omega \zeta_a \frac{1}{\tanh(kh)} = \frac{gk}{\omega} \zeta_a = \frac{gT}{\lambda} \zeta_a \tag{4.33}$$

The wave length is determined as an iterated function through the dispersion relation in a water depth of $h = 30\ m$ for a known wave period T.

$$\lambda = \frac{g}{2\pi} T^2 \tanh(\frac{2\pi h}{\lambda}) \tag{4.34}$$

The choices of coefficients to be implemented in SIMA will be further discussed in Chapter 6.

Chapter 5

Stochastic Processes

A structure placed in the ocean, such as an offshore wind turbine, will be subjected to environmental loads, e.g. wave and wind loads, which are inherently random. It is therefore necessary describe ocean waves, which will be the focus here, from a probabilistic perspective, i.e. as a stochastic process. A stochastic process $X(t)$ is a random function of time, which has realizations with a random value for all time t. A random value x_i at time t_i cannot be given with certainty, but must be predicted with a certain probability to lie within certain limits.

A stochastic process is *stationary* if across an ensemble (collection of realizations) of the process, its mean value $\mu_X = E[X(t)]$, standard deviation $\sigma_X = \sqrt{E[(X(t) - \mu_X)^2]}$ and autocorrelation function $R_{XX}(t_1, t_2) = E[X(t_1)X(t_2)]$ are independent of absolute time. Thus, the mean value and standard deviation are constant for all values of t and the autocorrelation function is a function of the time difference $\tau = t_2 - t_1$ so that $R_{XX}(\tau) = E[X(t)X(t + \tau)]$ (Chakrabarti 1987). A process is further called an *ergodic* process if in addition to the ensemble averages being stationary, the averages along a single sample are equal to the ensemble averages. Thus, stationarity is a requirement for an ergodic process (Newland 1993). The assumptions of stationarity and ergodicity are important assumptions when studying short-term statistics of ocean waves, and are used as assumptions further on.

5.1 Autocorrelation Function and Spectral Density Function

The autocorrelation function, assuming ergodicity, is the time average of the product of a stochastic process at times t and $t + \tau$. As previously stated, the autocorrelation function is only dependent on the time shift τ.

$$R_{XX}(\tau) = E[X(t)X(t+\tau)] = \lim_{T\to\infty} \frac{1}{2T} \int_{-T}^{T} x(t)x(t+\tau)dt \tag{5.1}$$

Some important properties of the autocorrelation function are listed below.

1. R_{XX} is an even function so that $R_{XX}(\tau) = R_{XX}(-\tau)$.

$$\begin{aligned} R_{XX}(-\tau) &= \lim_{T\to\infty} \frac{1}{2T} \int_{-T}^{T} x(t)x(t-\tau)dt \\ &= \lim_{T\to\infty} \frac{1}{2T} \int_{-T}^{T} x(u+\tau)x(u)du = R_{XX}(\tau) \end{aligned} \tag{5.2}$$

2. R_{XX} has a maximum for $\tau = 0$

$$\begin{gathered} \lim_{T\to\infty} \frac{1}{2T} \int_{-T}^{T} \{x(t) - x(t+\tau)\}^2 dt = \lim_{T\to\infty} \frac{1}{2T} \int_{-T}^{T} \{x(t)\}^2 dt \,... \\ -2 \lim_{T\to\infty} \frac{1}{2T} \int_{-T}^{T} \{x(t)x(t+\tau)\}^2 dt + \lim_{T\to\infty} \frac{1}{2T} \int_{-T}^{T} \{x(t+\tau)\}^2 dt \,... \\ = R_{XX}(0) - 2R_{XX} + R_{XX}(0) \geq 0 \\ R_{XX}(0) \geq R_{XX}(\tau) \end{gathered} \tag{5.3}$$

3. $R_{XX}(0)$ is equal to the variance of a process with zero mean.

$$R_{XX}(0) = E[X(t)^2] = \lim_{T\to\infty} \frac{1}{2T} \int_{-T}^{T} \{x(t)\}^2 dt = \sigma_X^2 \tag{5.4}$$

One can notice that the magnitude of the autocorrelation function for $\tau = 0$ represents the time average of the power or energy of the random process (Ochi 1990).

In many cases it may be desirable to investigate the stochastic process in the frequency domain. The link between a function in the time domain and the corresponding function in the frequency domain, is the Fourier transform. The Fourier transform pair presented here is the complex form for a non-periodic function and is based on the notation in Ochi (1990). The Fourier transform pair is denoted by $f(t) \leftrightarrow F(\omega)$, so that $F(\omega)$ is called the Fourier transform of $f(t)$, denoted by $F(\omega) = \mathscr{F}\{f(t)\}$, and $f(t)$ is the inverse Fourier transform of $F(\omega)$, denoted by $f(t) = \mathscr{F}^{-1}\{F(\omega)\}$.

$$f(t) = \frac{1}{2\pi} \int_{-\infty}^{\infty} F(\omega) e^{i\omega t} d\omega \tag{5.5a}$$

$$F(\omega) = \int_{-\infty}^{\infty} f(t) e^{-i\omega t} dt \tag{5.5b}$$

In general the condition for existence of the Fourier transform of f(t) is

$$\int_{-\infty}^{\infty} |f(t)| dt < \infty \tag{5.6}$$

Some important properties of the Fourier transform are summarized in Ochi (1990). These properties will not be listed in this work but will be applied and referred to when the Fourier transform is utilized.

For a sample function $x(t)$ of a stationary stochastic process, the condition for the Fourier transform in Equation 5.6 will not be satisfied. The difficulty of directly analysing the sample function in the frequency domain is overcome by taking the Fourier transform of the autocorrelation function $R_{XX}(\tau)$. The autocorrelation function indirectly gives the information about the frequencies in a random process, as it evaluates the correlation between the sample function at time t and a time shift τ later, for all values of τ. Hence, the autocorrelation function reflects for which values of τ the process is in phase and anti-phase, and to what degree. If the random process is shifted so that the mean value of the process is zero, it can be assumed that the autocorrelation function goes to zero as the time shift, τ, becomes large, i.e. there is no correlation between a value of the sample function at time t and at time $t + \tau$ when τ becomes large. Then the integral in Equation 5.6 will be finite for the autocorrelation function and the Fourier transform can be applied (Newland 1993).

The spectral density function, $S_{XX}(\omega)$, of a random process, $x(t)$, describes the distribution of energy into frequency components, ω. The spectral density function is defined as

$$S_{XX}(\omega) = \lim_{T \to \infty} \frac{1}{2T} |X(\omega)|^2 \tag{5.7}$$

The relationship between the autocorrelation function and the spectral density function is explained by the Wiener-Khintchine theorem (Ochi 1990) and utilizes the Fourier transform. The starting point is to take the Fourier transform of the autocorrelation function, given in Equation 5.1.

$$\begin{aligned}\int_{-\infty}^{\infty} R_{XX}(\tau)e^{-i\omega\tau}d\tau &= \lim_{T\to\infty}\frac{1}{2T}\int_{-\infty}^{\infty}\int_{-\infty}^{\infty} x(t)x(t+\tau)e^{-i\omega\tau}dtd\tau \\ &= \lim_{T\to\infty}\frac{1}{2T}\int_{-\infty}^{\infty}\int_{-\infty}^{\infty} x(t)x(t+\tau)e^{-i\omega(t+\tau)}e^{i\omega t}dtd\tau \\ &= \lim_{T\to\infty}\frac{1}{2T}X(\omega)X^*(\omega) = \lim_{T\to\infty}\frac{1}{2T}|X(\omega)|^2\end{aligned} \tag{5.8}$$

$X^*(\omega)$ is the complex conjugate of the process in the frequency domain $X(\omega)$. From Equation 5.8 it is seen by comparison to Equation 5.7 that the autocorrelation function and spectral density function are related through the Fourier transform and inverse Fourier transform, so that they make up a Fourier transform pair.

$$\begin{aligned}S_{XX}(\omega) &= \int_{-\infty}^{\infty} R_{XX}(\tau)e^{-i\omega\tau}d\tau \\ R_{XX}(\tau) &= \frac{1}{2\pi}\int_{-\infty}^{\infty} S_{XX}(\omega)e^{i\omega T}d\omega\end{aligned} \tag{5.9}$$

The definitions of the spectrum presented here are based on a two-sided spectrum, i.e. the definitions are valid for both positive and negative frequencies. In practice, working with negative frequencies does not make sense. From the definition of the spectral density function it can be shown that it is an even function.

$$\begin{aligned}S_{XX}(-\omega) &= \lim_{T\to\infty}\frac{1}{2T}X(-\omega)X^*(-\omega) = \lim_{T\to\infty}\frac{1}{2T}X^*(\omega)X(\omega) \\ &= \lim_{T\to\infty}\frac{1}{2T}|X(\omega)|^2 = S_{XX}(\omega)\end{aligned} \tag{5.10}$$

Thus, the definition of the two-sided spectrum in Equation 5.9 can be multiplied by a factor of two and be defined for positive frequencies only. This is also the case for the autocorrelation function which can be defined for positive time shifts only.

The moments of the spectrum, m_k, are useful properties as many statistical characteristics are defined based on the moment. The definition in Equation 5.11 is based on the one-sided spectrum and will be used in further discussions.

$$m_k = \int_{0}^{\infty} \omega^k S(\omega)d\omega \tag{5.11}$$

5.2 Statistical Description of Waves

The incident surface velocity profile, given in Equation 4.12, is defined for linear theory, and describes regular, deterministic waves. To describe the inherent randomness of ocean waves, the incident surface elevation must be generalized to describe long-crested irregular sea (propagating along the positive x-axis with a constant surface elevation along the y-axis). The surface elevation of a long-crested irregular sea can be written as the sum of a large number of linear wave components (Faltinsen 1990).

$$\zeta = \sum_{j=1}^{N} A_j sin(\omega_j t - k_j x + \epsilon_j) \tag{5.12}$$

A_j, ω_j, k_j and ϵ_j are respectively the wave amplitude, wave frequency, wave number and random phase angle (uniformly distributed on the interval [0,2π]) of wave component j. ω_j and k_j are related by the dispersion relation, given in Equation 4.11, which is dependent on water depth.

The wave amplitude can be expressed by a wave spectrum $S_W(\omega)$ (one-sided spectrum with only positive frequencies) and by its frequency content. The wave spectrum is discretized into N components with constant difference between successive frequencies, $\Delta\omega$. Then the wave amplitude for each component, j is found through the following relation

$$\frac{1}{2}A_j^2 = S_W(\omega_j)\Delta\omega \tag{5.13}$$

The instantaneous wave elevation is assumed to be Gaussian distributed with zero mean and variance σ_W^2. The variance can be shown to be equal to the area under the spectrum (Faltinsen 1990) and is thus equal to the 0^{th} moment of the spectrum according to Equation 5.11. Compared to the discrete formulations above, Equation 5.14 assumes $N \to \infty$ and $\Delta\omega \to 0$.

$$\sigma_W^2 = \int_0^\infty S_W(\omega) d\omega \tag{5.14}$$

In this statistical description of waves, stationarity has been assumed. In practice this means that a limited time period is regarded for which the properties describing a sea state may be assumed to be constant, from $\frac{1}{2}$ to maybe 10 hours. However a time period of 3 hours is frequently applied. This is referred to as a short-term description of the sea

(Faltinsen 1990).

There are also methods of implementing irregular sea based on second order wave theory. The regular second-order potential flow theory waves in Section 4.1.2 cannot be summed together in the same manner as described above for first-order potential flow theory waves. The principle of superposition of different regular wave components can only be applied for linear waves. SIMA has a built-in approach for implementing irregular sea for second order waves. The implementation in SIMA for long-crested waves is not reproduced here but is based on the approach in Marthinsen & Winterstein (1992).

5.2.1 Wave Spectra

There are many standardized wave spectra that approximate the real wave spectrum, as the real wave spectrum is usually not known for the wanted area and/or weather conditions. These are based on measurements of wave data and cannot be expected to represent the actual wave spectrum for all frequencies. Some spectra that are commonly used are the Pierson-Moskowitz, ITTC, ISSC, JONSWAP and Torsethaugen spectra (Myrhaug 2007). The PM, ITTC and ISSC spectra are all applicable for fully developed sea states at open sea. They are single-peaked and describe sea states that are generated by local wind. The Torsethaugen spectrum is a two-peaked spectrum which is applicable in areas where there is an important swell component in addition to wind generated sea.

The JONSWAP spectrum is also a single-peaked spectrum which describes wind generated sea. In contrast to the other single-peaked spectra, the JONSWAP spectrum is applicable for developing sea. It is the most used spectrum in the North Sea as it is based on measurements from the South-Eastern area of the North Sea. The JONSWAP spectrum is defined as

$$S_J(\omega) = \frac{\alpha g^2}{\omega^5} \exp\left[-\frac{5}{4}\left(\frac{\omega_p}{\omega}\right)^4\right] \gamma^{a(\omega)} \tag{5.15}$$

where

$$\begin{aligned} a(\omega) &= \exp\left[-\frac{1}{2}\left(\frac{\omega-\omega_p}{\sigma\omega_p}\right)^2\right] \\ \sigma &= \begin{cases} 0.07, & \text{for} \quad \omega \leq \omega_p \\ 0.09, & \text{for} \quad \omega > \omega_p \end{cases} \end{aligned} \tag{5.16}$$

α is a spectral parameter that relates to the wind speed and fetch length, ω_p is the peak frequency for which the spectrum is at its maximum, γ is a peakedness parameter. Hasselmann et al. (1973), who originally established the JONSWAP spectrum, have given the mean value for the peakedness parameter as $\bar{\gamma} = 3.3$, and the given values for σ in Equation 5.16.

A sea state is usually described by the significant wave, H_s and the peak period, T_p. The significant wave height is defined as the mean value of the one-third largest wave heights during a short-term sea state (usually 3 hours as previously mentioned), and the peak period is the period for which the spectrum is at its maximum value, i.e. the period with the most energy in the sea state. The two parameters are related to the spectrum as follows.

$$\begin{aligned} H_s &= 4\sqrt{m_0} \\ T_p &= \frac{2\pi}{\omega_p} \end{aligned} \tag{5.17}$$

For some parametrizations of the JONSWAP spectrum the parameters α and γ depend on the significant wave height and peak period (Myrhaug 2007).

The spectrum used for generating the waves in this work is the TMA spectrum. The TMA spectrum was developed by Hughes (1984) for finite water depths and is similar to the JONSWAP spectrum. The difference between the two spectra is that the TMA spectrum accounts for the water depth, h, by a factor $\Phi(\omega, h)$.

$$S_{TMA} = S_J \Phi(\omega, h) \tag{5.18}$$

where

$$\begin{aligned} \Phi(\omega, h) &= \frac{(k(\omega, h))^{-3} \frac{\partial k(\omega, h)}{\partial \omega}}{(k(\omega, \infty))^{-3} \frac{\partial k(\omega, \infty)}{\partial \omega}} \\ k(\omega, h) &= \frac{\omega}{\sqrt{gh}} \end{aligned} \tag{5.19}$$

The expression for $k(\omega, h)$ is found through the shallow water limit (limit as $h \to 0$) for the dispersion relation in Equation 4.11.

5.3 Structural Response Statistics

When considering the response of a structure subjected to irregular waves, it is necessary to investigate the statistical description of the response. This is typically done in the frequency domain by investigating the spectrum of the response. For a linear system subjected to linear loads the response spectrum is related to the force spectrum through the frequency response function (e.g. Naess & Moan (2012), Ochi (1990), Newland (1993)). However, there are often nonlinearities in the structural model or the forces such that the method concerning the frequency response function is not valid. In this work, the structural model of the monopile may arguably be approximated as a linear system, but nonlinearities in the loads are a certainty. In this case the response spectra are calculated by taking the Fourier transform of the autocorrelation function of the response time series.

For a linear system subjected to harmonic loads assuming linear wave theory, the wave forces are proportional to the wave amplitude. In this case the frequency of the response will be equal to the wave frequency. For this cases it has become customary to compare the response to the wave amplitude in stead of the wave force. The function that relates the response amplitude to the wave amplitude is defined as the response amplitude operator (RAO), and is analogous to the frequency response function. If the excitation is a harmonic input with constant amplitude, $x(t) = x_0 \sin(\omega t)$ and is applied to a linear system the response will be given by $y(t) = \sin(\omega t - \phi)$, where ϕ represents a phase shift in the response compared to the excitation (Newland 1993). The RAO is then defined as

$$RAO(\omega) = \frac{y_0}{x_0} \tag{5.20}$$

The RAO is established by considering linear regular waves, and computed for all available frequencies.

Chapter 6

Experimental Test and Simulation Procedure

The experimental tests conducted in conjunction with this work were performed by SINTEF Ocean through the NOWITECH project. Some limited overview of the relevant information for this work will be presented. Extensive information about the experimental test setup can be found in the NOWITECH test report (Thys 2017).

When post-processing of data is regarded, the location at $z = -28.5\ m$ is hereafter referred to as *mudline* as it is the closest location to the sea bottom at $z = -30\ m$ for which results from the experimental tests are measured. Similarly $z = 1.5\ m$ is hereafter referred to as *waterline* since it is the closest location to the mean surface level at $z = 0\ m$ for which results from the experimental tests are measured. Many other locations on the monopile, such as top of the tower, could be interesting to investigate but the aforementioned locations, mudline and waterline, were deemed the most interesting in this work. The experimental results have measurements for moment, shear force and accelerations. However, only the moment results are considered as part of this work. The shear force results were determined by differentiating the moment results, and were deemed to be not as accurate as desired.

6.1 Scaling

Performing model tests can be valuable for confirmation of system behaviour, estimating extreme responses, evaluating non-linear phenomena, comparison with numerical simulations and understanding flow phenomena to name a few aspects. When performing model tests the question of what to take into considerations when scaling the model arises. For the results in model scale to be applicable in full scale, *similitude* must be achieved. Three similarity criteria defines similitude.

1. *Geometric similarity*: The shape of the full (F) scale and model (M) scale structures should be the same. Thus all linear dimensions must be scaled according to the same scaling ratio $\lambda = \frac{L_F}{L_M}$. This requirement also applies to the environment surrounding the structure and elastic deformations.
2. *Kinematic similarity*: There should be a similarity in velocities and accelerations so that the incoming flow will have geometrically similar motions in model and full scale. As an example the velocity in the x- and y-direction must have the same ratio, ensuring that a circular motion in full scale is also a circular motion in model scale.
3. *Dynamic similarity*: The ratios between different forces in full scale must be the same in model scale. Force contributions of importance include inertia, viscous, gravitational and pressure forces, elastic forces in the fluid (compressibility) and surface forces. If geometric similarity and dynamic similarity are fulfilled, kinematic similarity automatically follows.

In practice it is difficult to satisfy different scaling criteria simultaneously in a model test. Often the similarity in the ratio between inertia forces and gravity forces is reasonable to apply. This ratio is widely known as the *Froude number* (Fn) and is given in Equation 6.2.

$$\frac{\text{Inertia force}}{\text{Gravity force}} = \frac{F_i}{F_g} \propto \frac{\rho U^2 L^2}{\rho g L} = \frac{U^2}{gL} \tag{6.1}$$

The dynamic similarity requirement between model and full scale then requires

$$\begin{gathered} \frac{U_M^2}{gL_M} = \frac{U_F^2}{gL_F} \\ \frac{U_M}{\sqrt{gL_M}} = \frac{U_F}{\sqrt{gL_F}} = Fn \end{gathered} \tag{6.2}$$

Similarity for Froude number in model and full scale will ensure that the gravity forces are scaled appropriately. Keeping in mind that surface waves are gravity-driven, the equality in Froude number will ensure that wave forces are correctly scaled, which is desirable when studying a fixed monopile in waves. Another quantity that may be of importance if viscous forces are expected to be of importance is the Reynolds number Re, which gives the ratio between inertia forces and viscous forces.

$$Re = \frac{UD}{\nu} \tag{6.3}$$

where U is the fluid velocity, D is the diameter of the member and ν is the fluid kinematic viscosity.

Typically, equality in Reynolds number will give correct scaling of viscous forces. However, performing Froude scaling and Reynolds scaling at the same time is impossible in model scale, since the viscosity of the fluid in model scale has to be taken as a very low number, which becomes unrealistic to achieve practically.

For the monopile structure subjected to wave loads in this work, Froude scaling has been applied. A summary of how different physical quantities are scaled when using Froude scaling is given in Table 6.1. ρ_M and ρ_F denotes the density of water in respectively model scale and full scale.

Table 6.1: Froude scaling of selected physical parameters

Physical parameter	**Unit**	**Scaling factor**
Length	[m]	λ
Time	[s]	$\lambda^{\frac{1}{2}}$
Frequency	[Hz]	$\lambda^{-\frac{1}{2}}$
Structural mass	[kg]	$\lambda^3 \cdot \frac{\rho_F}{\rho_M}$
Force	[N]	$\lambda^3 \cdot \frac{\rho_F}{\rho_M}$
Moment	[Nm]	$\lambda^4 \cdot \frac{\rho_F}{\rho_M}$

A scaling factor of $\lambda = 40$ was used for the model in the experiments. In addition a factor of $\frac{\rho_F}{\rho_M} = 1.025$ reflected the ratio between the density of salt water (for full scale) and fresh water (for model scale). Thus, all experimental results that were obtained in model scale have been scaled according to Table 6.1 with the presented parameters.

6.2 Filtering

Filtering can be a useful tool when working with dynamic systems, e.g. in order to sort data at different frequencies or removing unwanted components from the data. Filtering is especially important when working with experimental results as data from experiments typically are affected by unwanted noise. Noise can contaminate data through measurement noise, typically introduced through the accuracy of the sensors making measurements, or through process noise, i.e. undesired dynamics of the system (Steen 2014).

Filters are typically split into four types: lowpass, highpass, bandpass and bandstop. The generic graphical representation of these filters are shown in Figure 6.1.

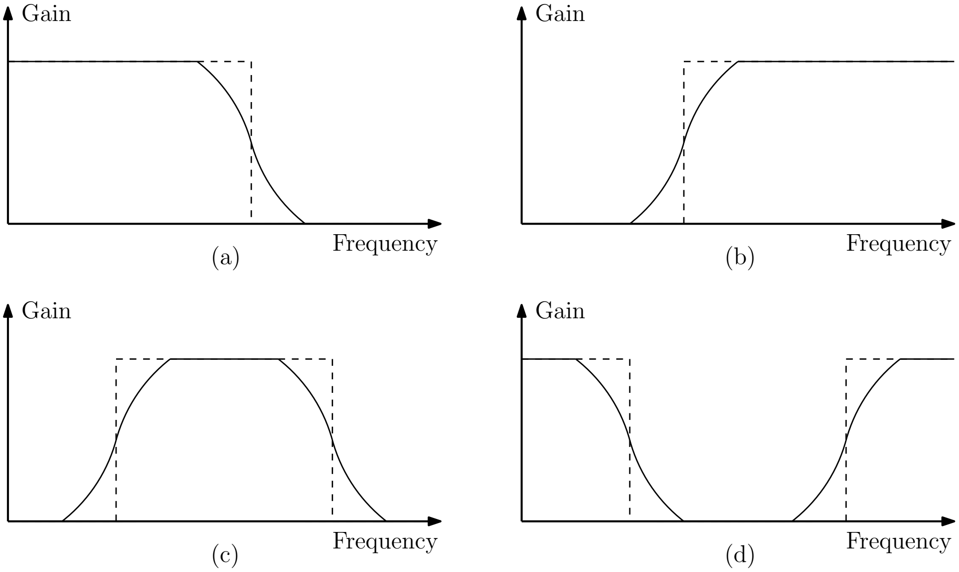

Figure 6.1: The four main types of filters: lowpass (a), highpass (b), bandpass (c) and bandstop (d). The dotted line represents an ideal filter, while the solid line represents a more realistic filter.

The lowpass filter lets low frequencies pass (passband) and attenuates high frequencies (stopband). The lowpass filter typically has a cut-off frequency, ω_c, for which higher frequencies are filtered out. In reality there is no single cut-off frequency where the signal is cut off, which would ideally be preferable. The signal is typically damped out during a small band of frequencies. Therefore, there are different definitions of the cut-off frequency. A definition that is frequently used is that the cut-off frequency is the frequency where the amplitude of the input signal is reduced to half at the output (Winder 2002).

The difference between an ideal filter and a more realistic filter is marked in Figure 6.1. The highpass filter is the opposite of the lowpass filter and lets high frequencies pass while low frequencies are attenuated. The bandpass filter and bandstop filters can in many cases be looked upon as combinations of a lowpass filter and a highpass filter. The bandpass filter attenuates both low and high frequencies and lets a band of frequencies pass, while the bandstop filter attenuates a band of frequencies and lets low and high frequencies pass.

Filters can be classified in different manners. In this work only linear, time-invariant filters are regarded. Further, filters can be analogue, applied on continuous time signals, or digital, applied on discrete-time (sampled) signals. In practice when working on data from experiments or simulations, these will be discrete-time signals. Hence digital filters are applied in typical post-processing tasks.

A filtered signal and the original signal are related by the filter transfer function, $H(i\omega)$ (where i is the imaginary unit). The gain of the filter, $G(\omega)$, is the absolute value of the complex filter transfer function. The filter is typically applied in the frequency domain. Thus, the time domain signal, $x(t)$, must be Fourier transformed to the frequency domain and then the filtered signal is inverse Fourier transformed back to the time domain. Equation 6.4 is valid for a continuous-time signal. With a z-transform (e.g. Grove (1991)) it can also be made valid for a discrete-time signal.

$$\begin{aligned} G(\omega) &= |H(i\omega)| \\ x_{filt}(t) &= \mathscr{F}^{-1}\{G(\omega)\mathscr{F}\{x(t)\}\} \end{aligned} \tag{6.4}$$

There are many linear time-invariant filters that can be used for filtering, e.g. Butterworth, Chebyshev, Bessel and Cauer. However, the Butterworth filter has shown to be a very good choice since it has a smooth passband and stopband, while the others have ripples (oscillations) in either the passband, stopband or both (Winder 2002).

The digital Butterworth filter is presented in Equation 6.5, where z is the discrete z-transform variable related to $s = \sigma + i\omega$ in the Laplace domain (e.g. Grove (1991)). Practically the Butterworth filter is implemented in MATLAB by the function *butter*. If the filter is lowpass or highpass, the order of the filter is n, while the order of the filter is $2n$ for a bandpass or bandstop filter (due to two cut-off frequencies). The two vectors of coefficients $\vec{a}$ and $\vec{b}$ are determined based on the cut-off frequency (or cut-off frequencies for bandpass or bandstop) and the order of the filter.

$$H(z) = \frac{b(1) + b(2)z^{-1} + ... + b(n+1)z^{-n}}{a(1) + a(2)z^{-1} + ... + a(n+1)z^{-n}} \tag{6.5}$$

The order of the filter determines how quick the decay (slope from passband to stopband or vice versa) of the filter becomes. A filter will always introduce a phase shift of the original signal, and a higher order of the filter will introduce a larger phase shift at increasingly higher frequencies. There exists techniques to overcome the problem that a phase shift is introduced in the time signal with a filter. This is referred to as zero-phase filtering and is only possible when post-processing data. In simple terms the zero-phase filtering applies the filter twice. First the original time signal is filtered (first filtering) and then it is reversed. The filtered reversed time signal is filtered (second filtering), and then the time signal is reversed back again. Thus, the phase shift normally introduced with the filter is cancelled. The order of the filter becomes double of what it is designed for if zero-phase filtering is not used since the filter is applied twice. Zero-phase filtering is implemented in MATLAB through the function *filtfilt*, which takes the Butterworth vectors of coefficients and the original discrete-time data series as input.

In general, low-pass filtering has been applied to all results from the experimental tests to remove high-frequent measurement noise. Band-pass filtering has also been used, but only for some select applications.

6.3 Model Calibration Tests

The results from the experimental decay tests have been used for calibration of the simulation model with regards to structural eigenfrequencies and global structural damping. The decay tests were performed in the experiment by placing the structure in the ocean basin and exciting it by hitting the structure at two different locations, corresponding to top of the tower ($z = 87.6\ m$) and a point between the top of the tower and the waterline ($z = 31.8\ m$). The reason for exciting the structure at different points was to excite different bending modes of the structure. Hitting at the top of the tower is expected to excite the first bending mode, while hitting the structure between the top of the tower and the waterline is expected to also excite the second and possibly third bending modes. In this way, the structural eigenfrequencies up to the third bending mode can be estimated.

The time series from the experimental tests have been analyzed in MATLAB and the method of logarithmic decrement, described in Section 3.4 was used to estimate the structural damping, in form of the damping ratio. The decay test for the hit at the top of the tower used for estimating the damping, as the response is concentrated at the first bending mode, i.e. at one frequency only. Hence, the method of logarithmic decrement can be used, as it assumes that the response is at a single frequency and a peak is always lower than the previous. This would not be the case for the decay test with hit between the top of the tower and the waterline, as multiple frequencies from different modes will interact.

The time series of the decay tests were transformed to the frequency domain, by application of the function *dat2spec* which is a feature of the WAFO toolbox (WAFO-group 2011) for MATLAB. The function divides the time series into blocks of equal size and estimates the autocorrelation function for each block before applying FFT to estimate the spectral density function for each block. Averaging is performed between the spectra for each blocks to obtain the spectral density function for the entire decay test. The spectrum for the decay test was used to obtain the eigenfrequencies for the different modes, which appear as peak frequencies in the spectrum. When estimating the eigenfrequencies, the decay tests with hit at both locations are used.

Having analyzed the experimental tests, the simulation model in SIMA had to be tuned to have the same properties as the experimental model. The structural damping in SIMA is implemented as global Rayleigh damping for the entire structure. Only stiffness proportional damping has been used following from the discussion in Section 3.2. The simulation model was tuned with respect to eigenfrequencies, with focus on getting the first mode eigenfrequency correct, by altering the stiffness of the mudpile, i.e. cross-sectional bending stiffness properties of *soilSpring* in Table 3.3. One could arguably have tuned the mass of the drag disks, but there is a larger uncertainty connected to the stiffness of the mudpile due to the way the monopile was fixed to the ocean basin bottom in the experimental test setup, than the mass of the drag disks.

The decay test does not directly give any information about the modal shapes of the structure. For this purpose an eigenvalue analysis is much more convenient. Hence, an eigenvalue analysis is conducted in SIMA, for which the modal shapes of the three first bending modes and the corresponding eigenfrequency for each mode is determined. The eigenvalue analysis is, in addition to obtaining the modal shapes of the structure, useful to confirm the eigenfrequencies estimated from the decay tests. Thus, the eigenvalue analysis supports the decay tests in validating the structural properties of the monopile.

6.4 Regular Waves

The regular waves in this work were calibrated with two nominal wave steepnesses, $\frac{H}{\lambda} = \frac{1}{30}$ and $\frac{H}{\lambda} = \frac{1}{40}$, and for periods between 6 and 15 seconds with 1 second intervals. The wave steepnesses are not strictly the specified ratio for all tests, but the nominal value will be used for reference. The list of calibrated regular waves is given in Table 6.2. Due to wavemaker limitations the largest period for steepness $\frac{H}{\lambda} = \frac{1}{30}$ is 14 seconds. As wave reflection in the ocean basin becomes an issue, there is only a small time interval of the signal that can be used, i.e. after transient effects are finished and before wave reflection begins. This time interval is also specified in Table 6.2. The time interval corresponds to the five last periods before wave reflection in the ocean basin was experienced (only last two periods for $T \geq 13\ s$).

Table 6.2: Overview of calibrated regular waves with wave height, H [m], wave period, T [s], and start and end times of signal, t_1 [s] and t_2 [s]

Steepness $\frac{H}{\lambda} = \frac{1}{30}$					**Steepness $\frac{H}{\lambda} = \frac{1}{40}$**				
Wave no.	H	T	t_1	t_2	*Wave no.*	H	T	t_1	t_2
80100	1.9	6	470.42	500.40	81000	1.4	6	470.42	500.40
80200	2.6	7	390.19	425.20	81100	1.9	7	390.19	425.20
80303	3.3	8	328.31	368.31	81201	2.5	8	328.31	368.31
80401	4.2	9	278.60	323.60	81301	3.2	9	278.60	323.60
80501	5.2	10	237.46	287.45	81401	3.9	10	237.46	287.45
80601	6.3	11	210.01	265.03	81501	4.7	11	210.01	265.03
80701	7.5	12	210.01	270.03	81601	5.6	12	210.01	270.03
80800	8.8	13	210.01	236.00	81701	6.6	13	210.01	236.00
80901	10.2	14	210.01	238.02	81800	7.7	14	210.01	238.02
					81902	8.8	15	210.01	240.02

The calibrated regular wave test were run without the structure in the ocean basin. After calibration, the structure was installed and the calibrated waves were run again to obtain the structural response. The test numbers and their corresponding wave numbers are listed in Table 6.3, as well as the added mass and drag coefficients for each test. The added mass and drag coefficients have been calculated based on the wave height and wave period for the calibrated wave for each test according to the approach described in Section 4.5. The value of the drag coefficient for smooth cylinders before wake amplification effects are taken into account is taken it taken as $C_{DS} = 0.65$. The drag and added mass coefficients are then a function of the K_C number. The K_C for each test is therefore also listed in Table 6.3.

Table 6.3: Overview of the test numbers and their corresponding calibrated wave numbers for the regular wave tests, as well as K_C number, added mass and drag coefficients for each test

Steepness $\frac{H}{\lambda} = \frac{1}{30}$					**Steepness $\frac{H}{\lambda} = \frac{1}{40}$**				
Test no.	*Wave no.*	K_C	C_A	C_D	*Test no.*	*Wave no.*	K_C	C_A	C_D
20010	80100	0.85	1.00	0.19	21010	81000	0.63	1.00	0.35
20020	80200	1.18	1.00	0.19	21020	81100	0.86	1.00	0.19
20030	80303	1.54	1.00	0.19	21030	81201	1.17	1.00	0.19
20040	80401	2.04	1.00	0.20	21040	81301	1.55	1.00	0.19
20050	80501	2.65	1.00	0.24	21050	81401	1.99	1.00	0.19
20060	80601	3.39	0.98	0.28	21060	81501	2.53	1.00	0.23
20070	80701	4.27	0.94	0.34	21070	81601	3.19	1.00	0.27
20072	80701	4.27	0.94	0.34	21080	81701	3.98	1.00	0.32
20080	80800	5.31	0.90	0.41	21090	81800	4.91	1.00	0.38
20090	80901	6.5	0.85	0.49	21091	81800	4.91	1.00	0.38
20091	80901	6.5	0.85	0.49	21100	81902	5.92	1.00	0.45

The regular wave tests are simulated in SIMA with the same surface elevation time series as measured from the calibrated waves in the experimental tests. This procedure is described in Section 6.6. Additionally the regular wave tests generated by SIMA, based on the input of the surface elevation time series, are simulated with linear wave kinematics with integration up to the mean surface level.

The regular tests are used to obtain the RAO for each steepness by using the mudline and waterline moment as the response. The RAOs have been established for first, second and third order, corresponding to n times the wave frequency, where n is the order. The response is bandpass filtered around the frequency of the order in question by the frequency band $[0.9\omega_n\ , 1.1\omega_n]$, and the response amplitude is compared to the first order wave amplitude to obtain the RAO, as described in Equation 5.20. However, when considering an actual regular wave, generated in an ocean basin, the wave amplitude will not be perfectly equal to the nominal value for each cycle and so it follows that the response will not have perfectly equal amplitude for each cycle. There are many ways to determine the amplitude of both the wave and response within the indicated time interval for the regular wave test.

Steen (2014) suggests that the average value of the peaks and average value of the minimum peak and maximum peak are less accurate estimates of the amplitude, and that the amplitude should be calculated as the standard deviation of the signal multiplied with the square root of two.

$$RAO(\omega) = \frac{y_0}{x_0} = \frac{\sqrt{2}\sigma_y}{\sqrt{2}\sigma_x} = \frac{\sigma_y}{\sigma_x} \tag{6.6}$$

where y_0 and σ_y denote the response amplitude and standard deviation of the response time series respectively and x_0 and σ_x denote the wave amplitude and standard deviation of the surface elevation time series respectively.

6.5 Irregular Waves

As mentioned in Section 5.2, the irregular waves were generated by the TMA spectrum. The data for input to the TMA spectrum was based on data from cite no. 15 *North Sea Centre* in Li et al. (2015), somewhat adjusted to take the capacity of the wavemaker into consideration and to avoid breaking wave events. The sea states (combination of H_s and T_p) studied in this work are located on or close to the 50-year contour line, i.e. sea states with 50-year return period on the specific location. The 50-year contour line and the selected conditions are shown in Figure 6.2.

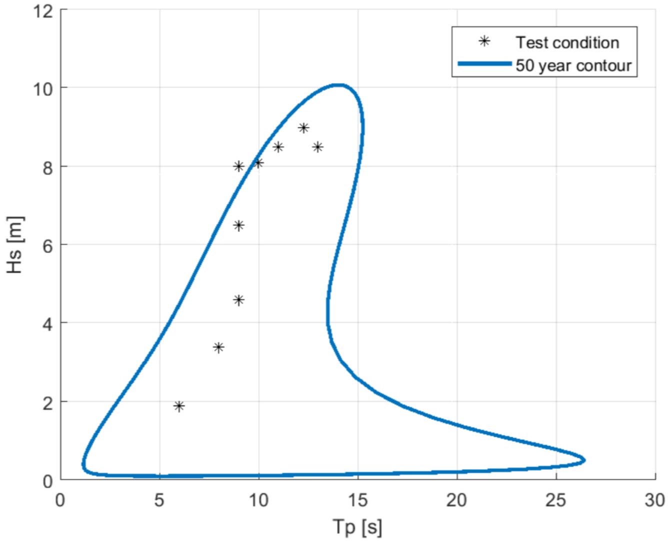

Figure 6.2: 50-year contour line and selected sea states (the four smallest sea states are not considered in this work). Taken from Thys (2017).

The list of calibrated irregular waves is given in Table 6.4 with their respective significant wave height and peak period. As for the regular waves, the calibrated irregular waves were run without the structure in the ocean basin. After calibration, the structure was installed and the calibrated waves were run again to obtain the structural response. The test numbers and their corresponding wave numbers are listed in Table 6.5, as well as the added mass and drag coefficients for each test. The added mass and drag coefficients have been calculated based on the significant wave height and peak period for the calibrated wave for each test according to the approach described in Section 4.5. As for the regular wave tests, the value of the drag coefficient for smooth cylinders before wake amplification effects are taken into account is taken it taken as $C_{DS} = 0.65$. The drag and added mass coefficients are then a function of the K_C number. The K_C for each test is therefore also listed in Table 6.5.

The irregular waves have a start-up period of 19 minutes and the effective duration of the irregular tests correspond to a sea state duration of 3 hours (full scale), in accordance with the previous discussion about sea states in Section 5.2.

Table 6.4: Overview of calibrated irregular waves with significant wave height, H_s [m] and peak period, T_p [s]

Wave no.	H_s	T_p	Comment
84502	8.0	9.0	
84601	8.1	10.0	
84701	8.5	10.9	
84803	9.0	12.3	Base case
84810	9.0	12.3	Seed variation
84811	9.0	12.3	Seed variation
84812	9.0	12.3	Seed variation
85101	8.5	13.0	

Table 6.5: Overview of the test numbers and their corresponding calibrated wave numbers for the irregular wave tests, as well as K_C number, added mass and drag coefficients for each test

Test no.	35010	36010	37010	38010	38020	38030	38040	38110
Wave no.	84502	84601	84701	84803	84810	84811	84812	84803
K_C	3.89	4.13	4.58	5.22	5.22	5.22	5.22	5.22
C_A	0.96	0.95	0.93	0.90	0.90	0.90	0.90	0.90
C_D	0.32	0.33	0.36	0.40	0.40	0.40	0.40	0.40

Test no.	38120	38130	38140	38150	38160	38170	38180	39010
Wave no.	84803	84803	84803	84803	84803	84803	84803	85101
K_C	5.22	5.22	5.22	5.22	5.22	5.22	5.22	5.13
C_A	0.90	0.90	0.90	0.90	0.90	0.90	0.90	0.91
C_D	0.40	0.40	0.40	0.40	0.40	0.40	0.40	0.40

From Table 6.4 it is seen that there are four wave numbers with the same sea state parameters, i.e. $H_s = 9.0\ m$ and $T_p = 12.3\ s$. These are different realizations of the same sea state. When irregular sea is generated from a wave spectrum, as described in Section 5.2, it is often desirable to generate multiple time realizations of the same sea state to cover the stochastic diversity of a process and use the data as a basis for e.g. extreme value statistics. The term seed refers to the initialization of a sequence of random numbers generated by a pseudo-random number generator. When a realization of an irregular sea is generated, e.g. according to Equation 5.12, the random phase angles, ϵ_j, will be generated the same every time if the seed is the same value. Making a variation in the seed will create a different set of random phase angles, which will ensure that the time realization of the irregular sea is different, even though the significant wave height and peak period are unchanged.

As for the regular wave tests, the irregular wave tests are simulated in SIMA with the same surface elevation time series measured from the calibrated waves in the experimental tests. This is described in Section 6.6. Additionally the irregular wave tests are simulated with four different types of wave kinematics, all described in Chapter 4. These methods are linear wave kinematics with integration of forces to mean surface level, linear wave kinematics with simple extrapolation above the mean surface level, linear wave kinematics with Wheeler stretching and second order wave kinematics with integration of forces to wave surface. The different types of wave kinematics are generated by SIMA with only the surface elevation time series as input.

For the post-processing of the irregular wave tests, different aspects have been studied.

The experimental test time series of the wave elevation were studied to identify large and steep wave events that could lead to ringing responses. The moment time series were studied accordingly to identify ringing responses. The waterline moment time series were studied in particular as it was found that the response was mostly concentrated at the first bending mode, making it easier to identify ringing responses. Next, the simulated time series were considered, looking for ringing responses at the time instances where ringing was found in the experimental time series. As the structural response has been simulated with different types of wave kinematics, it was interesting to study how well, if at all, any of the wave theories could describe ringing responses.

The overall ability of the load models to describe the response of the structure was also investigated. This was done by studying the response spectra of the simulations with the different types of wave kinematics, and comparing them with the experimental response spectra. In this way it is possible to determine how well the simulated response represents the experimental response at different frequencies.

The damping in the system was determined through the decay tests, described in Section 6.3. However, there was some concern about how well the damping was estimated through the decay tests, and if the damping estimated through the decay tests was representative of the damping when the structure was subjected to waves. As the system damping governs the response around the natural frequency, it is an important parameter to study. A parameter study was therefore conducted on the system damping. Four different damping ratios were considered. These are listed in Table 6.6, as well as the corresponding stiffness-proportional damping coefficient for the Rayleigh damping formulation. Suja-Thauvin et al. (2017) have done experimental tests on a monopile structure of similar geometry and for similar water depth as the one in this work. They found that the damping ratio for the first mode was 1.1%. This was used as a basis for a realistic damping ratio when determining the range of damping ratios for the parameter study. Suja-Thauvin et al. (2017) have also made a summary of the damping for similar full scale monopile wind turbines which is found in the literature. These damping ratios are in the range $1.7 - 2.8\%$ depending on the wind speed for idling cases. This range could also have been used as a basis for determining the damping ratios for the parameter study. However, the effect of changing the damping will be shown to be well described by the chosen parameters.

Table 6.6: First mode damping ratios (λ_1 [%]) and stiffness-proportional damping coefficients (α_1) for the parameter study

λ_1	α_1
0.47	0.0065
0.68	0.0095
0.89	0.0125
1.10	0.0155

From Table 6.5 it is seen that there are nine experimental tests that have been run with the same wave (Wave no. 84803). These are repetition tests, conducted to investigate the random error of the experiments. The random error is considered by the coefficient of variation which is defined as the ratio between the standard deviation and mean value of a process. The coefficient of variation for a sample, x, of size N is given by

$$C_v = \frac{s_x}{\bar{x}} \tag{6.7}$$

where $\bar{x}$ and s_x are mean value and the standard deviation of the sample respectively, given by

$$\begin{aligned} \bar{x} &= \frac{1}{N}\sum_{i=1}^{N} x_i \\ s_x &= \sqrt{\frac{1}{N-1}\sum_{i=1}^{N}(x_i - \bar{x})^2} \end{aligned} \tag{6.8}$$

The coefficient of variation is applied to the maximum moment (absolute value), as well as the maximum wave height at the two wave probes on the same line as the structure in the repeated tests. An overview of the wave probes used in the experiments is shown in Figure 6.3. The two wave probes considered for the repeatability analysis are numbered 7 and 15. The structure is installed at coordinate $(0, 0)$, which is referred to as *blink*. When the calibrated wave tests are run and the structure is not installed in the ocean basin, there is an extra wave probe installed at blink. This wave probe is numbered 2, and is the wave probe where the measured surface elevation data for the calibrated waves has been taken from in this work.

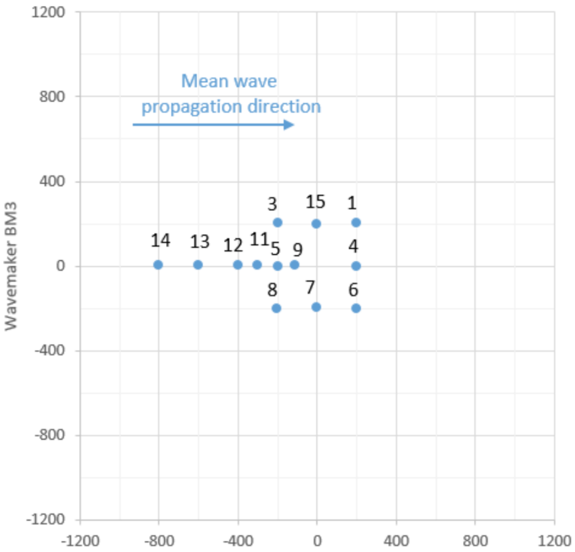

Figure 6.3: Set-up of wave probes for regular and irregular wave tests, when the structure is installed at blink (coordinate $(0, 0)$). Taken from Thys (2017).

6.6 Wave Generation for Simulations

SIMA has the possibility of generating waves based on input for surface elevation from text file. The file has to have time instances in the first column and the surface elevation in the second column. The file length (number of rows) has to be a numerically efficient number, i.e. 2^n, $n = 1, 2, 3, \ldots$. This option is useful since the measured waves from the experiments can be used to run analyses also for the simulations, so that the response can be compared based on the same input conditions.

For each distinct wave number from the regular wave tests (Table 6.2) and irregular wave tests (Table 6.4), the calibrated wave from the experiments was imported into MATLAB. The surface elevation was sampled with a time step of 0.1 seconds (sampling frequency $10\ Hz$) from the experimental test surface elevation, which was measured with a considerably higher sampling frequency of $31.62\ Hz$ ($200\ Hz$ in model scale), corresponding to a time step of 0.0316 seconds. As the time instances for the sampled surface elevation does not coincide with the time instances of the experimental test surface elevation, linear interpolation was used to obtain the surface elevation at the sampled time instances. An example of how the time series of the sampled surface elevation time series for SIMA looks compared to the original time series from the experiment is presented in Figure 6.4 for a regular wave test.

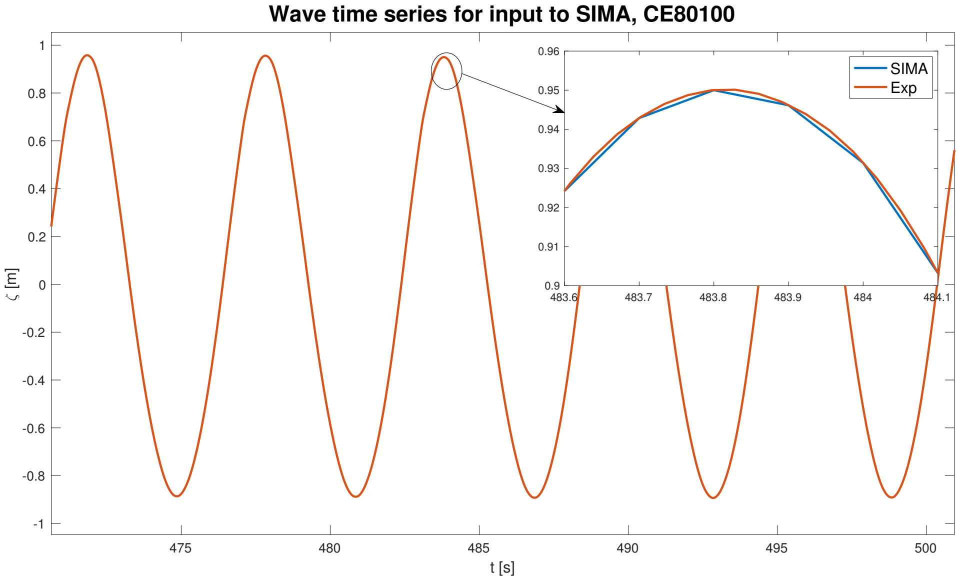

Figure 6.4: Sampled surface elevation for SIMA based on measurements from experiments, exemplified for a regular wave

For the regular waves, a specified time interval for which the wave is considered regular due to wave reflection issues has been specified in Table 6.2. The file length for the sampled regular surface elevation is taken as the end time of that interval, t_2, multiplied by the sampling frequency of 10 Hz and rounded up to the nearest number in $2^n,\ n = 1, 2, 3, ...$. The file lengths, i.e. number of rows in the files, for the sampled regular waves time series are listed in Table 6.7 along with the corresponding end times for the time series. The time interval between t_1 and t_2 where the regular wave tests are valid is enforced in the post-processing of the response.

Table 6.7: Overview of the file length and time series end time [s] for the sampled waves elevation time series for regular waves to be implemented in SIMA

Steepness $\frac{H}{\lambda} = \frac{1}{30}$			**Steepness $\frac{H}{\lambda} = \frac{1}{40}$**		
Wave no.	*File length*	*End time*	*Wave no.*	*File length*	*End time*
80100	8192	819.1	81000	8192	819.1
80200	8192	819.1	81100	8192	819.1
80303	4096	409.5	81201	4096	409.5
80401	4096	409.5	81301	4096	409.5
80501	4096	409.5	81401	4096	409.5
80601	4096	409.5	81501	4096	409.5
80701	4096	409.5	81601	4096	409.5
80800	4096	409.5	81701	4096	409.5
80901	4096	409.5	81800	4096	409.5
			81902	4096	409.5

For the irregular waves, the file length was determined based on the end time for the measured time series from the experiments. The irregular waves were run so that the effective length of the time series became approximately 3 hours and 19 minutes in the experiments, as suggested in Section 6.5. Thus the file size for the irregular waves should be 11940 seconds multiplied with the sampling frequency of 10 Hz and rounded up to the nearest number in $2^n,\ n = 1, 2, 3, ...$ Following from this, the file length for the irregular waves was determined to be 2^{17}, i.e. 131072 number of rows in the file corresponding to a time series length of 13107.1 seconds. Since the surface elevation time series from the experiments is shorter than what is required for the time series for input to SIMA, the surface elevation for the time instances exceeding the end time of the experimental wave time series was set to zero. Adding zeros to the end of the file was not necessary for the regular waves, since the experimental surface elevation time series was always longer than what was required for the sampled surface elevation time series.

SIMA interprets the surface elevation time series input as a linear surface elevation. For the irregular wave tests it is expected that nonlinearities occur in the ocean basin when waves interact. Hence, it is expected that there will be energy for the nonlinear at sum-frequencies, i.e. in the right tail of the wave spectrum. In order to not have SIMA overestimate the energy in the sea state, it is therefore convenient to filter out the high-frequencies expected to be related to nonlinearities. Stansberg et al. (2008) proposes a cut-off frequency for which the surface elevation should be low-pass filtered.

$$\omega_{c,high} = \sqrt{\frac{2g}{H_s}} \tag{6.9}$$

Similarly to the nonlinear sum-frequency effects, it was seen that nonlinear difference-frequency effects were experienced. Thus, it is desirable to filter out these low frequencies as well. No guidelines as to which cut-off frequency should be implemented for low-frequencies were found. A cut-off frequency was chosen as $\omega_{c,low} = 0.4\ rad/s$ after visually investigating the measured spectra. As both low and high frequencies should be filtered out, a bandpass filter was implemented with the two mentioned cut-off frequencies, before the measured surface elevation from the experiments was sampled. It was realized too late that there would be problems connected to not filtering out the difference frequencies when SIMA was generating waves. Thus, the bandpass filter is only implemented for the irregular wave simulations with second order wave kinematics. For the other three methods for generating wave kinematics, only a lowpass filter with the cut-off frequency in Equation 6.9 was implemented. The consequences of this is discussed when evaluating the results.

An issue arose in SIMA related to memory when generating second order irregular waves. Thus, only half the time series could be run at the time, i.e. for $6553.5\ s$. Due to time limitations for both simulating and post-processing the data, only the first $6553.5\ s$ of the time series was simulated. This is also discussed further when evaluating the results.

Chapter 7

Results and Discussion

The results presented in this chapter are selected results to illustrate different aspects of the structural response. As validation is important in this thesis, additional figures for regular wave tests and irregular wave tests are provided in the appendices to support the findings presented in the main part of the thesis. The results are generated based on the experimental test and simulation procedure described in Chapter 6. The results are commented and discussed as they are presented.

7.1 Calibration of Simulation Model

In order to calibrate the simulation model the decay test data from the experiments were used. Figure 7.1 shows the waterline moment spectrum of the decay test when the structure was excited by a hit at the middle of the tower. The peaks in the spectrum represents the eigenfrequencies of the three first bending modes of the structure. It is seen that most of the energy is concentrated around the first bending mode, as expected. Some energy is evident at the second bending mode, while there is only a small amount of energy evident at the third bending mode.

The corresponding decay test is simulated in SIMA, and the waterline spectrum of the simulation is shown in Figure 7.2. It is seen that the simulated decay test only estimates the first two bending modes. The simulation model was only tuned to have the first bending mode eigenfrequency equal to the experimental model, which was found to be $\omega_1 = 1.42\ rad/s$. As a result, there is some error connected to the second and third mode eigenfrequencies.

A summary of the eigenfrequencies for the three first bending modes of the structure estimated from the experimental decay tests and the simulations in SIMA is given in Table 7.1, after the results of the eigenvalue analysis are considered.

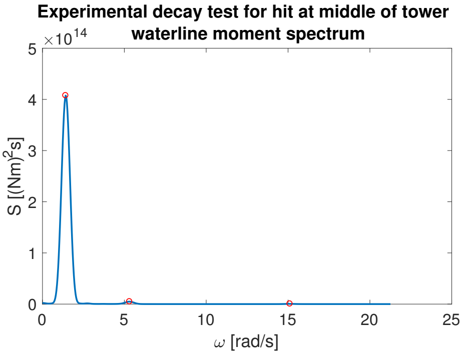

Figure 7.1: Waterline moment spectrum for experimental decay tests, where the structure was excited by a hit around the middle of the tower

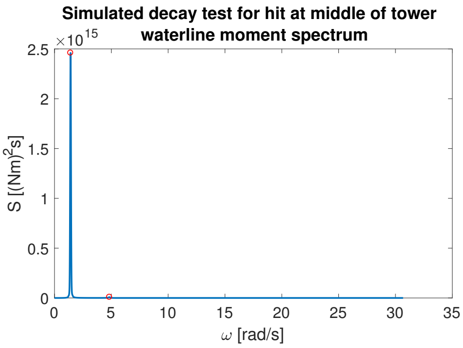

Figure 7.2: Waterline moment spectrum for simulated decay tests, where the structure was excited by a hit around the middle of the tower

Figure 7.3 shows the waterline moment decay test in the time domain for both the experimental test and the simulated test. These time series were used to estimate the moment spectra above. Up to around 60 seconds it is seen that there are multiple frequencies of oscillations that interact. Afterwards the decay stabilizes at one frequency, presumably the eigenfrequency of the first bending mode. As there are multiple frequencies interacting, the method of logarithmic decrement was not applied to the decay tests where the structure was excited by a hit at the middle of the tower.

Figure 7.4 shows the waterline moment times series of the decay test when the structure was excited by a hit at the top of the tower. Compared to the decay in Figure 7.3, it is seen that there are not multiple frequencies interacting. The response is concentrated at the eigenfrequency of the first bending mode. For this case, the method of logarithmic decrement was applied and the structural damping was estimated, in form of the damping ratio. The damping ratio for the first mode was found to be $\lambda_1 = 0.47\%$. This corresponds to a stiffness-proportional damping coefficient of $\alpha_2 = 0.0065$ for the Rayleigh structural damping formulation. It is observed that the overall behaviour of the first mode structural response with respect to both damping and eigenfrequency is very well represented by the SIMA simulation relative to the experimental test.

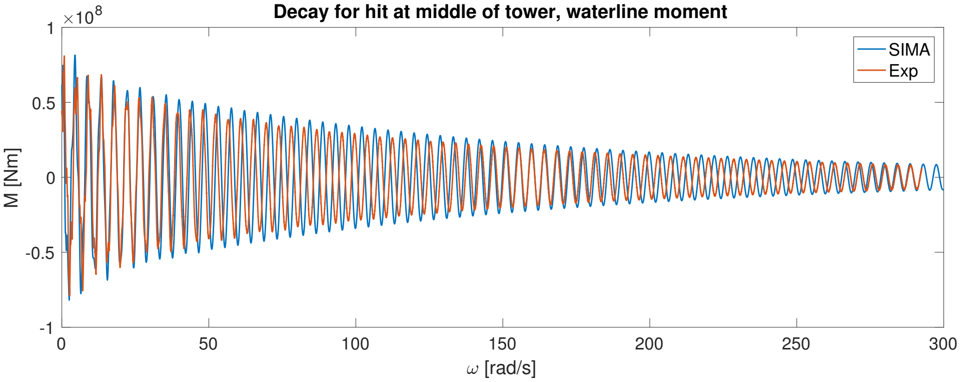

Figure 7.3: Comparison between experimental and simulated waterline moment decay time series, where the structure was excited by a hit around the middle of the tower

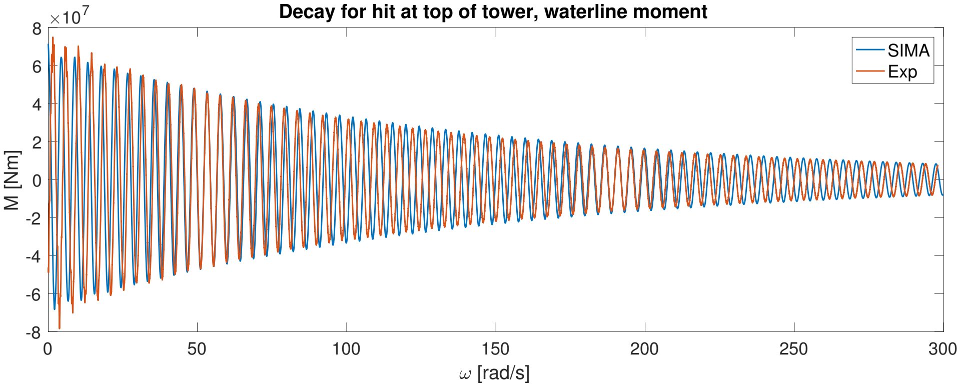

Figure 7.4: Comparison between experimental and simulated waterline moment decay time series, where the structure was excited by a hit at the top of the tower

An eigenvalue analysis was also performed in SIMA to support the validation of the simulation model. The results of the eigenvalue analysis are shown in Figure 7.5. The figure shows the first three modal shapes in bending and the corresponding modal eigenfrequencies. It is noticed that the eigenvalue test confirms the first mode eigenfrequency estimated from the decay tests. From the modal shapes it is evident that exciting the structure at the top of the tower ($z = 87.6\ m$) excites the first bending mode, while the second and third bending modes are only excited to a relatively small extent. If the structure is excited at the middle of the tower ($z = 31.8\ m$) all three bending modes will be excited to some extent. This is in accordance with what was discussed for the decay time series and spectra.

In Section 3.5 the structure was simplified as a cantilever beam when considering modal shapes. It is seen that the sketches of the three first modal shapes in Figure 3.1 are good representations of the actual modal shapes calculated from the eigenvalue analysis.

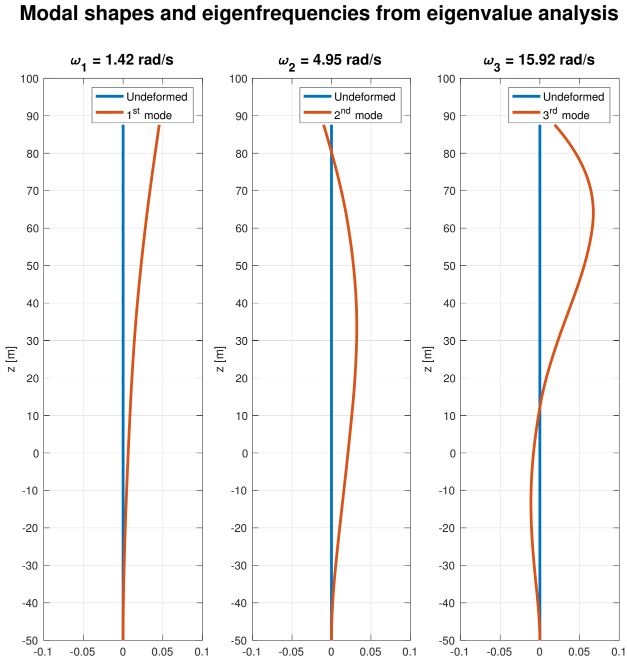

Figure 7.5: Modal shapes and corresponding eigenfrequencies for the first three bending modes from the eigenvalue analysis

Table 7.1 shows a summary of the eigenfrequencies, and corresponding eigenperiods, for the three first bending modes estimated from the experimental decay tests, simulated decay tests and the eigenvalue analysis.

Table 7.1: Eigenfrequencies for the three first modes ω_n [rad/s], with error in percent relative to experimental decay test, and corresponding eigenperiod T_n [s]

	ω_1	T_1	ω_2	T_2	ω_3	T_3
Experiment	1.42	4.42	5.32	1.18	15.11	0.42
Simulation	1.42 (0%)	4.42	4.86 (-8.6%)	1.29	-	-
Eigenvalue	1.42 (0%)	4.42	4.95 (-7.0%)	1.27	15.92 (+5.4%)	0.39

Even though there is some error connected to the second and third mode eigenfrequencies, the simulation model is considered calibrated based on the results in this section, as the overall structural behaviour of the simulation model is satisfactory compared to the experimental model with the available data.

7.2 Regular Wave Results

The main purpose of the regular wave tests for this work was to establish the RAOs for the first, second and third order of the response compared to the first order wave elevation. The results for the mudline moment RAOs are shown in the figures below. Figure 7.6 and Figure 7.7 show the first-order RAO for wave steepness $\frac{H}{\lambda} = \frac{1}{30}$ and $\frac{H}{\lambda} = \frac{1}{40}$ respectively. From Section 7.1 it was shown that the first mode eigenperiod was $T_1 = 4.42\ s$. Therefore it seems reasonable that the first-order RAO has a higher value for periods close to this, while it slowly decays for higher periods. The behaviour of the system is very similar for both wave steepnesses, as expected. It is also observed that the simulated RAO and the experimental RAO are close in value for all frequencies considered in this work, indicating that Morison's equation with linear theory kinematics estimates the first order loads well.

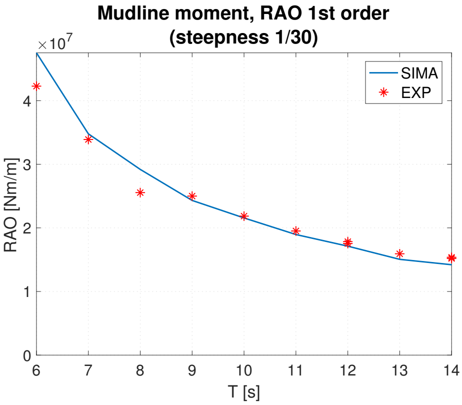

Figure 7.6: 1^{st} order RAO for mudline moment from regular waves (steepness 1/30)

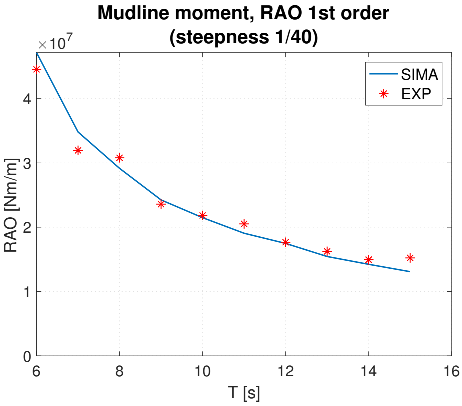

Figure 7.7: 1^{st} order RAO for mudline moment from regular waves (steepness 1/40)

The second-order RAOs are shown in Figure 7.8 and Figure 7.9. It is seen that the simulated response is a very good estimation of the response obtained from the experimental tests, except for the tests with wave period $T = 9\ s$. The simulated response is greatly overestimated at this period. It is noticed that this period correspond to two times the natural frequency of the first mode. For the simulations in this work, the Morison model takes diffraction effects into account through the MacCamy-Fuchs correction. However, only linear diffraction effects are taken into account. It is expected that second order diffraction effects must be taken into account in order to properly estimate the response at this period through simulations.

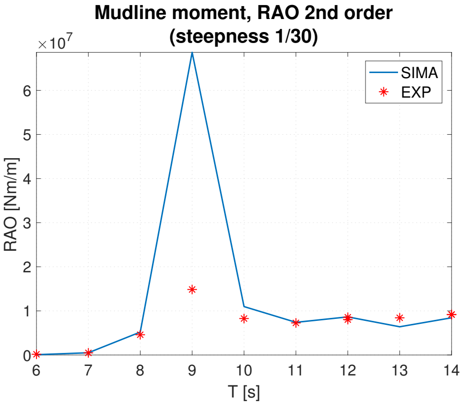

Figure 7.8: 2^{nd} order RAO for mudline moment from regular waves (steepness 1/30)

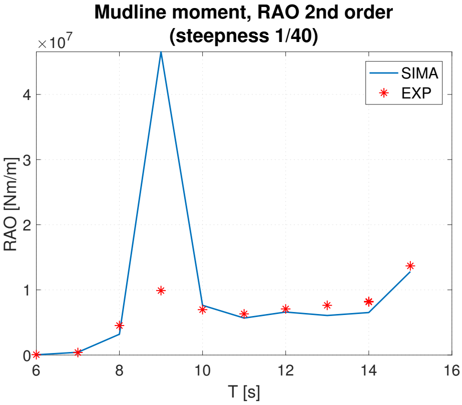

Figure 7.9: 2^{nd} order RAO for mudline moment from regular waves (steepness 1/40)

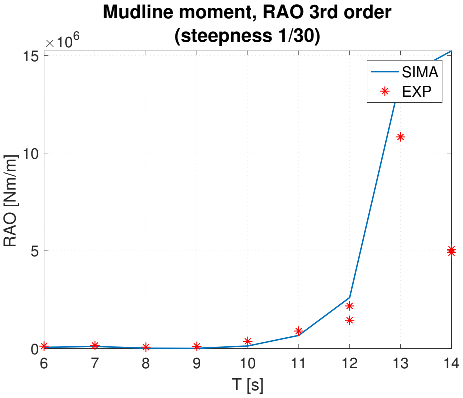

Figure 7.10: 3^{rd} order RAO for mudline moment from regular waves (steepness 1/30)

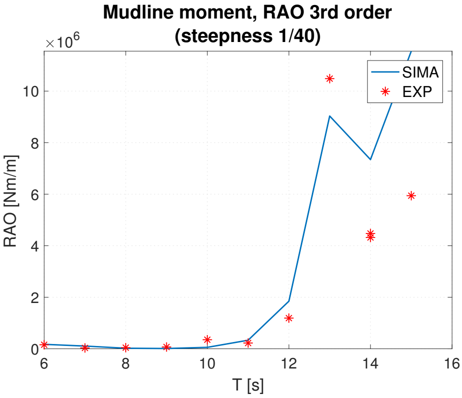

Figure 7.11: 3^{rd} order RAO for mudline moment from regular waves (steepness 1/40)

Figure 7.10 and Figure 7.11 show the RAOs for third order. Overall it is seen that the third-order response is one order of magnitude lower than both first-order and second-order responses. From the figures it seems as though the response is well estimated for low periods, and that the error increases for higher periods. However, a close examinations of the response at the periods $T \leq 10$ revealed that the relative error is comparable to the rest of the data. The response at these periods is two orders of magnitude lower than first and second order response. Thus, it becomes very difficult to discuss the results according to theory since the magnitude of the response makes it very vulnerable with respect to measurement accuracy. Nonetheless, a large overestimation is seen at three times the natural frequency. Following from the reasoning used for the second-order response, this could be connected to diffraction effects.

As mentioned, only the RAOs for the mudline moment has been presented here. For validation purposes the waterline moment results are given in Appendix A. The results of the waterline moment follow the discussion made for the mudline moment.

A comparison of the simulated and experimental test mudline moment time series for three selected regular wave tests are shown below to complement the RAO results. Figure 7.12 shows how the simulated response is clearly overestimated for the regular wave with period $T = 9\ s$, as indicated by the second-order RAOs. In Figure 7.13 it is seen that the first-order response is clearly estimated well. However, the third-order response is overestimated by the simulations, as indicated by the third-order RAOs for $T = 14\ s$. Figure 7.14 illustrates that the response is well estimated for first and second order for $T = 11\ s$. As mentioned earlier, it is difficult to say if the third-order response is estimated well as the magnitude of the third-order response is much smaller relative to the response for first and second order.

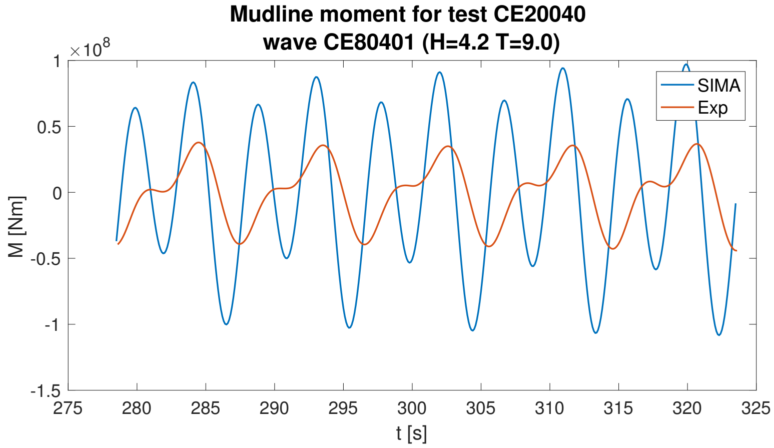

Figure 7.12: Mudline moment for test CE20040 (wave steepness 1/30), showing overestimation of simulated response

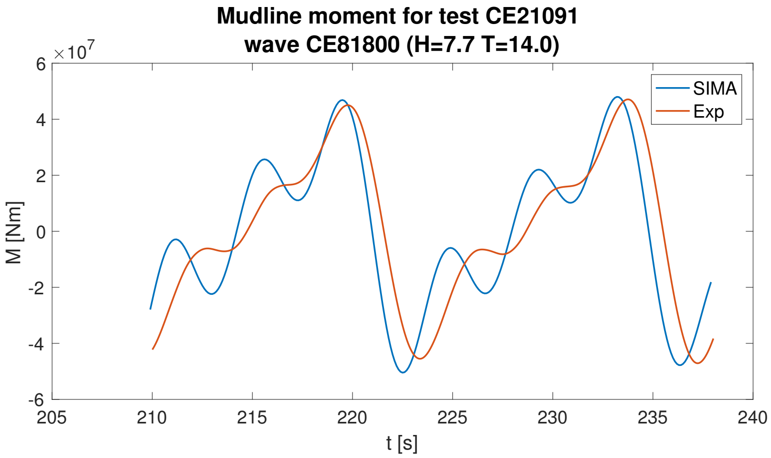

Figure 7.13: Mudline moment for test CE21091 (wave steepness 1/30), showing overestimation of simulated response at third order

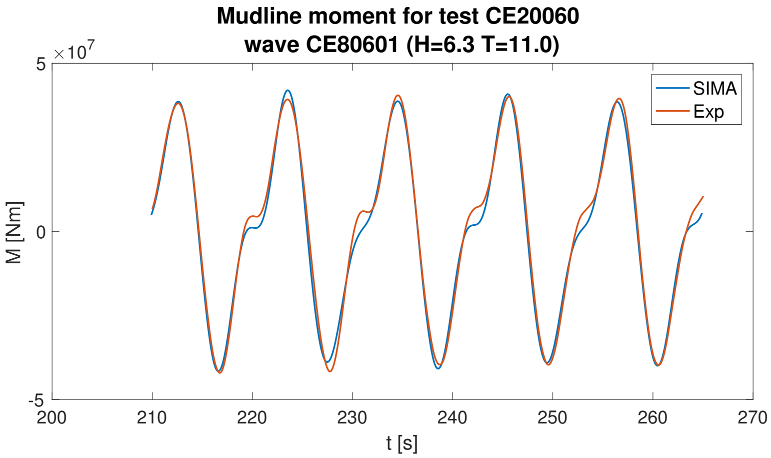

Figure 7.14: Mudline moment for test CE21091 (wave steepness 1/30), showing a well estimated simulated response

7.3 Irregular Wave Results

7.3.1 Repeatability Analysis

The repeatability analysis has been done to consider the uncertainties in the experiments. Test number 38010 is referred to as the base case and the other tests are referred to as repetition cases.

Table 7.2 shows the global maximum for each time series and its time of occurrence for both the mudline moment and waterline moment. The local maxima for the repetition tests are also found around the time where the global maximum of the base case occurs. The local maxima are found in a 50 second interval, defined within 25 seconds on either side of the global maxima times of occurrence. It is seen that there is some variation in both the maxima values and times of occurrence. It is especially noted that the base case values differ significantly from the repetition cases values at the base case global maximum time of occurrence. The mudline maxima are intuitively larger than the waterline maxima as there are no external loads acting above the mean surface level.

Table 7.2: Overview of the global maxima [Nm], time of occurrence of global maxima [s] and local maxima [Nm] (at time of base case global maxima) for the mudline and waterline moment in the repeated tests

	Mudline			**Waterline**		
Test no.	*Global max*	*Time*	*Local max*	*Global max*	*Time*	*Local max*
38010	1.959×10^8	2693.3	1.959×10^8	9.626×10^7	2693.3	9.626×10^7
38110	1.854×10^8	9038.7	1.727×10^8	8.371×10^7	518.6	7.842×10^7
38120	1.849×10^8	9097.8	1.307×10^8	8.810×10^7	10582.1	5.209×10^7
38130	1.866×10^8	7629.5	1.460×10^8	8.622×10^7	552.0	5.652×10^7
38140	1.863×10^8	7853.3	1.500×10^8	9.982×10^7	7861.8	6.289×10^7
38150	1.827×10^8	9368.5	1.255×10^8	8.849×10^7	4638.9	4.761×10^7
38160	1.829×10^8	9369.0	1.651×10^8	8.494×10^7	4639.4	7.414×10^7
38170	1.916×10^8	7853.0	1.673×10^8	9.449×10^7	6412.4	7.518×10^7
38180	1.874×10^8	9041.9	1.619×10^8	8.901×10^7	4639.0	7.083×10^7

As for the mudline and waterline moment, the global maxima and time of occurrence, as well as the local maxima, are found for the surface elevation at wave probe 7 and wave probe 15. These results are given in Table 7.3. Again it is seen that the time of occurrence of the surface elevation global maxima vary. However, the maxima values, both global and local, do not seem to vary as significantly as for the moment results. Since the wave probes are placed on the same line as the structure and with equal distance from the structure when facing the long-crested waves, it would ideally be expected to see the same results at the two wave probes since the structure is axisymmetric. However, some disturbances due to e.g. wave reflection must be expected.

Table 7.3: Overview of the global maxima [m], time of occurrence of global maxima [s] and local maxima [m] (at time of base case global maxima) for the surface elevation measured at wave probe 7 and wave probe 15 in the repeated tests

	Wave probe 7			**Wave probe 15**		
Test no.	*Global max*	*Time*	*Local max*	*Global max*	*Time*	*Local max*
38010	10.2	9433.1	10.2	9.2	3309.4	9.2
38110	11.0	3309.2	9.3	9.3	1830.5	8.2
38120	9.4	3309.2	9.2	11.0	2830.2	8.2
38130	10.3	3309.8	9.9	9.7	1693.0	8.2
38140	10.6	3309.4	9.5	9.3	9611.1	8.9
38150	11.8	3309.0	9.0	10.4	9610.9	9.2
38160	9.9	3309.6	7.9	10.4	7627.1	9.2
38170	10.6	7626.4	8.5	11.0	7626.9	8.3
38180	10.0	7626.5	8.3	10.4	7627.0	9.1

Based on the data in Table 7.2 and Table 7.3 the coefficient of variation has been found for mudline and waterline moment, and surface elevation from wave probe 7 and wave probe 15, for both global and local maxima. These results are presented in Table 7.4. The difference in coefficient of variation for global and local maxima for both the mudline moment and waterline moment is seen to be quite large. This suggests that the uncertainty with respect to repeating the overall response maxima of the time series is low, while the uncertainties related to single event maxima is quite high. For the surface elevation measured at the wave probes, it is seen that the coefficient of variation is not very high, both for the global and local maxima, suggesting that large wave events are repeated reasonably well both for the time series as a whole and for single events.

Table 7.4: Coefficient of variation in percent for the maximum mudline and waterline moment, as well as the maximum surface elevation at wave probe 7 and wave probe 15 in the repeated tests for both global and local maxima

	Mudline	**Waterline**	**Wave probe 7**	**Wave probe 15**
Global	2.3%	6.1%	6.7%	7.1%
Local	13.9%	22.2%	8.1%	8.2%

A factor that could have influenced the variation in the results is the time when the tests were run and the order they were run in. The base case was run two to three days prior to the repeated cases. Between the base case and the repeated cases, the tests involving the waves with seed variation were run. It is regarded as unlikely that the wavemaker dynamics are influenced by this. However, there could have been some small, unintentional changes in how the structure was fixed to the ocean basin bottom. There could also be uncertainties connected to how long time was allowed between tests in order to allow for the water to return to calm conditions.

7.3.2 Parameter Study on the Damping

From the decay tests it was determined that there was very little system damping, i.e. first mode damping ratio $\lambda_1 = 0.47\%$. This makes the system very sensitive with regards to damping as a small estimation error would give a large change in simulated response. Additionally, only the method of logarithmic decrement, which determines linear damping, has been used as an estimate of the total damping in the system. From the time series of the decay in Figure 7.3 where the structure was excited by a hit around the middle of the tower, it is seen that the linear damping gives a good estimate from around 150 seconds after the excitation. Before this it is seen that the linear damping does not fully describe the total damping in the system. It is therefore questionable if the damping estimated from the experimental decay test is representative also for simulations where the structure has input from waves. The irregular wave tests have been run for 50-year sea states, where the peak periods are in the interval $T_p \in [9, 13]$. From the RAOs in Section 7.2 it is seen that both the first-order and second-order response is important for large wave periods, as they are of the same order of magnitude. Interaction of different frequencies is expected so that the time series of the irregular waves will intuitively look more like the first 25 seconds of the decay in Figure 7.3 than the time series of the decay in Figure 7.4, for which the damping is estimated from. With this in mind, it seems very likely that the damping is underestimated. Thus, a parameter study on the damping was performed.

Selected results from the parameter study for test number 38010 are shown in Figure 7.15 to Figure 7.22. These figures show a comparison of the response spectra from the four different methods used to create wave kinematics in this work and the experimental results, for both mudline and waterline moment. For validation purposes, the equivalent spectra as the ones presented for test number 38010 are given in Appendix B. The discussion made for test 38010 is also valid for the other tests.

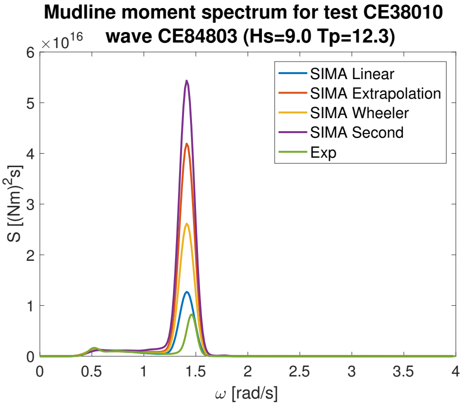

Figure 7.15: Mudline moment spectra for the four different simulated wave kinematics models compared to the experimental test. Simulations with damping ratio 0.47%.

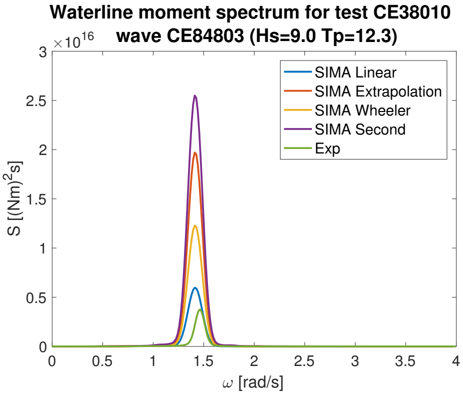

Figure 7.16: Waterline moment spectra for the four different simulated wave kinematics models compared to the experimental test. Simulations with damping ratio 0.47%.

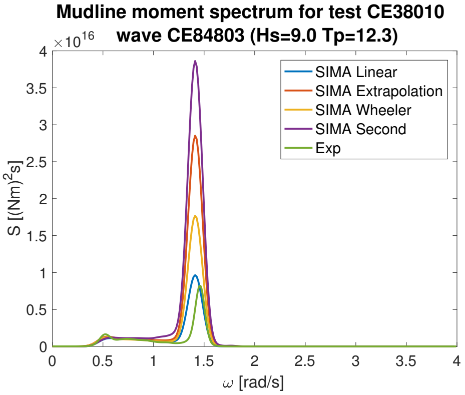

Figure 7.17: Mudline moment spectra for the four different simulated wave kinematics models compared to the experimental test. Simulations with damping ratio 0.68%.

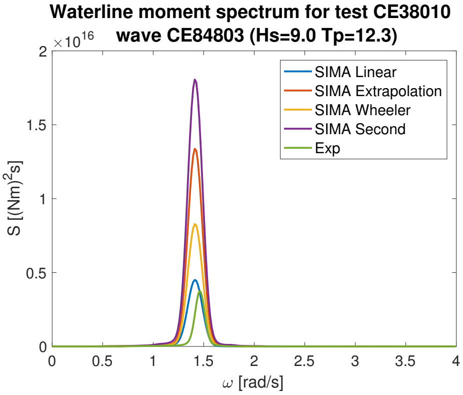

Figure 7.18: Waterline moment spectra for the four different simulated wave kinematics models compared to the experimental test. Simulations with damping ratio 0.68%.

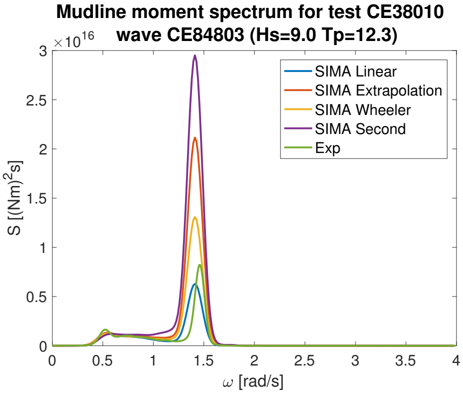

Figure 7.19: Mudline moment spectra for the four different simulated wave kinematics models compared to the experimental test. Simulations with damping ratio 0.89%.

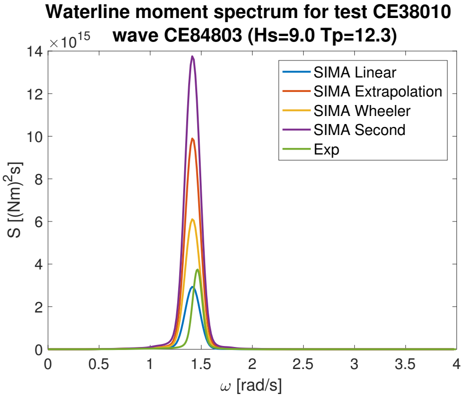

Figure 7.20: Waterline moment spectra for the four different simulated wave kinematics models compared to the experimental test. Simulations with damping ratio 0.89%.

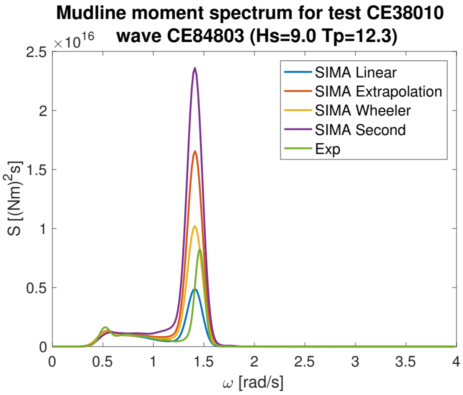

Figure 7.21: Mudline moment spectra for the four different simulated wave kinematics models compared to the experimental test. Simulations with damping ratio 1.10%.

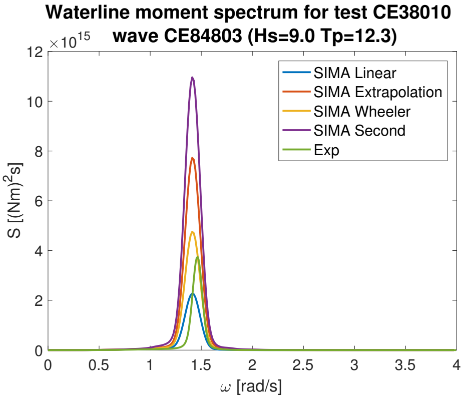

Figure 7.22: Waterline moment spectra for the four different simulated wave kinematics models compared to the experimental test. Simulations with damping ratio 1.10%.

Overall, the figures show that the majority of the response is concentrated around the first mode eigenfrequency. Around the eigenfrequency damping governs the response, as the inertia and stiffness terms cancel. It is therefore seen that a change in damping changes the peak height at the first mode eigenfrequency of the spectra close to linearly proportional. Comparing the mudline and waterline moment spectra, it is seen that the mudline moment spectra have response both around the eigenfrequency and a band at slightly lower frequency. This corresponds to response at wave frequencies (peak wave frequency

$\omega_p = 0.51\ rad/s$ for test number CE38010). When the structure is excited by waves the response is taken up by either inertia, damping or stiffness. The wave forces will act on the structure as a distributed load with decaying amplitude towards the sea bottom. If the wave forces are simplified into an equivalent point load with a point of attack, this point of attack would intuitively be located somewhere below waterline, but above mudline. Most of the forces will be transferred to the sea bottom fixed boundary through the stiffness of the structure. Thus, the wave forces do not excite a moment response at waterline. At waterline the response is explained by forces taken up by inertia.

For the simulated response it is seen that linear theory gives rise to the lowest response, followed by Wheeler stretching and simple extrapolation of linear wave kinematics, while second-order theory estimates the largest response. For the damping ratio of 0.47% estimated from the decay tests, it is seen in Figure 7.15 and Figure 7.16 that the experimental test response is overestimated by all simulated responses. This seems peculiar since a 50-year sea state with large significant wave height is considered and linear theory often is referred to as small-amplitude theory since the surface elevation is based on a linearized free surface condition. Thus, it was expected that pure linear theory it would underestimate the response. Although the simulated response is slightly lower in Figure 7.17 and Figure 7.18, when the damping ratio is increased to 0.68% all simulated responses still overestimate the experimental response. It seems very likely that the two first damping ratios in the parameter study are too low to be realistic damping ratios for the simulations to represent the experimental response. The same argument can be made for damping ratio 0.89% in Figure 7.19 and Figure 7.18, where the peak in the spectrum for the experimental response is only slightly larger than that of the linear theory response.

Considering the last damping ratio of 1.10%, it is seen in Figure 7.21 and Figure 7.22 that the peak of the experimental response spectrum is close to that of the linear theory with Wheeler stretching. This seems more reasonable since Wheeler stretching introduces nonlinear (second-order) terms in the horizontal wave forces, making the moment nonlinear as well. It was mentioned in Chapter 2 that Schløer et al. (2016) makes the point that linear theory applied with Wheeler stretching may better approximate extreme loads than pure linear theory. However, it was also concluded that it was necessary to consider nonlinear wave loads, i.e. at least full second-order theory. Based on this, it is also likely that the damping ratio of 1.10% is too low to represent realistic damping of the system. It was pointed out in Section 6.5 that Suja-Thauvin et al. (2017) had found realistic damping ratios for similar full-scale structures to be up to 2.8%. With such a large damping ratio relative to what was estimated in the decay test in this work, it seems like the peak of the second-order theory response spectrum could be close to that of the experimental response. On the other hand, it seems unlikely that the damping ratio could be underestimated by a factor of approximately 6 from the decay tests.

In Section 6.6 it was specified that the second order waves were not simulated for as long as the other methods for generating wave kinematics. The results of the second order wave tests are therefore strictly not fully comparable to the other methods for generating wave kinematics when considering the response spectra. However, it is assumed that the results give an indication of the energy in the sea state that can be used for comparisons. Thus, the discussion that has been made regarding second-order wave are assumed to be valid also if the time series was run for its full length. When comparing single events, the length of the time series does not influence the results. Of course, if the event occurs after the end time for the second order wave results the foundation for comparison is absent.

Another issue that was introduced in Section 6.6, was that the surface elevation time series from the experiments were not band pass filtered when sampling the surface elevation for input to the simulations with linear wave kinematics, linear kinematics with simple extrapolation and Wheeler stretched linear kinematics. This was only done for the second-order waves. When considering the error that this may have introduced, it is possible to look at the response spectra. It is seen that there is no, or negligible, energy at what would be considered difference frequencies, i.e. at frequencies lower than the wave first-order wave frequencies. Additionally there is certainly no energy is seen for a mean value, i.e. at $\omega = 0$. Thus, the results obtained without bandpass filtering are considered valid.

7.3.3 Ringing Responses

Possible ringing responses are studied by investigating the time series from the experiments, both for the surface elevation and the response. In Chapter 2 ringing responses were characterized by a large, sudden amplification of the response which decays exponentially with the eigenfrequency of the structure. Ringing is usually triggered by a steep wave event, often following from relatively calm sea. Thus, the experimental time series were studied in order to find combinations of steep wave events and typical ringing responses. For this purpose the waterline moment was used as the response as the moment at waterline mainly is concentrated at the first mode eigenfrequency, which makes it easier to single out ringing responses. Ringing showed to be a quite frequent occurring phenomena for the experimental tests considered in this work. Therefore only two events have been included in the results. At the time of occurrence of the ringing events the simulated waterline moment response has also been studied, with the four different methods for generating wave kinematics in this work, in order to check if the ringing events occur in the simulations.

In Figure 7.23 the surface elevation is plotted together with the waterline line moment for test 37010 and shows a ringing event occurring following from a steep, large wave event at around $t = 2670\ s$. The wave clearly resembles a nonlinear wave, compared to the example of a second order wave shown in Figure 4.1. The wave has a steep crest and more rounded troughs, with a larger crest height than trough depth. A large amplification of the response is seen and the response decays at the eigenfrequency to steady state. This fits the description of a ringing event and resembles the ringing event in the Figure 2.1 which was taken from Faltinsen et al. (1995).

From Figure 7.24 it is seen that nothing resembling a ringing event occurs. There is no amplification of the response, which suggests that linear theory is not suited to describe a ringing event. In Figure 7.25, Figure 7.26 and Figure 7.27 for the response for extrapolated linear wave kinematics, Wheeler stretched linear wave kinematics and second-order wave kinematics respectively a large, sudden amplification is seen comparable to that of the experiment in both shape and magnitude. A decay is also seen for about three to four periods of oscillation before the first mode response is excited again. This suggests that introducing nonlinearities in the forces gives a closer approximation of the experimental response when subjected to large, steep wave events.

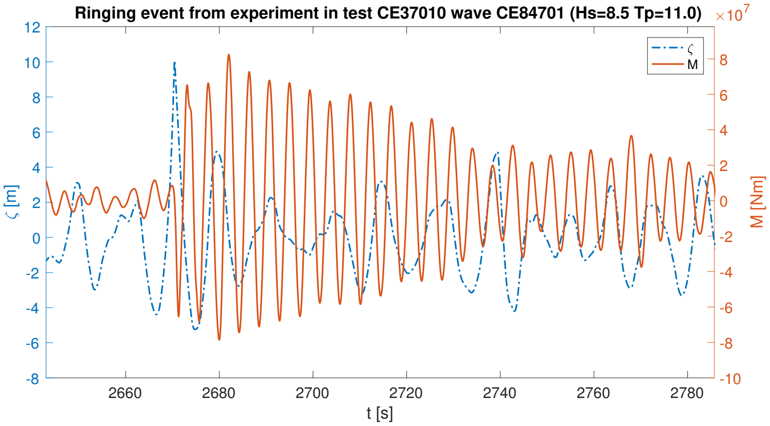

Figure 7.23: Surface elevation (blue) and waterline moment (red), showing a ringing event from the experiments in test number 37010

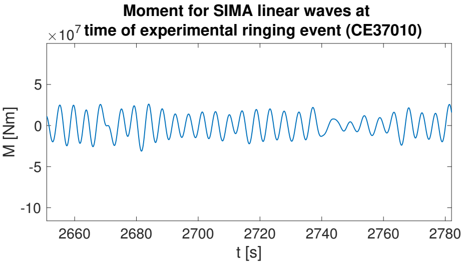

Figure 7.24: Waterline moment from simulation with linear theory at the time of the ringing event from the experiments in test number 37010

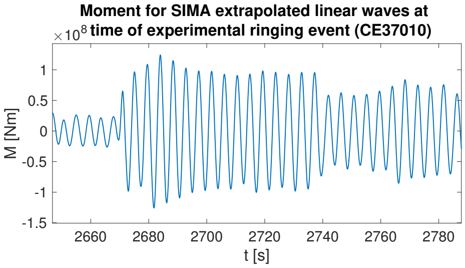

Figure 7.25: Waterline moment from simulation with simple extrapolation at the time of the ringing event from the experiments in test number 37010

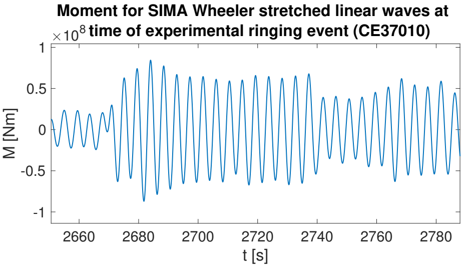

Figure 7.26: Waterline moment from simulation with Wheeler stretching at the time of the ringing event from the experiments in test number 37010

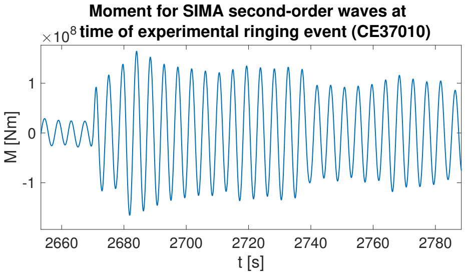

Figure 7.27: Waterline moment from simulation with second-order theory at the time of the ringing event from the experiments in test number 37010

Figure 7.28 shows a series of ringing responses in test number 38180, initiated by steep wave events at approximately $t = 9040\ s$, $t = 9090\ s$ and $t = 9170\ s$ respectively. For each of the large, steep wave events there is a sudden amplification followed by a decay at the eigenfrequency. The last ringing response is somewhat irregular compared to the two first events. However, not all ringing events can be expected to look like the event from Faltinsen et al. (1995) in Figure 2.1. From Figure 7.29, Figure 7.30 and Figure 7.31 it is seen that the simulations with linear wave kinematics, simple extrapolated linear wave kinematics and Wheeler stretched wave kinematics respectively estimate the response similarly in shape but with different magnitude. It is seen that the first mode is constantly excited in the simulations so that nothing resembling a ringing response can be found. From these results it seems as though the methods for wave kinematics used in the simulations are not able to describe ringing responses. It should be noted that since the second-order wave simulations are only simulated for 6553.5 seconds, it was not possible to include results from second-order theory for this test.

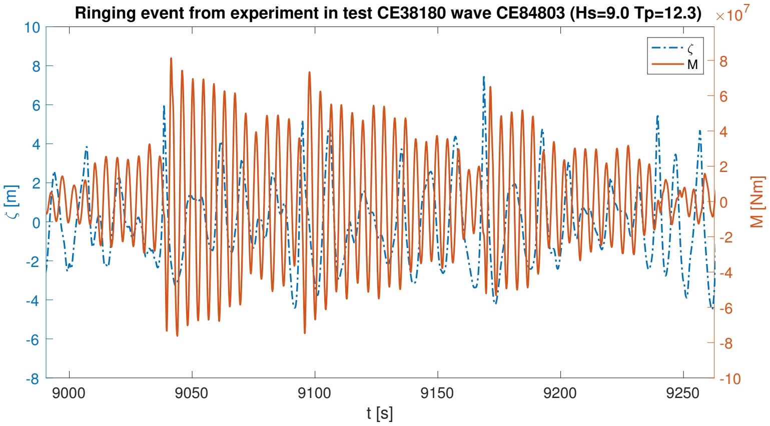

Figure 7.28: Surface elevation (blue) and waterline moment (red), showing a series of ringing events the experiments in test number 38180

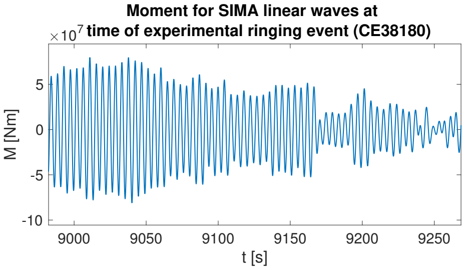

Figure 7.29: Waterline moment from simulation with linear theory at the time of the ringing event from the experiments in test number 38180

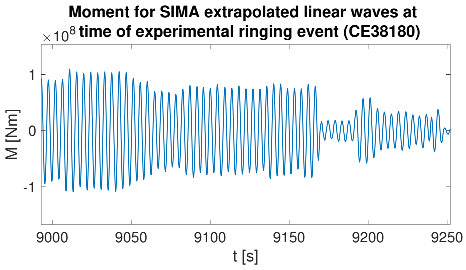

Figure 7.30: Waterline moment from simulation with simple extrapolation at the time of the ringing event from the experiments in test number 38180

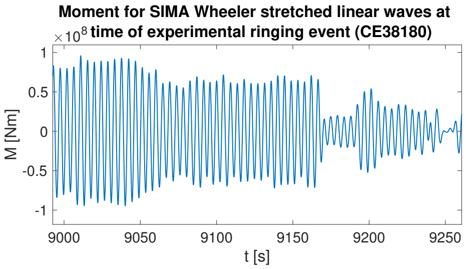

Figure 7.31: Waterline moment from simulation with Wheeler stretching at the time of the ringing event from the experiments in test number 38180

When the ringing events are considered it can be said that linear theory waves cannot predict ringing responses. When nonlinearities are introduced in the forces, i.e. through stretching techniques for linear wave kinematics or second-order theory, the response may in some cases resemble that of the experimental ringing events. However, the first mode response seems to be excited very easily in the simulations, making it difficult to see any definitive decay of the response even if there is a large amplification. Considering the results, it seems more likely than not that higher order forces than second-order must be introduced to better describe ringing responses. This is in accordance with what has been suggested in the literature, as described in Chapter 2. The FNV model presented in Section 4.4, adapted to intermediate water depths by Kristiansen & Faltinsen (2017) could very well give results for ringing responses resembling those of the experiments.

Three additional examples of ringing responses in the experimental tests are given in Appendix C for test numbers 38030, 38170 and 38110. The discussion made for the different wave kinematics models is also valid for the additional tests. It should be noted that test 38110 does not include second-order wave results, due to the same reason explained for test number 38180.

Chapter 8

Concluding Remarks

This thesis has examined the results from the experimental tests of a monopile supported offshore wind turbine, performed by the NOWITECH project, and compared the results against simulations. The focus has been put on validation of hydrodynamic load models, both linear and nonlinear, that can describe the response from the experiments, both at a statistical level and for single events, through simulations.

A beam element model was built in SIMA and presented as a starting point to this thesis. The model was calibrated based on available decay tests from the experiments to have the same system damping and first mode eigenfrequency as the experimental model. This was done by altering the stiffness of the mudpile, i.e. what represents the stiffness of the soil-structure interface. The first mode eigenfrequency was found to be $\omega_1 = 1.42 rad/s$, which is not far away from typical wave periods. It was therefore expected that the structure was susceptible to dynamics. The damping ratio was estimated as 0.47%, which is considered to be relatively low compared to similar monopile supported offshore wind turbines in full scale, where damping ratios have been found up to 2.8%. An eigenvalue analysis was also conducted to confirm the eigenfrequencies found from the decay tests. The simulated decay tests could only estimate the first and second mode eigenfrequencies, while the eigenvalue confirmed the third mode eigenfrequency as well. It was found that the error in the estimates for the second and third eigenfrequencies were 7.0% and 5.4% respectively, based on the eigenvalue analysis. The eigenvalue analysis also conveniently provided the modal shapes of the three first bending modes. These were in accordance with what was assumed by simplifying the structure as a cantilever beam. Overall the structural properties and behaviour of the simulation model was satisfactory compared to the experimental model after performing the model calibration tests.

Regular wave tests were treated to establish the RAOs for first, second and third order, i.e. filtered for multiples of the first-order wave frequency. The first-order RAOs displayed a reasonable behaviour of the response, with larger dynamic amplification closer to the first mode eigenperiod. Moreover the agreement between the simulated and experimental values was good. The second order RAO also showed good agreement between the simulated and experimental results, except for one wave period, $T = 9\ s$, where the simulated response strongly over-predicted the response. The period in question corresponds to approximately two times the eigenfrequency. For the simulations, Morison's equation with linear wave kinematics was used together with the MacCamy-Fuchs correction for diffraction was used. However, only linear diffraction is accounted for by this method. The over-prediction may be a result of not having the possibility to include second order diffraction effects in the simulations. The third order RAOs were of an order of magnitude lower than the first and second order RAOs. Thus, some uncertainty due to accuracy of measurements were connected to the third order RAOs.

A repeatability analysis was performed for the nine repeated irregular wave tests with input from wave number 84803. The repeatability analysis revealed through the coefficient of variation that the random error connected global maxima for the mudline and waterline moment response was quite low, so that the magnitude of global maxima are repeated very well. A considerably larger random error was connected to the repetition of the magnitude of single event maxima. The coefficient of variation was also considered for the maximum wave amplitude at two different wave probes. This revealed that both global maxima and single event maxima are repeated quite well.

A parameter study on the damping was initiated as the damping in the system, estimated from the decay tests was very low. Realistic damping ratios were found in the literature and considered. It is found that the originally estimated damping ratio is likely to not be representative of the system damping when the structure is subjected to waves. This is concluded based on linear theory overestimating the response from the experimental tests, which is contradictory to what is found in the literature when considering extreme sea states. If the more realistic damping ratio of 1.1% found in Suja-Thauvin et al. (2017) is accepted as the damping ratio for the structure, it was found that linear wave kinematics with Wheeler stretching is the most appropriate method for describing the energy in the response from the experimental tests.

Single events are considered by looking through time series for ringing responses. In agreement with the literature, it is found that in the experiments ringing responses are initiated by large, steep wave events. The ringing events characteristically have a large amplification from the steady state response and decays with the eigenfrequency for some periods. It is found that linear wave theory cannot describe ringing events. Introducing nonlinearities may in some cases better approximate the ringing response. However, more likely than not higher order than second order theory must be considered to properly describe the ringing phenomenon.

8.1 Recommendations for Further Work

As experimental tests have been performed there is a lot of different scenarios that can be investigated in connection to this work. Additionally, there are some parts of this work that could benefit from further attention.

- A definitive conclusion on what could be a reasonable damping ratio for the system when subjected to waves has not been made. The sensitivity of the structural response has been indicated. A conclusion on the structural damping should be made before proceeding to simulate cases for validation of the experimental results. Introduction of quadratic damping to the system could prove to be a good choice.
- The second-order wave simulations were only simulated for half the time originally planned. The second order waves should be simulated for the full length in order to make definitive conclusions on how it estimated the response overall.
- In order to better describe the ringing responses, the FNV method should be implemented. As the monopile supported offshore wind turbine hydrodynamically is located at intermediate water depths, the updated version of the FNV method, described by Kristiansen & Faltinsen (2017), should be given more attention.
- In this work only long-crested waves have been considered. In general short-crested waves give a more realistic picture of realistic ocean wave conditions. It could be of interest to look into the effect of short-crested waves on the response, compared to the results obtained for long-crested waves.
- Looking into fatigue conditions or extreme value statistics could also be interesting approaches to further investigate the NOWITECH test data.

Bibliography

Ahmed, F. & Kandagal, S. B. (2016), ‘ScienceDirect Modal Identification of Aircraft Wing Coupled Heave-Pitch Modes Using Wavelet Packet Decomposition and Logarithmic Decrement’, *Procedia Engineering* **144**, 435–443.

Bachynski, E. E. (2014), Design and Dynamic Analysis of Tension Leg Platform Wind Turbines, PhD thesis, NTNU.

Bachynski, E. E., Kristiansen, T. & Thys, M. (2017), ‘Experimental and numerical investigations of monopile ringing in irregular finite-depth water waves’, *Applied Ocean Research* **68**, 154–170.

Bachynski, E. E. & Moan, T. (2014), ‘Ringing loads on tension leg platform wind turbines’, *Ocean Engineering* **84**, 237–248.

Bell, K. (2013), *An Engineering Approach to Finite Element Analysis of Linear Structural Mechanics Problems*, Akademia Forlag.

Chakrabarti, S. K. (1987), *Hydrodynamics of offshore structures*, Computational Mechanics Publications.

Chaplin, J. R., Rainey, R. C. T. & Yemm, R. W. (1997), ‘Ringing of a vertical cylinder in waves’, *Journal of Fluid Mechanics* **350**, 119–147.

de Ridder, E. J., Aalberts, P., van den Berg, J., Buchner, B. & Peeringa, J. (2011), The Dynamic Response of an Offshore Wind Turbine With Realistic Flexibility to Breaking Wave Impact, *in* ‘Volume 5: Ocean Space Utilization; Ocean Renewable Energy’, ASME, pp. 543–552.

Dean, R. G. & Dalrymple, R. A. (1984), *Water wave mechanics for engineers and scientists*, Prentice-Hall.

DNV GL (2017), ‘Environmental conditions and environmental loads’, *DNVGL-RP-C205* .

Faltinsen, O. M. (1990), *Sea Loads*, Cambridge University Press.

Faltinsen, O. M., Newman, J. N. & Vinje, T. (1995), ‘Nonlinear wave loads on a slender vertical cylinder’, *Journal of Fluid Mechanics* **289**(1), 179–198.

Gavin, H. P. (2016), ‘Numerical Integration in Structural Dynamics’, *Department of Civil & Environmental Engineering, Duke University* .
URL: *http://people.duke.edu/ hpgavin/cee541/NumericalIntegration.pdf*

Grove, A. C. (1991), *An introduction to the Laplace transform and the z transform*, Prentice Hall.

Grue, J., Bjørshol, G. & Strand, Ø. (1993), ‘Higher harmonic wave exciting forces on a vertical cylinder’, *Matematisk Institutt, Universitetet i Oslo* .

Gurley, K. R. & Kareem, A. (1998), ‘Simulation of Ringing in Offshore Systems under Viscous Loads’, *Journal of Engineering Mechanics* **124**(5), 582–586.

Hasselmann, K., Barnett, T., Bouws, E., Carlson, H., Cartwright, D., Enke, K., Ewing, J., Gienapp, H., Hasselmann, D., Kruseman, P., Meerburg, A., Müller, P., Olbers, D., Richter, K., Sell, W. & Walden, H. (1973), *Measurements of wind-wave growth and swell decay during the joint North Sea wave project (JONSWAP)*, Deutsches Hydrographisches Institut.

Hughes, S. A. (1984), *The TMA shallow-water spectrum description and applications*, US Army Engineer Waterways Experiment Station, Coastal Engineering Research Center.

Johannessen, T. B. (2012), ‘Nonlinear Superposition Methods Applied to Continuous Ocean Wave Spectra’, *Journal of Offshore Mechanics and Arctic Engineering* **134**(1), 011302–1–011302–14.

Jonkman, J., Butterfield, S., Musial, W. & Scott, G. (2009), ‘Development, Definition of a 5-MW Reference Wind Turbine for Offshore System’, *Technical Report NREL/TP-500-38060* .

Jonkman, J. & Musial, W. (2010), ‘Offshore Code Comparison Collaboration (OC3) for IEA Task 23 Offshore Wind Technology and Deployment’, *Technical Report NREL/TP-5000-48191* .

Kristiansen, T. & Faltinsen, O. M. (2017), 'Higher harmonic wave loads on a vertical cylinder in finite water depth', *Journal of Fluid Mechanics* **833**, 773–805.

Krokstad, J. R., Stansberg, C. T., Nestegård, A. & Marthinsen, T. (1998), 'A New Non-slender Ringing Load Approach Verified Against Experiments', *Journal of Offshore Mechanics and Arctic Engineering* **120**(1), 20–29.

Li, L., Gao, Z. & Moan, T. (2015), 'Joint Distribution of Environmental Condition at Five European Offshore Sites for Design of Combined Wind and Wave Energy Devices', *Journal of Offshore Mechanics and Arctic Engineering* **137**(3), 0319011–1–0319011–16.

MacCamy, R. C. & Fuchs, R. A. (1954), 'Wave forces on piles: a diffraction theory', *Corps of Engineers* **Technical**.

Marthinsen, T. & Winterstein, S. R. (1992), 'On The Skewness Of Random Surface Waves'.

Morison, J., Johnson, J. & Schaaf, S. (1950), 'The Force Exerted by Surface Waves on Piles', *Journal of Petroleum Technology* **2**(5), 149–154.

Myrhaug, D. (2007), *Uregelmessig sjø*, Akademia Forlag.

Naess, A. & Moan, T. (2012), *Stochastic Dynamics of Marine Structures*, Cambridge University Press, Cambridge.

Newland, D. E. (1993), *An introduction to random vibrations, spectral and wavelet analysis*, 3rd edn, Longman.

Newman, J. N. (1977), *Marine Hydrodynamics*, MIT Press.

Newman, J. N. (1996), Nonlinear Scattering of Long Waves by a Vertical Cylinder, *in* 'Waves and Nonlinear Processes in Hydrodynamics', Springer, Dordrecht, pp. 91–102.

NOWITECH (2017), 'NOWITECH highlights'.

Ochi, M. K. (1990), *Applied probability and stochastic processes in engineering and physical sciences*, Wiley.

Schløer, S., Bredmose, H. & Bingham, H. B. (2016), 'The influence of fully nonlinear wave forces on aero-hydro-elastic calculations of monopile wind turbines', *Marine Structures* **50**, 162–188.

SINTEF Ocean (2017*a*), 'RIFLEX Theory Manual'.

SINTEF Ocean (2017*b*), 'RIFLEX User Guide'.

Stansberg, C. T. (1997), 'Comparing ringing loads from experiments with cylinders of different diameters : an empirical study', *8th International Conference on the Behaviour of Off-Shore Structures (BOSS'97)* .

Stansberg, C. T., Gudmestad, O. T. & Haver, S. K. (2008), 'Kinematics Under Extreme Waves', *Journal of Offshore Mechanics and Arctic Engineering* **130**(2), 021010–1–021010–7.

Steen, S. (2014), *Experimental Methods in Marine Hydrodynamics*, Department of Marine Technology.

Suja-Thauvin, L., Krokstad, J. R., Bachynski, E. E. & de Ridder, E.-J. (2017), 'Experimental results of a multimode monopile offshore wind turbine support structure subjected to steep and breaking irregular waves', *Ocean Engineering* **146**(September), 339–351.

Tejada, A. (2009), 'A Mode-Shape-Based Fault Detection Methodology for Cantilever Beams - NASA/CR-2009-215721', *Sponsoring Organization: NASA Langley Research Center* .

Thys, M. (2017), NOWITECH Bottom Fixed Wind Turbine Model Tests, Technical report, SINTEF Ocean.

WAFO-group (2011), *WAFO - A Matlab Toolbox for Analysis of Random Waves and Loads - A Tutorial*, Math. Stat., Center for Math. Sci., Lund Univ., Lund, Sweden.

Wheeler, J. (1970), 'Method for Calculating Forces Produced by Irregular Waves', *Journal of Petroleum Technology* **22**(03), 359–367.

Winder, S. (2002), *Analog and Digital Filter Design*, 2 edn, Newnes.

WindEurope (2017), 'The European offshore wind industry - Key trends and statistics 2016'.

Appendices

Appendix A

RAOs from Regular Wave Tests

A.1 Mudline Moment RAOs

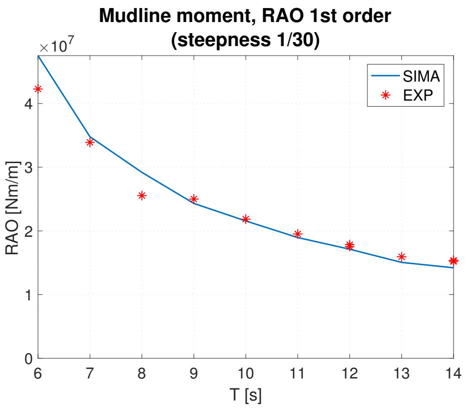

Figure A.1: 1^{st} order RAO for mudline moment from regular waves (steepness 1/30)

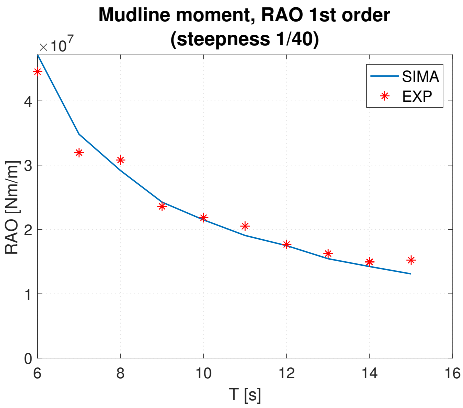

Figure A.2: 1^{st} order RAO for mudline moment from regular waves (steepness 1/40)

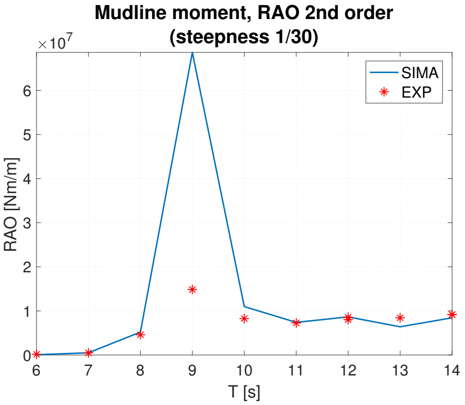

Figure A.3: 2^{nd} order RAO for mudline moment from regular waves (steepness 1/30)

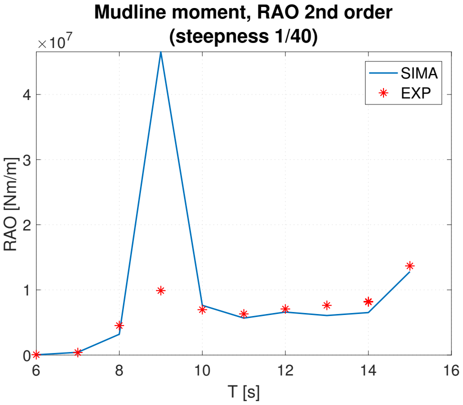

Figure A.4: 2^{nd} order RAO for mudline moment from regular waves (steepness 1/40)

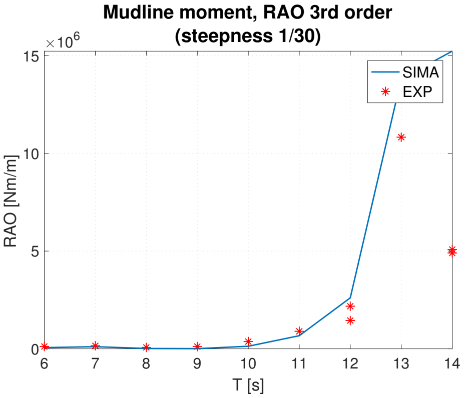

Figure A.5: 3^{rd} order RAO for mudline moment from regular waves (steepness 1/30)

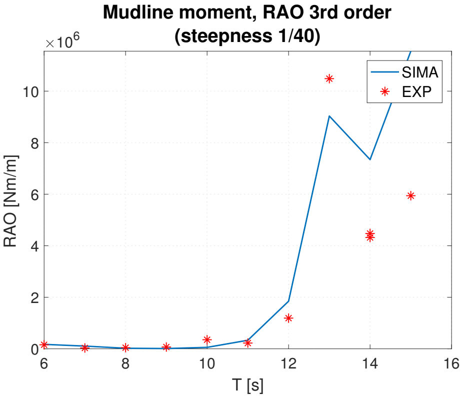

Figure A.6: 3^{rd} order RAO for mudline moment from regular waves (steepness 1/40)

A.2 Waterline Moment RAOs

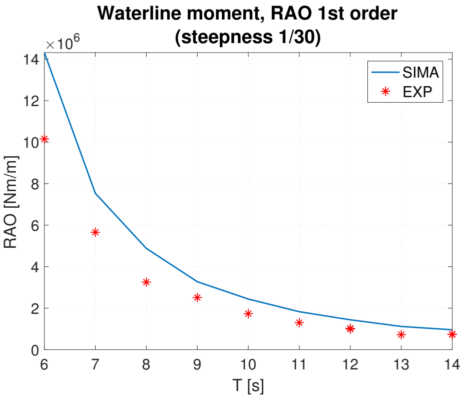

Figure A.7: 1^{st} order RAO for waterline moment from regular waves (steepness 1/30)

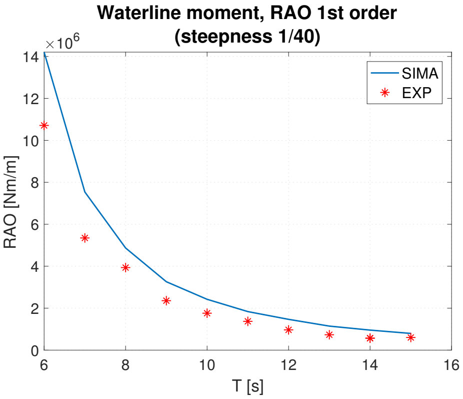

Figure A.8: 1^{st} order RAO for waterline moment from regular waves (steepness 1/40)

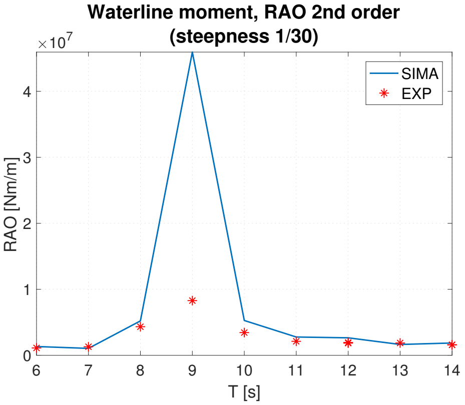

Figure A.9: 2^{nd} order RAO for waterline moment from regular waves (steepness 1/30)

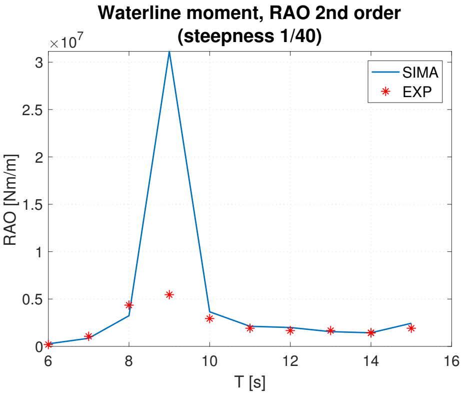

Figure A.10: 2^{nd} order RAO for waterline moment from regular waves (steepness 1/40)

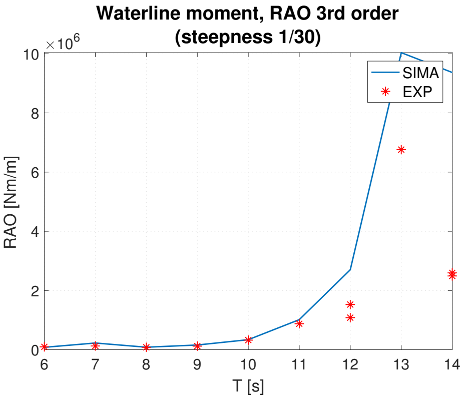

Figure A.11: 3^{rd} order RAO for waterline moment from regular waves (steepness 1/30)

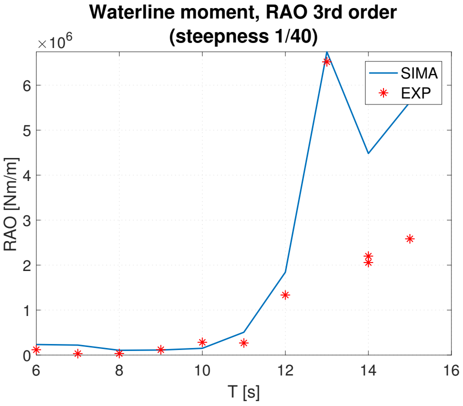

Figure A.12: 3^{rd} order RAO for waterline moment from regular waves (steepness 1/40)

Appendix B

Spectra for Irregular Wave Test Damping Parameter Study

B.1 Spectra for Test No. 35010

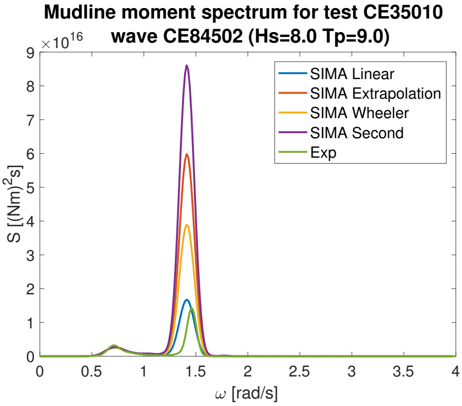

Figure B.1: Mudline moment spectra for the four different simulated wave kinematics models compared to the experimental test. Simulations with damping ratio 0.47%.

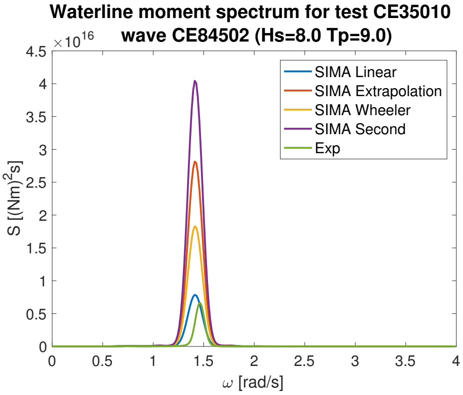

Figure B.2: Waterline moment spectra for the four different simulated wave kinematics models compared to the experimental test. Simulations with damping ratio 0.47%.

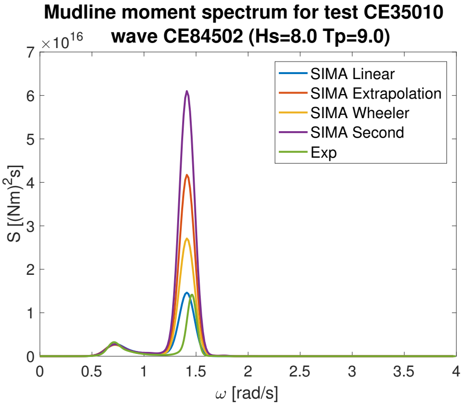

Figure B.3: Mudline moment spectra for the four different simulated wave kinematics models compared to the experimental test. Simulations with damping ratio 0.68%.

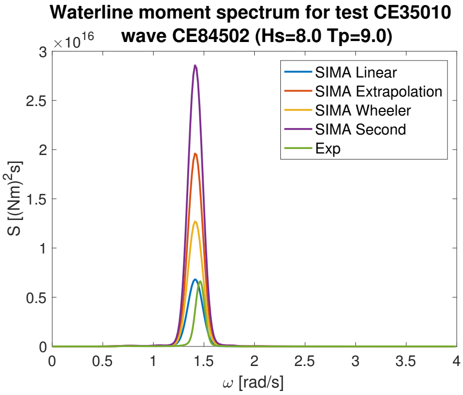

Figure B.4: Waterline moment spectra for the four different simulated wave kinematics models compared to the experimental test. Simulations with damping ratio 0.68%.

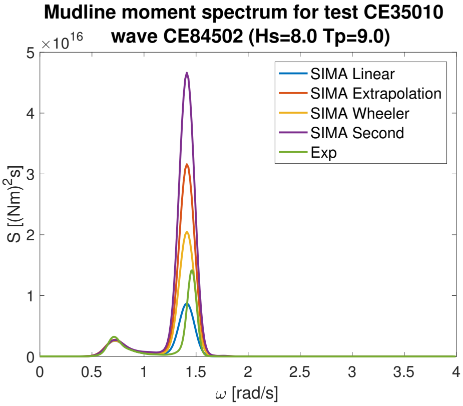

Figure B.5: Mudline moment spectra for the four different simulated wave kinematics models compared to the experimental test. Simulations with damping ratio 0.89%.

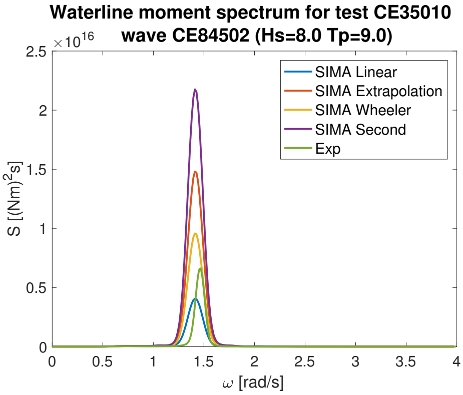

Figure B.6: Waterline moment spectra for the four different simulated wave kinematics models compared to the experimental test. Simulations with damping ratio 0.89%.

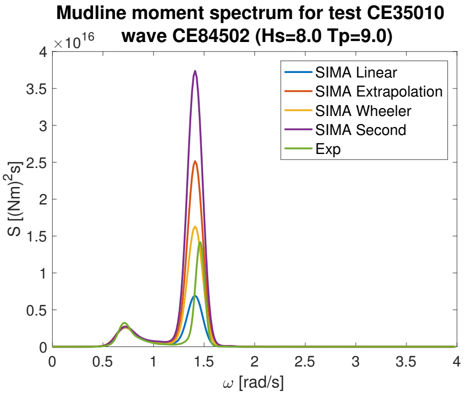

Figure B.7: Mudline moment spectra for the four different simulated wave kinematics models compared to the experimental test. Simulations with damping ratio 1.10%.

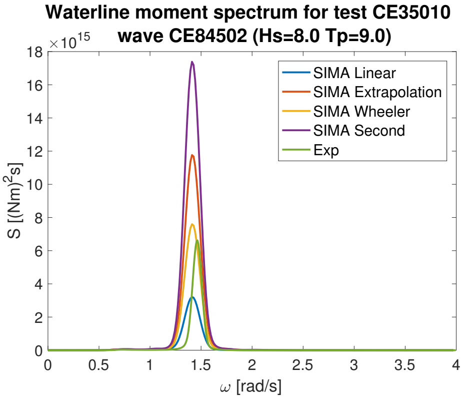

Figure B.8: Waterline moment spectra for the four different simulated wave kinematics models compared to the experimental test. Simulations with damping ratio 1.10%.

B.2 Spectra for Test No. 36010

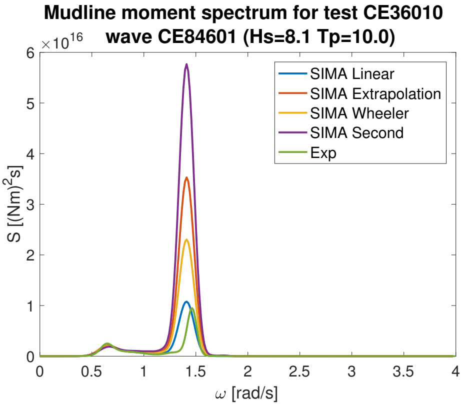

Figure B.9: Mudline moment spectra for the four different simulated wave kinematics models compared to the experimental test. Simulations with damping ratio 0.47%.

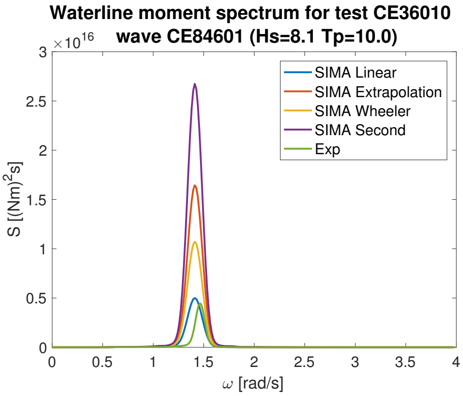

Figure B.10: Waterline moment spectra for the four different simulated wave kinematics models compared to the experimental test. Simulations with damping ratio 0.47%.

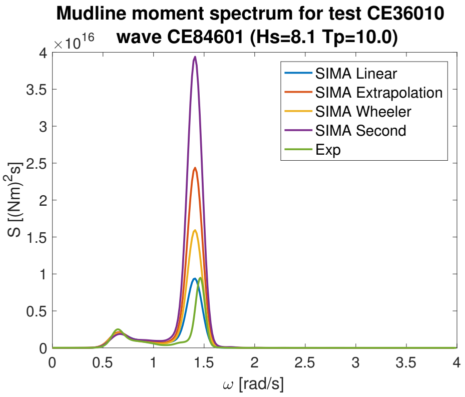

Figure B.11: Mudline moment spectra for the four different simulated wave kinematics models compared to the experimental test. Simulations with damping ratio 0.68%.

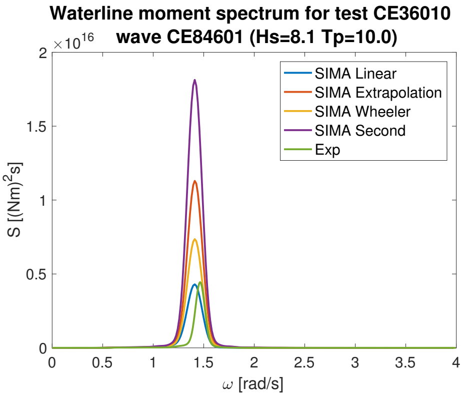

Figure B.12: Waterline moment spectra for the four different simulated wave kinematics models compared to the experimental test. Simulations with damping ratio 0.68%.

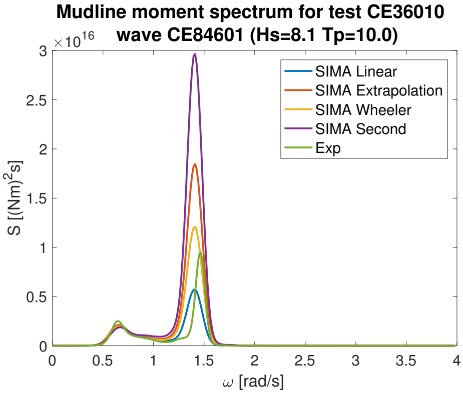

Figure B.13: Mudline moment spectra for the four different simulated wave kinematics models compared to the experimental test. Simulations with damping ratio 0.89%.

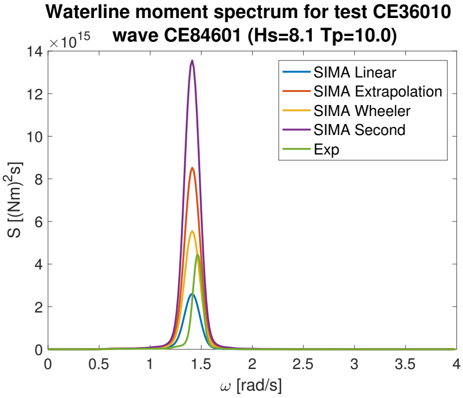

Figure B.14: Waterline moment spectra for the four different simulated wave kinematics models compared to the experimental test. Simulations with damping ratio 0.89%.

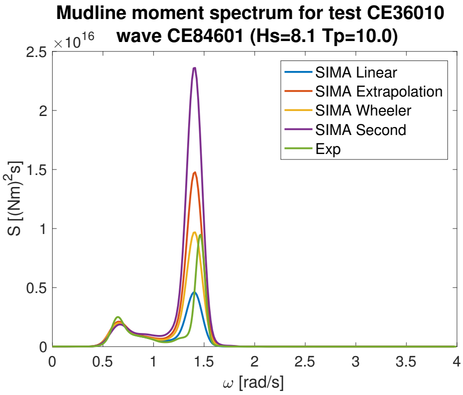

Figure B.15: Mudline moment spectra for the four different simulated wave kinematics models compared to the experimental test. Simulations with damping ratio 1.10%.

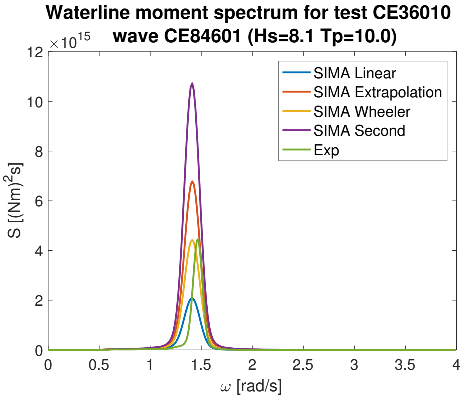

Figure B.16: Waterline moment spectra for the four different simulated wave kinematics models compared to the experimental test. Simulations with damping ratio 1.10%.

B.3 Spectra for Test No. 37010

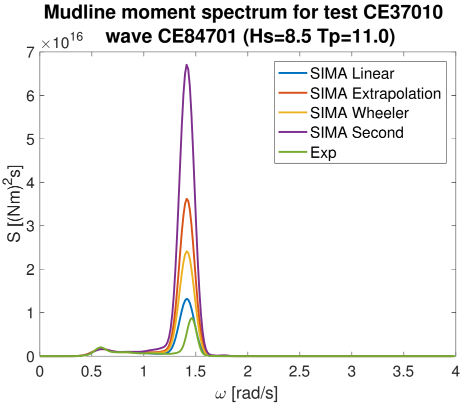

Figure B.17: Mudline moment spectra for the four different simulated wave kinematics models compared to the experimental test. Simulations with damping ratio 0.47%.

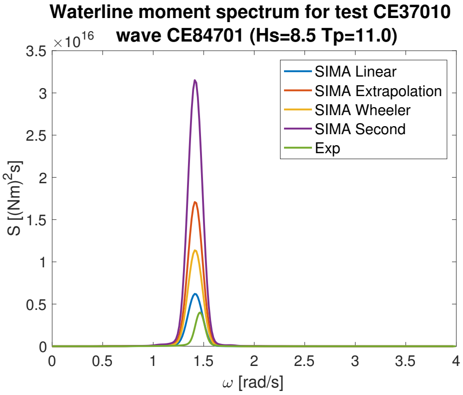

Figure B.18: Waterline moment spectra for the four different simulated wave kinematics models compared to the experimental test. Simulations with damping ratio 0.47%.

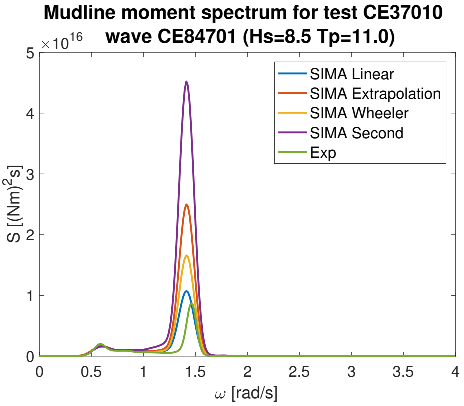

Figure B.19: Mudline moment spectra for the four different simulated wave kinematics models compared to the experimental test. Simulations with damping ratio 0.68%.

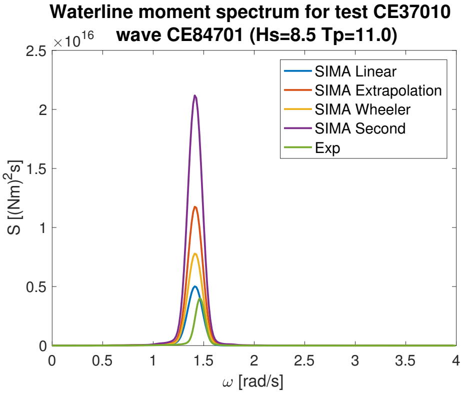

Figure B.20: Waterline moment spectra for the four different simulated wave kinematics models compared to the experimental test. Simulations with damping ratio 0.68%.

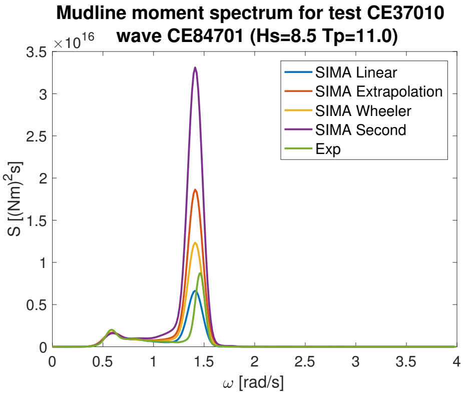

Figure B.21: Mudline moment spectra for the four different simulated wave kinematics models compared to the experimental test. Simulations with damping ratio 0.89%.

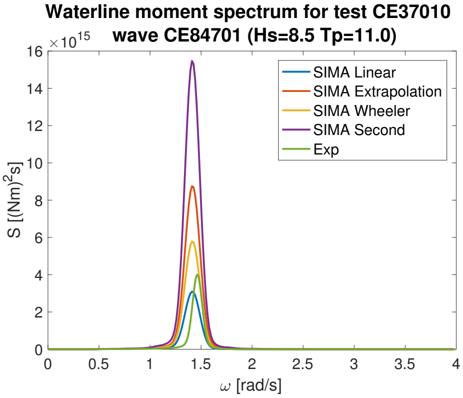

Figure B.22: Waterline moment spectra for the four different simulated wave kinematics models compared to the experimental test. Simulations with damping ratio 0.89%.

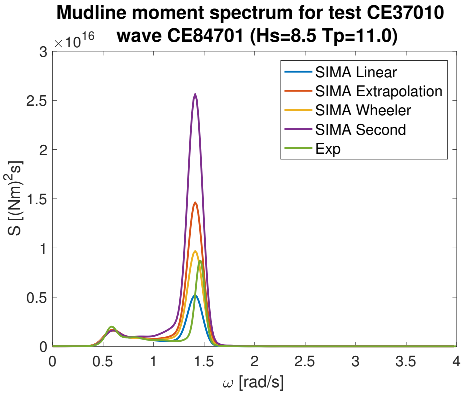

Figure B.23: Mudline moment spectra for the four different simulated wave kinematics models compared to the experimental test. Simulations with damping ratio 1.10%.

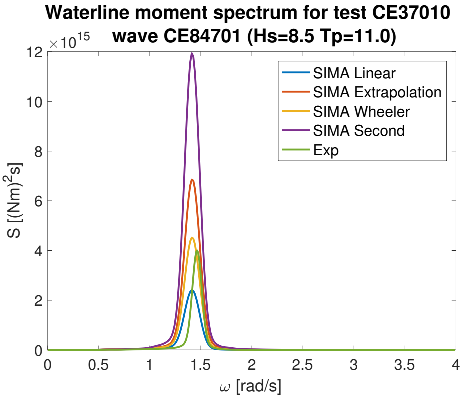

Figure B.24: Waterline moment spectra for the four different simulated wave kinematics models compared to the experimental test. Simulations with damping ratio 1.10%.

B.4 Spectra for Test No. 38010

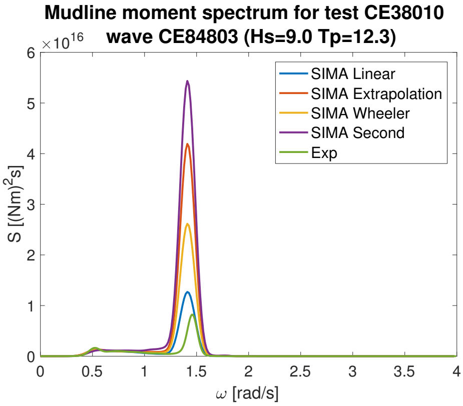

Figure B.25: Mudline moment spectra for the four different simulated wave kinematics models compared to the experimental test. Simulations with damping ratio 0.47%.

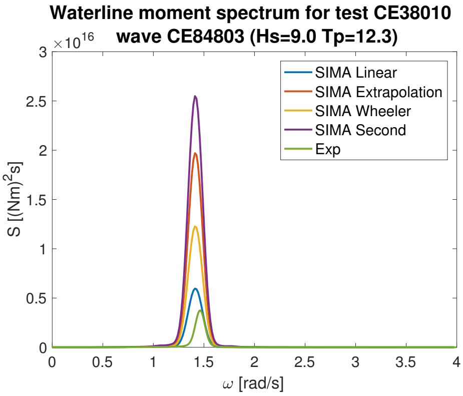

Figure B.26: Waterline moment spectra for the four different simulated wave kinematics models compared to the experimental test. Simulations with damping ratio 0.47%.

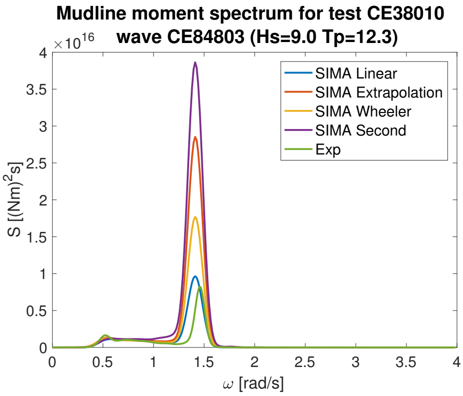

Figure B.27: Mudline moment spectra for the four different simulated wave kinematics models compared to the experimental test. Simulations with damping ratio 0.68%.

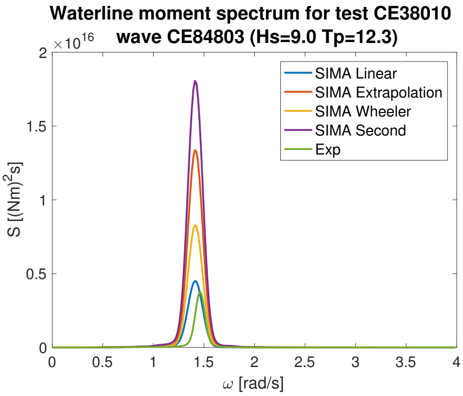

Figure B.28: Waterline moment spectra for the four different simulated wave kinematics models compared to the experimental test. Simulations with damping ratio 0.68%.

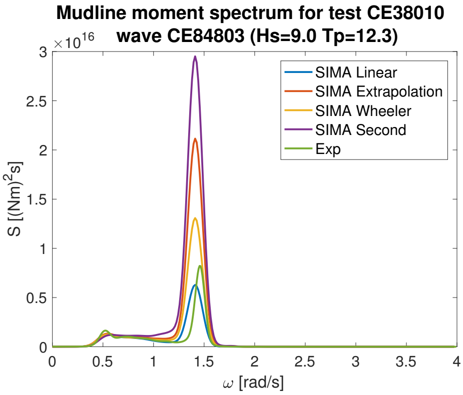

Figure B.29: Mudline moment spectra for the four different simulated wave kinematics models compared to the experimental test. Simulations with damping ratio 0.89%.

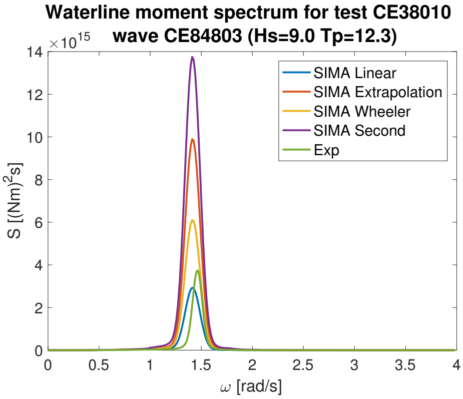

Figure B.30: Waterline moment spectra for the four different simulated wave kinematics models compared to the experimental test. Simulations with damping ratio 0.89%.

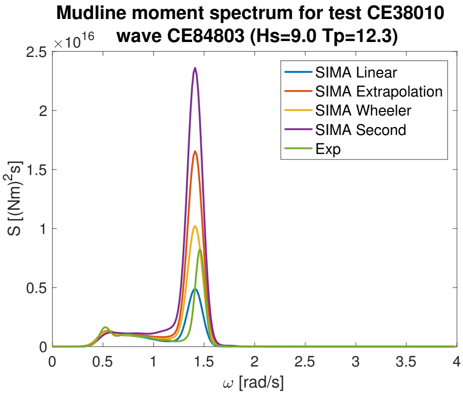

Figure B.31: Mudline moment spectra for the four different simulated wave kinematics models compared to the experimental test. Simulations with damping ratio 1.10%.

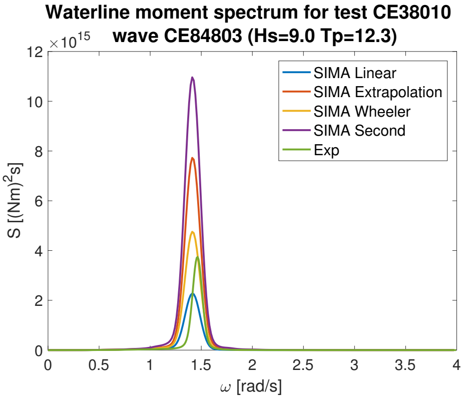

Figure B.32: Waterline moment spectra for the four different simulated wave kinematics models compared to the experimental test. Simulations with damping ratio 1.10%.

B.5 Spectra for Test No. 38020

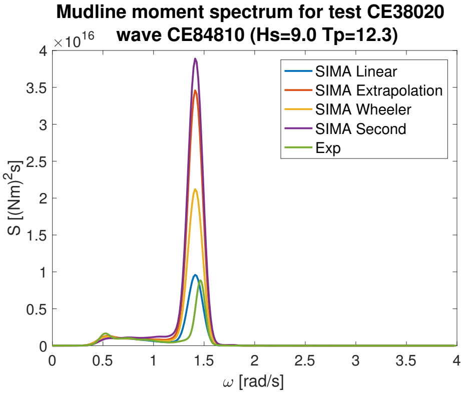

Figure B.33: Mudline moment spectra for the four different simulated wave kinematics models compared to the experimental test. Simulations with damping ratio 0.47%.

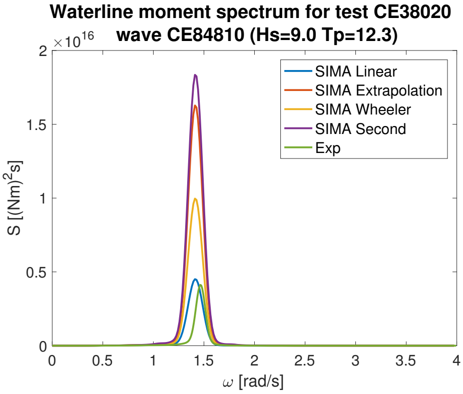

Figure B.34: Waterline moment spectra for the four different simulated wave kinematics models compared to the experimental test. Simulations with damping ratio 0.47%.

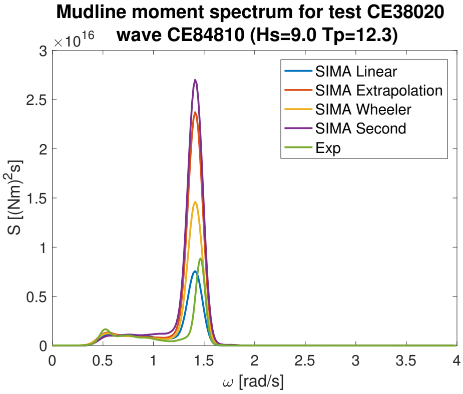

Figure B.35: Mudline moment spectra for the four different simulated wave kinematics models compared to the experimental test. Simulations with damping ratio 0.68%.

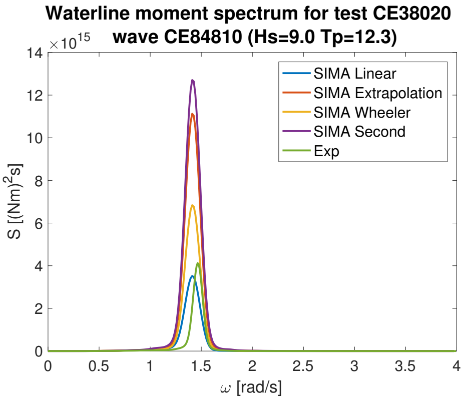

Figure B.36: Waterline moment spectra for the four different simulated wave kinematics models compared to the experimental test. Simulations with damping ratio 0.68%.

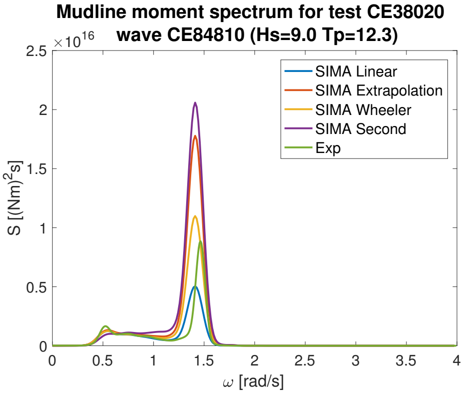

Figure B.37: Mudline moment spectra for the four different simulated wave kinematics models compared to the experimental test. Simulations with damping ratio 0.89%.

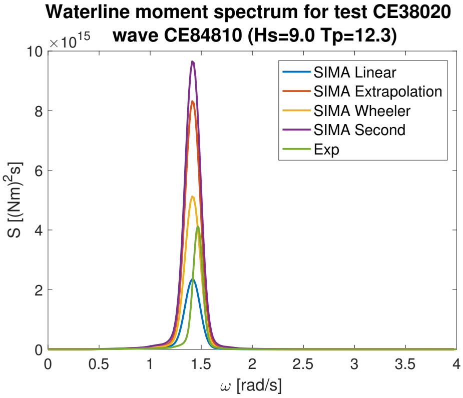

Figure B.38: Waterline moment spectra for the four different simulated wave kinematics models compared to the experimental test. Simulations with damping ratio 0.89%.

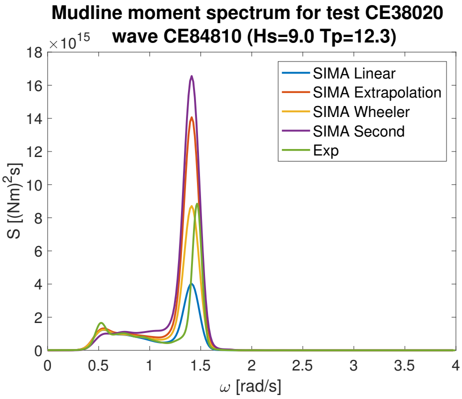

Figure B.39: Mudline moment spectra for the four different simulated wave kinematics models compared to the experimental test. Simulations with damping ratio 1.10%.

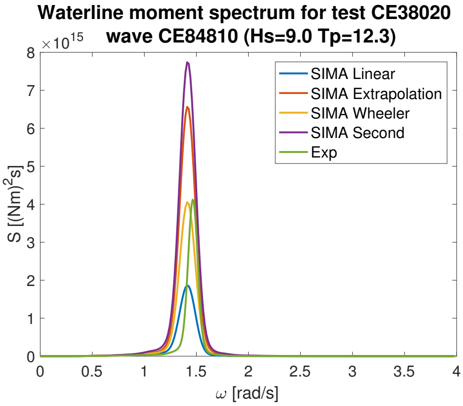

Figure B.40: Waterline moment spectra for the four different simulated wave kinematics models compared to the experimental test. Simulations with damping ratio 1.10%.

B.6 Spectra for Test No. 38030

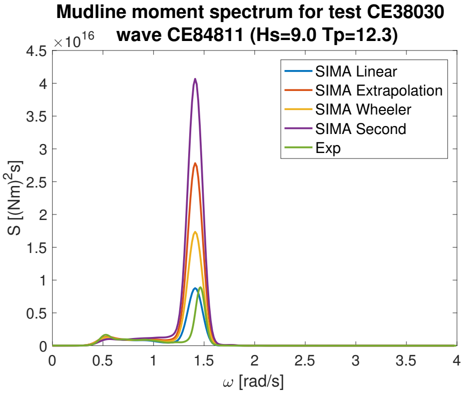

Figure B.41: Mudline moment spectra for the four different simulated wave kinematics models compared to the experimental test. Simulations with damping ratio 0.47%.

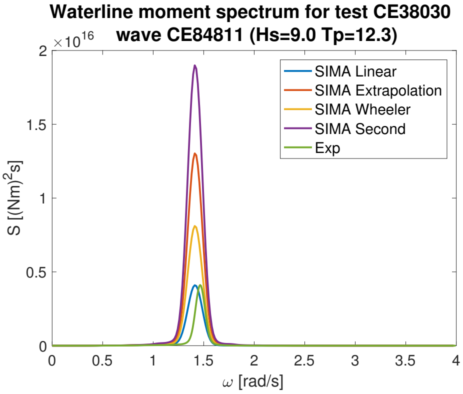

Figure B.42: Waterline moment spectra for the four different simulated wave kinematics models compared to the experimental test. Simulations with damping ratio 0.47%.

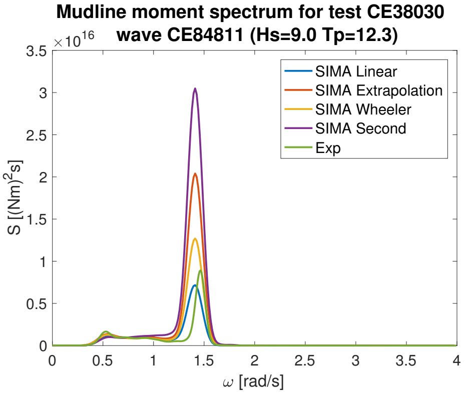

Figure B.43: Mudline moment spectra for the four different simulated wave kinematics models compared to the experimental test. Simulations with damping ratio 0.68%.

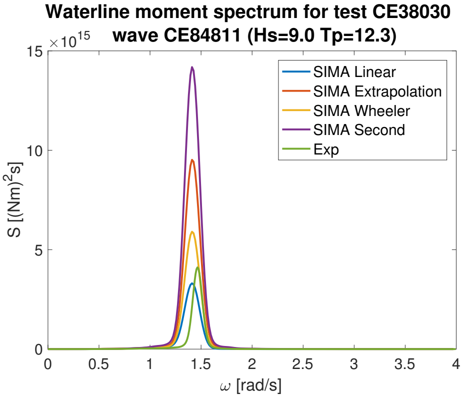

Figure B.44: Waterline moment spectra for the four different simulated wave kinematics models compared to the experimental test. Simulations with damping ratio 0.68%.

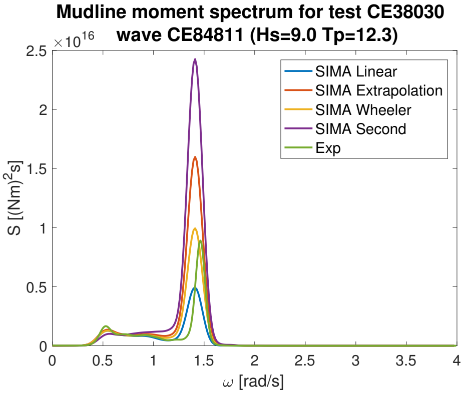

Figure B.45: Mudline moment spectra for the four different simulated wave kinematics models compared to the experimental test. Simulations with damping ratio 0.89%.

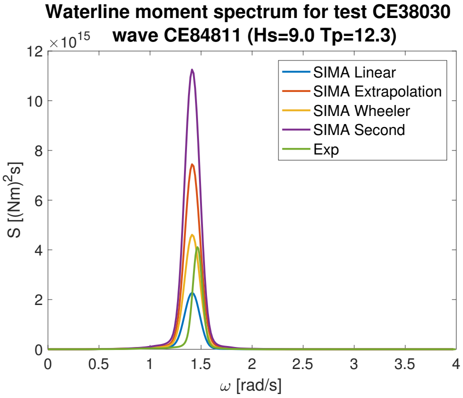

Figure B.46: Waterline moment spectra for the four different simulated wave kinematics models compared to the experimental test. Simulations with damping ratio 0.89%.

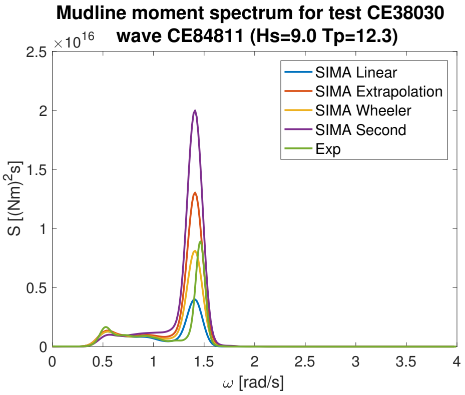

Figure B.47: Mudline moment spectra for the four different simulated wave kinematics models compared to the experimental test. Simulations with damping ratio 1.10%.

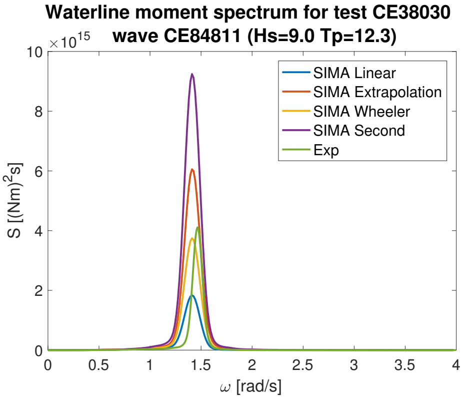

Figure B.48: Waterline moment spectra for the four different simulated wave kinematics models compared to the experimental test. Simulations with damping ratio 1.10%.

B.7 Spectra for Test No. 38040

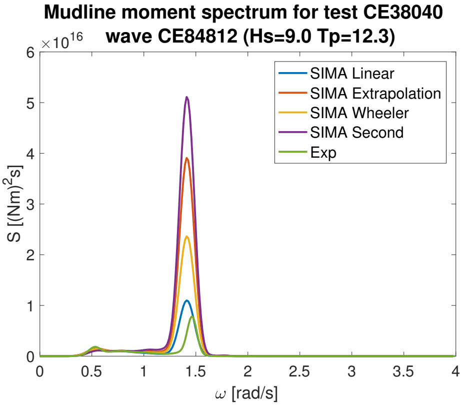

Figure B.49: Mudline moment spectra for the four different simulated wave kinematics models compared to the experimental test. Simulations with damping ratio 0.47%.

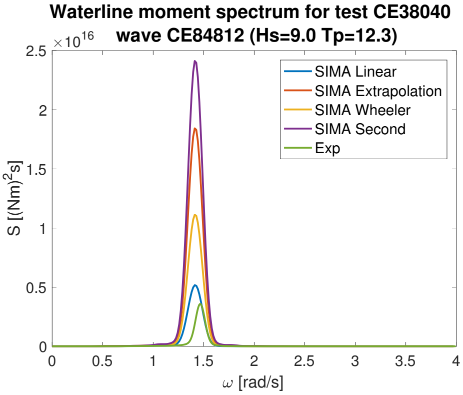

Figure B.50: Waterline moment spectra for the four different simulated wave kinematics models compared to the experimental test. Simulations with damping ratio 0.47%.

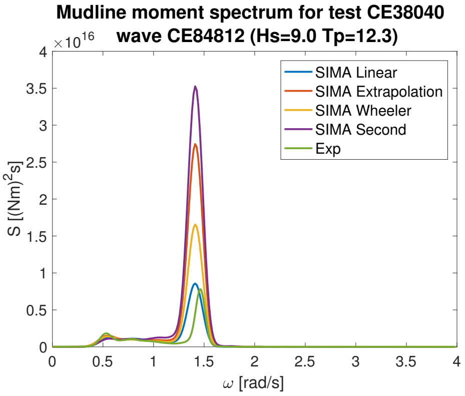

Figure B.51: Mudline moment spectra for the four different simulated wave kinematics models compared to the experimental test. Simulations with damping ratio 0.68%.

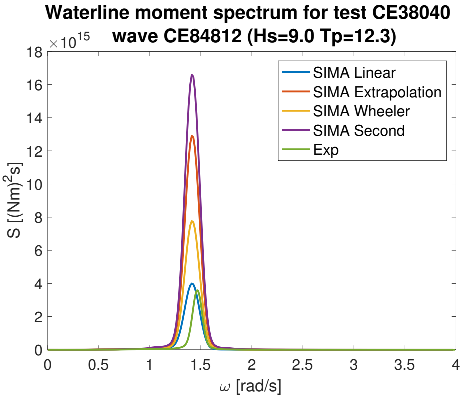

Figure B.52: Waterline moment spectra for the four different simulated wave kinematics models compared to the experimental test. Simulations with damping ratio 0.68%.

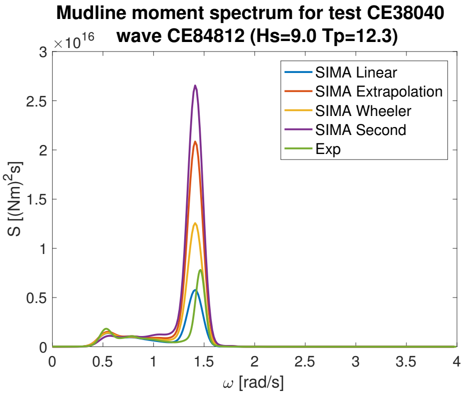

Figure B.53: Mudline moment spectra for the four different simulated wave kinematics models compared to the experimental test. Simulations with damping ratio 0.89%.

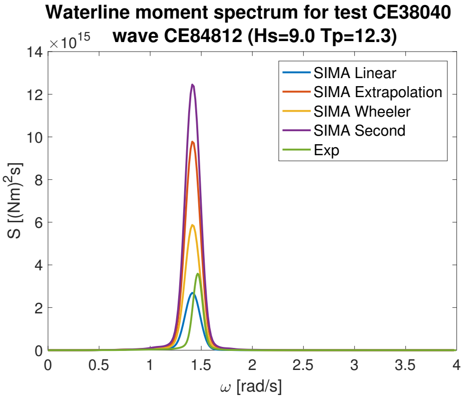

Figure B.54: Waterline moment spectra for the four different simulated wave kinematics models compared to the experimental test. Simulations with damping ratio 0.89%.

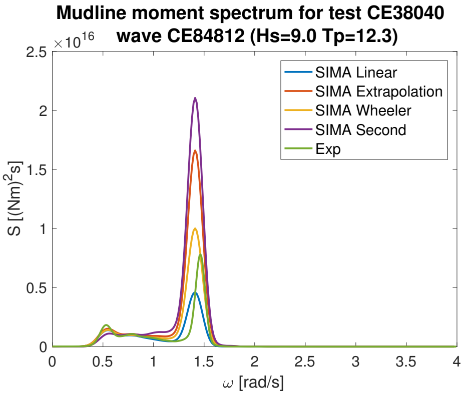

Figure B.55: Mudline moment spectra for the four different simulated wave kinematics models compared to the experimental test. Simulations with damping ratio 1.10%.

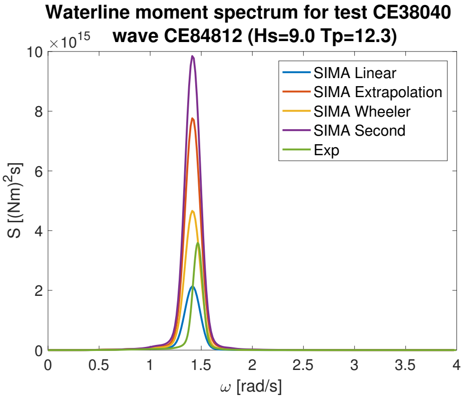

Figure B.56: Waterline moment spectra for the four different simulated wave kinematics models compared to the experimental test. Simulations with damping ratio 1.10%.

B.8 Spectra for Test No. 38110

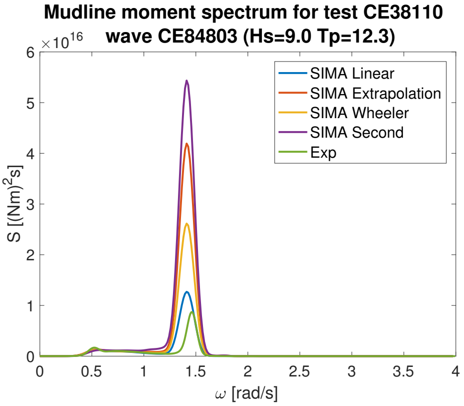

Figure B.57: Mudline moment spectra for the four different simulated wave kinematics models compared to the experimental test. Simulations with damping ratio 0.47%.

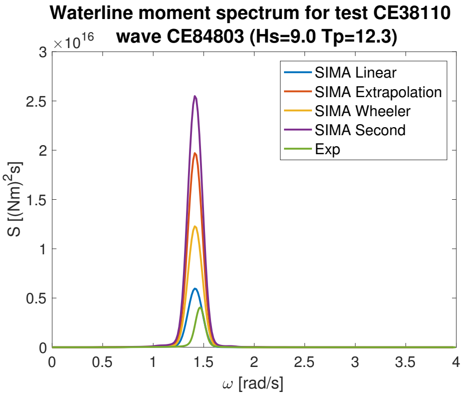

Figure B.58: Waterline moment spectra for the four different simulated wave kinematics models compared to the experimental test. Simulations with damping ratio 0.47%.

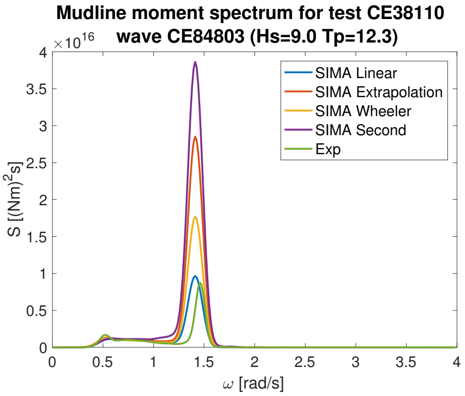

Figure B.59: Mudline moment spectra for the four different simulated wave kinematics models compared to the experimental test. Simulations with damping ratio 0.68%.

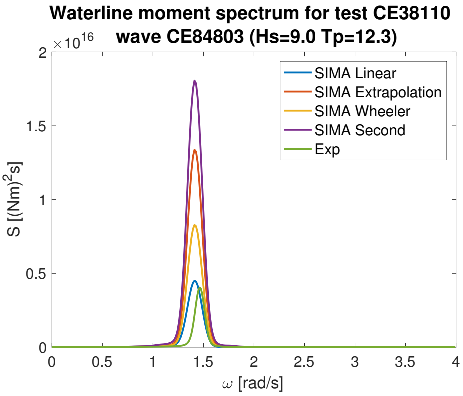

Figure B.60: Waterline moment spectra for the four different simulated wave kinematics models compared to the experimental test. Simulations with damping ratio 0.68%.

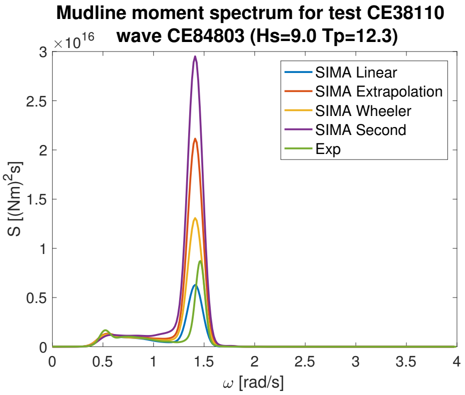

Figure B.61: Mudline moment spectra for the four different simulated wave kinematics models compared to the experimental test. Simulations with damping ratio 0.89%.

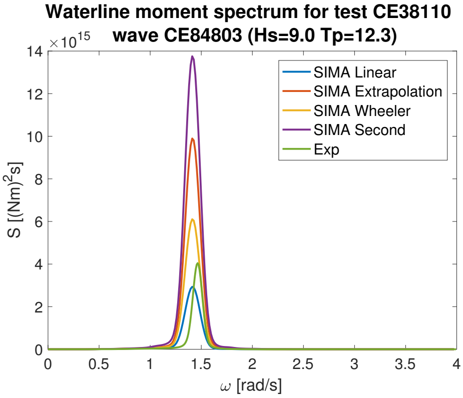

Figure B.62: Waterline moment spectra for the four different simulated wave kinematics models compared to the experimental test. Simulations with damping ratio 0.89%.

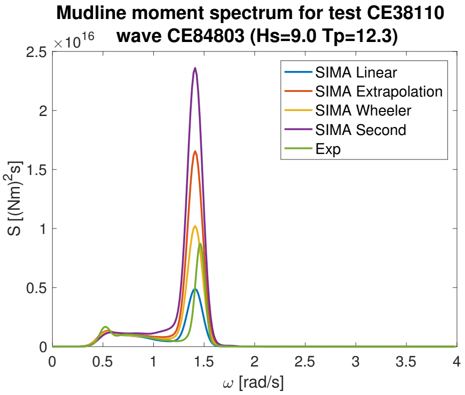

Figure B.63: Mudline moment spectra for the four different simulated wave kinematics models compared to the experimental test. Simulations with damping ratio 1.10%.

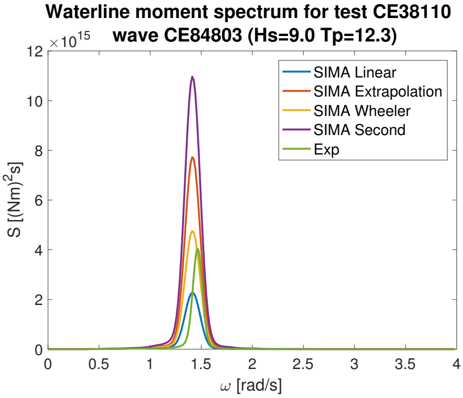

Figure B.64: Waterline moment spectra for the four different simulated wave kinematics models compared to the experimental test. Simulations with damping ratio 1.10%.

B.9 Spectra for Test No. 38120

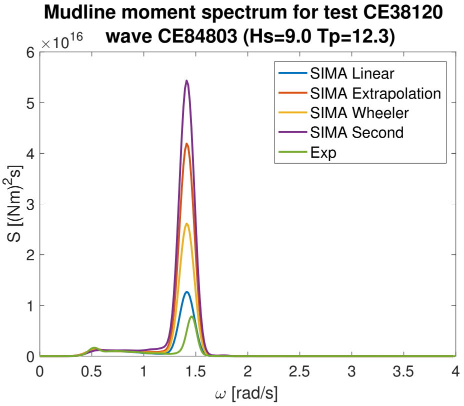

Figure B.65: Mudline moment spectra for the four different simulated wave kinematics models compared to the experimental test. Simulations with damping ratio 0.47%.

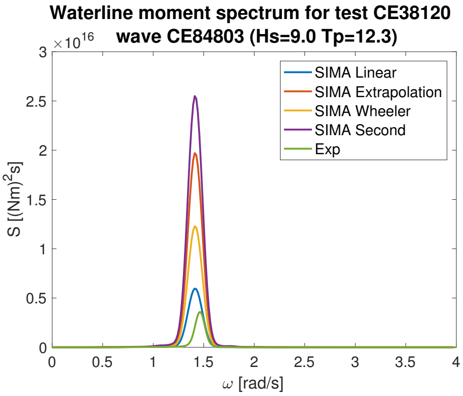

Figure B.66: Waterline moment spectra for the four different simulated wave kinematics models compared to the experimental test. Simulations with damping ratio 0.47%.

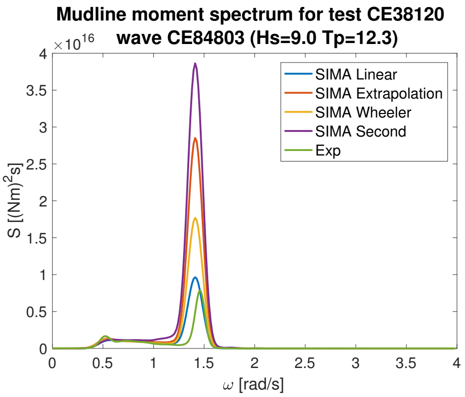

Figure B.67: Mudline moment spectra for the four different simulated wave kinematics models compared to the experimental test. Simulations with damping ratio 0.68%.

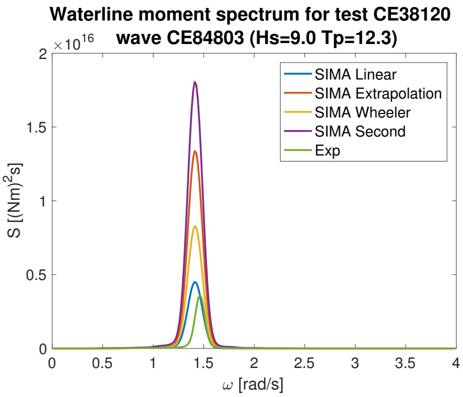

Figure B.68: Waterline moment spectra for the four different simulated wave kinematics models compared to the experimental test. Simulations with damping ratio 0.68%.

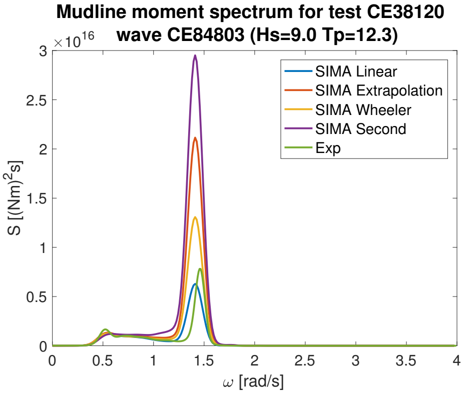

Figure B.69: Mudline moment spectra for the four different simulated wave kinematics models compared to the experimental test. Simulations with damping ratio 0.89%.

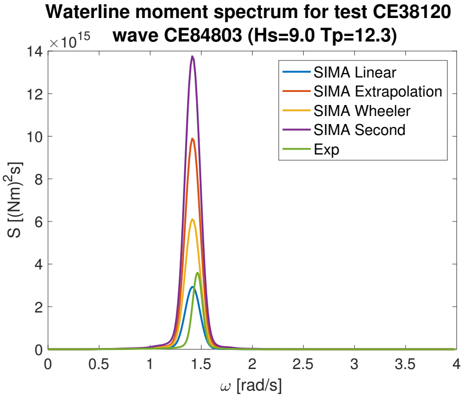

Figure B.70: Waterline moment spectra for the four different simulated wave kinematics models compared to the experimental test. Simulations with damping ratio 0.89%.

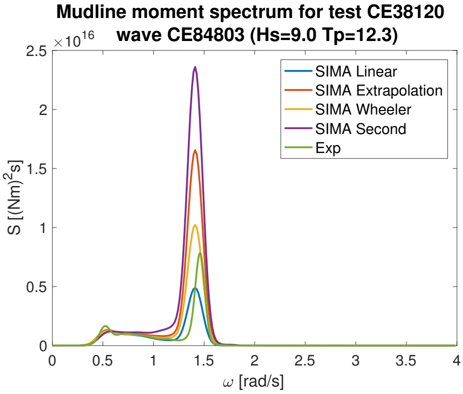

Figure B.71: Mudline moment spectra for the four different simulated wave kinematics models compared to the experimental test. Simulations with damping ratio 1.10%.

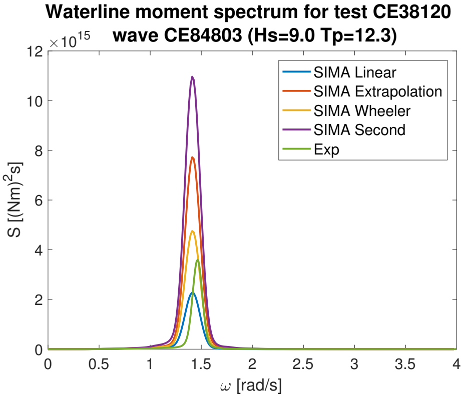

Figure B.72: Waterline moment spectra for the four different simulated wave kinematics models compared to the experimental test. Simulations with damping ratio 1.10%.

B.10 Spectra for Test No. 38130

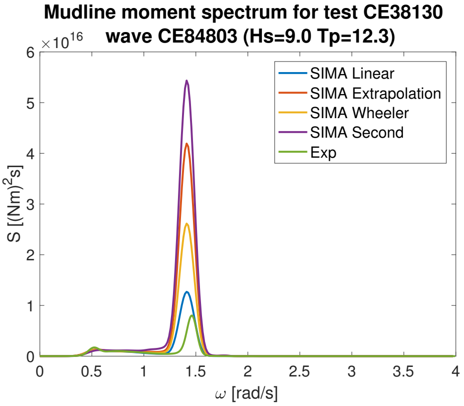

Figure B.73: Mudline moment spectra for the four different simulated wave kinematics models compared to the experimental test. Simulations with damping ratio 0.47%.

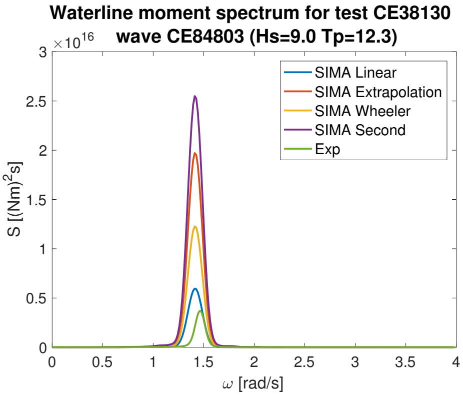

Figure B.74: Waterline moment spectra for the four different simulated wave kinematics models compared to the experimental test. Simulations with damping ratio 0.47%.

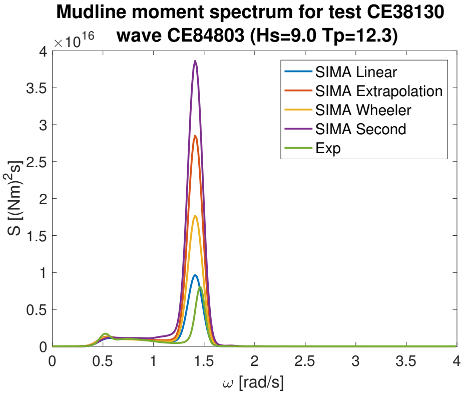

Figure B.75: Mudline moment spectra for the four different simulated wave kinematics models compared to the experimental test. Simulations with damping ratio 0.68%.

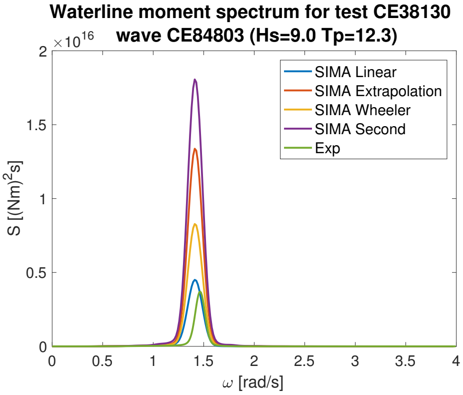

Figure B.76: Waterline moment spectra for the four different simulated wave kinematics models compared to the experimental test. Simulations with damping ratio 0.68%.

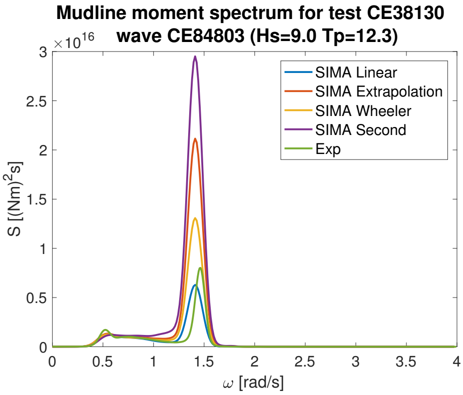

Figure B.77: Mudline moment spectra for the four different simulated wave kinematics models compared to the experimental test. Simulations with damping ratio 0.89%.

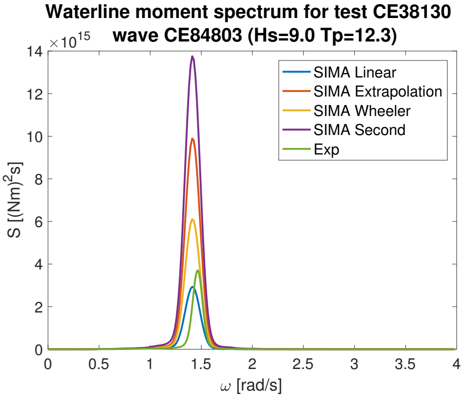

Figure B.78: Waterline moment spectra for the four different simulated wave kinematics models compared to the experimental test. Simulations with damping ratio 0.89%.

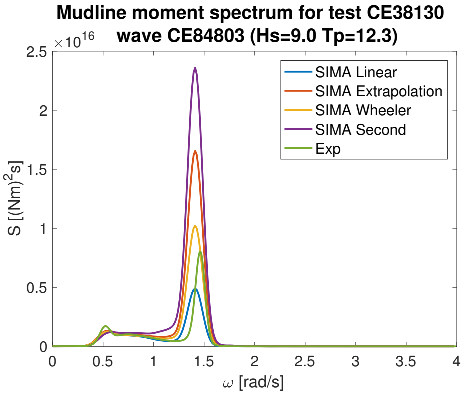

Figure B.79: Mudline moment spectra for the four different simulated wave kinematics models compared to the experimental test. Simulations with damping ratio 1.10%.

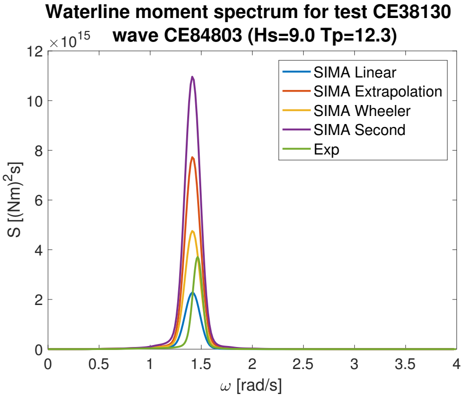

Figure B.80: Waterline moment spectra for the four different simulated wave kinematics models compared to the experimental test. Simulations with damping ratio 1.10%.

B.11 Spectra for Test No. 38140

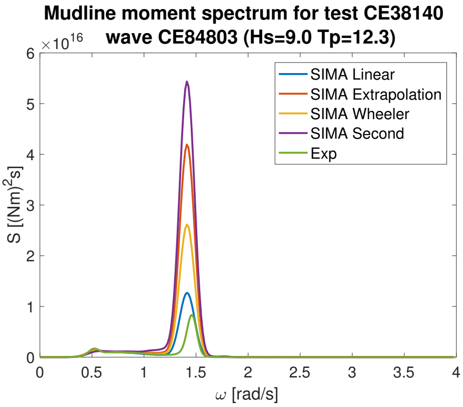

Figure B.81: Mudline moment spectra for the four different simulated wave kinematics models compared to the experimental test. Simulations with damping ratio 0.47%.

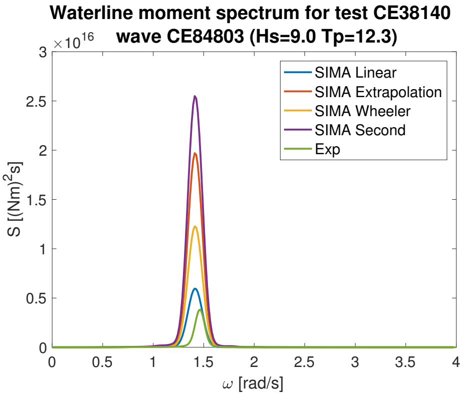

Figure B.82: Waterline moment spectra for the four different simulated wave kinematics models compared to the experimental test. Simulations with damping ratio 0.47%.

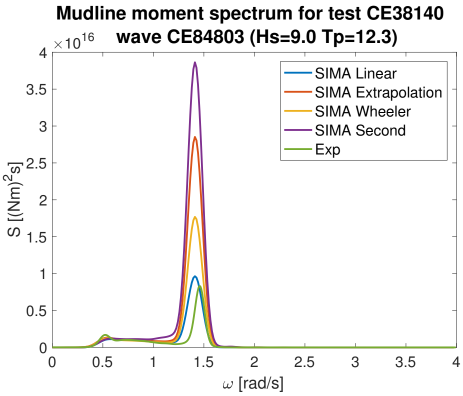

Figure B.83: Mudline moment spectra for the four different simulated wave kinematics models compared to the experimental test. Simulations with damping ratio 0.68%.

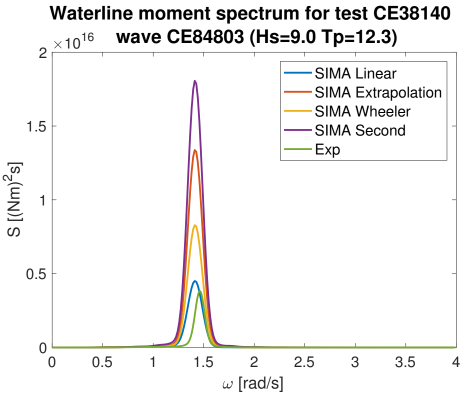

Figure B.84: Waterline moment spectra for the four different simulated wave kinematics models compared to the experimental test. Simulations with damping ratio 0.68%.

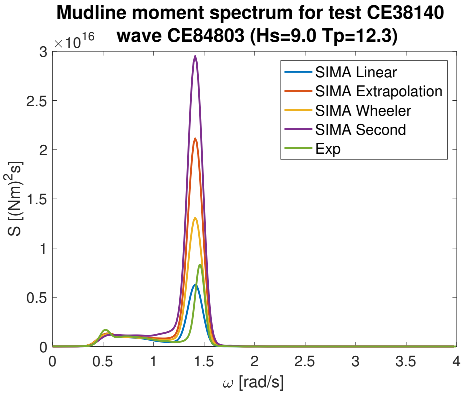

Figure B.85: Mudline moment spectra for the four different simulated wave kinematics models compared to the experimental test. Simulations with damping ratio 0.89%.

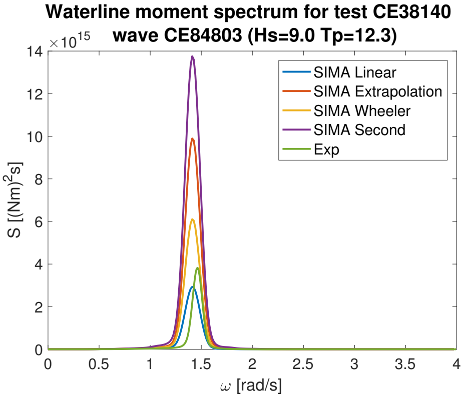

Figure B.86: Waterline moment spectra for the four different simulated wave kinematics models compared to the experimental test. Simulations with damping ratio 0.89%.

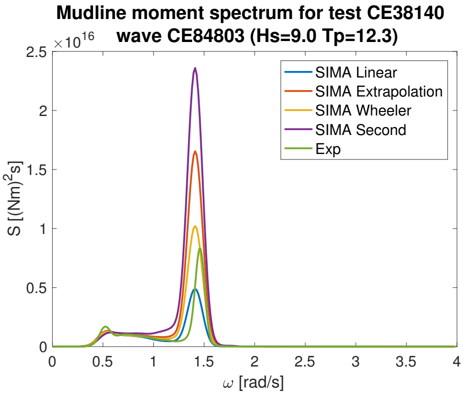

Figure B.87: Mudline moment spectra for the four different simulated wave kinematics models compared to the experimental test. Simulations with damping ratio 1.10%.

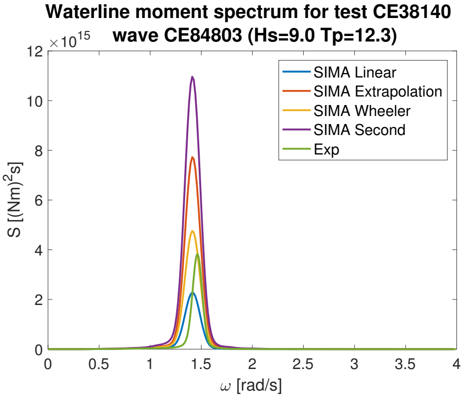

Figure B.88: Waterline moment spectra for the four different simulated wave kinematics models compared to the experimental test. Simulations with damping ratio 1.10%.

B.12 Spectra for Test No. 38150

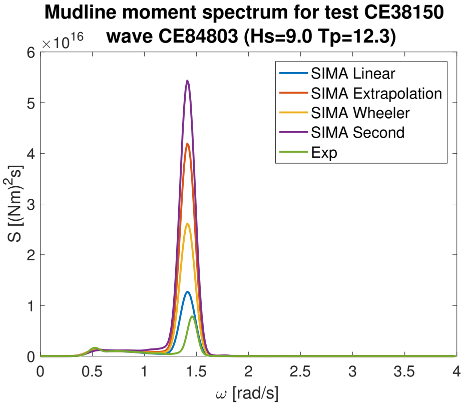

Figure B.89: Mudline moment spectra for the four different simulated wave kinematics models compared to the experimental test. Simulations with damping ratio 0.47%.

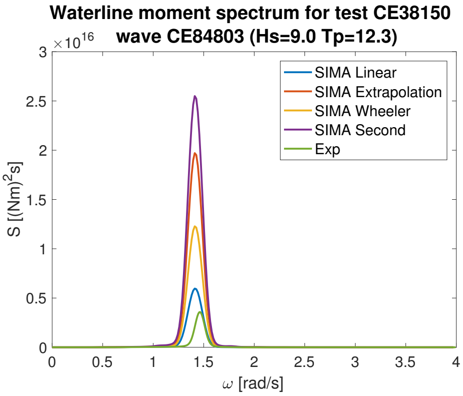

Figure B.90: Waterline moment spectra for the four different simulated wave kinematics models compared to the experimental test. Simulations with damping ratio 0.47%.

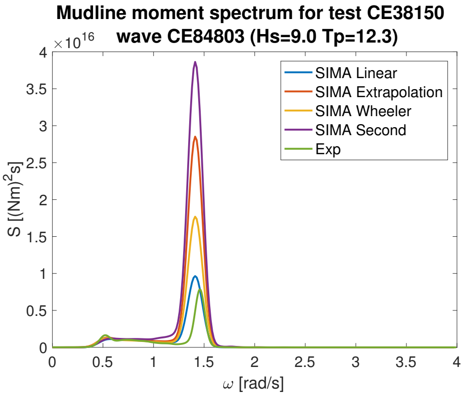

Figure B.91: Mudline moment spectra for the four different simulated wave kinematics models compared to the experimental test. Simulations with damping ratio 0.68%.

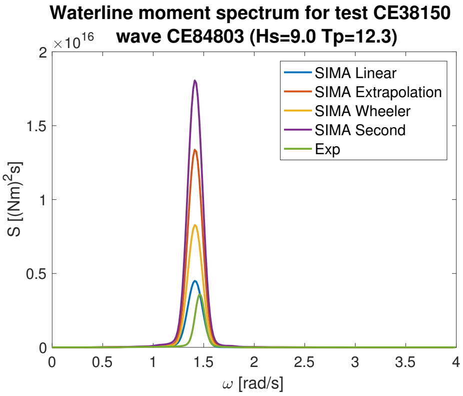

Figure B.92: Waterline moment spectra for the four different simulated wave kinematics models compared to the experimental test. Simulations with damping ratio 0.68%.

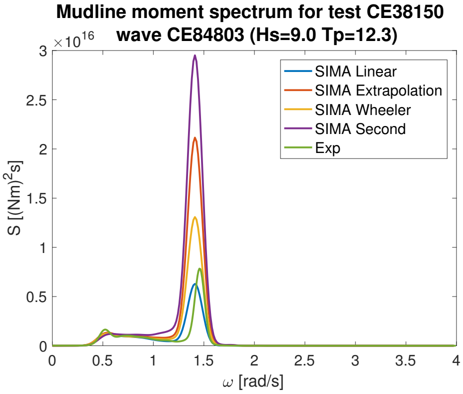

Figure B.93: Mudline moment spectra for the four different simulated wave kinematics models compared to the experimental test. Simulations with damping ratio 0.89%.

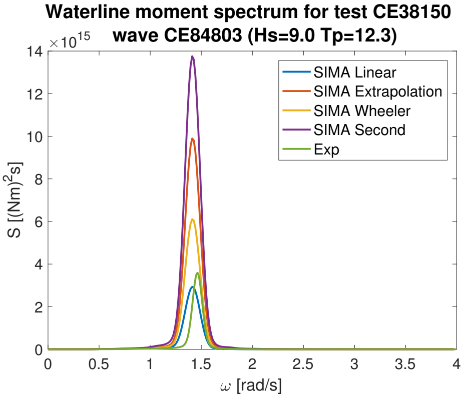

Figure B.94: Waterline moment spectra for the four different simulated wave kinematics models compared to the experimental test. Simulations with damping ratio 0.89%.

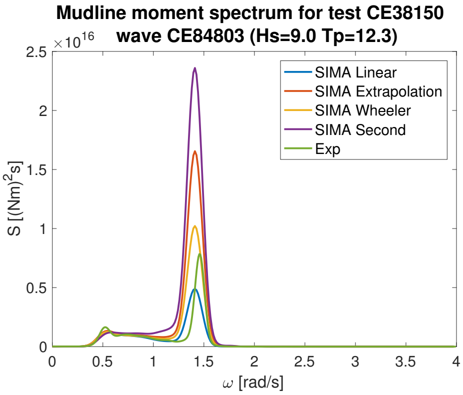

Figure B.95: Mudline moment spectra for the four different simulated wave kinematics models compared to the experimental test. Simulations with damping ratio 1.10%.

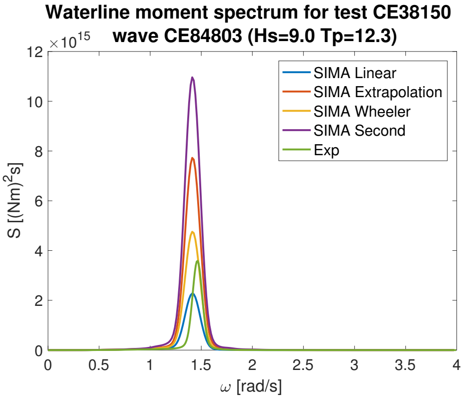

Figure B.96: Waterline moment spectra for the four different simulated wave kinematics models compared to the experimental test. Simulations with damping ratio 1.10%.

B.13 Spectra for Test No. 38160

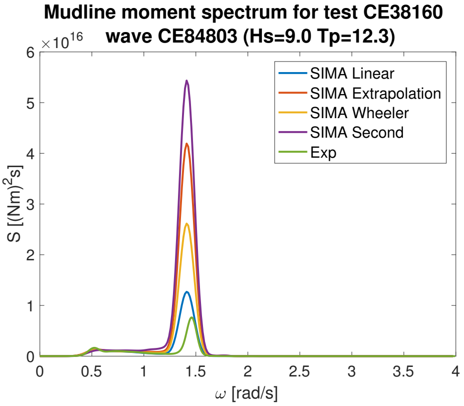

Figure B.97: Mudline moment spectra for the four different simulated wave kinematics models compared to the experimental test. Simulations with damping ratio 0.47%.

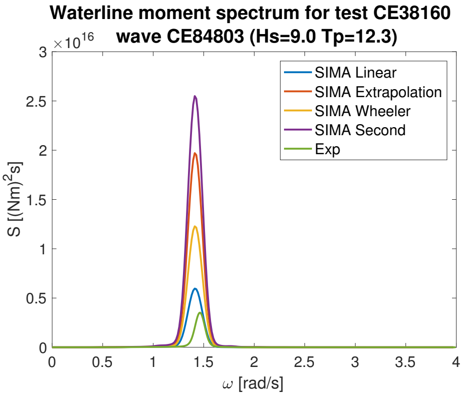

Figure B.98: Waterline moment spectra for the four different simulated wave kinematics models compared to the experimental test. Simulations with damping ratio 0.47%.

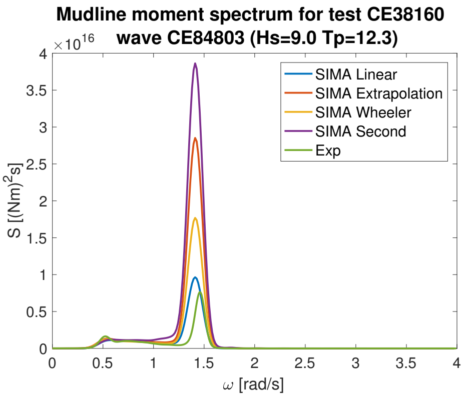

Figure B.99: Mudline moment spectra for the four different simulated wave kinematics models compared to the experimental test. Simulations with damping ratio 0.68%.

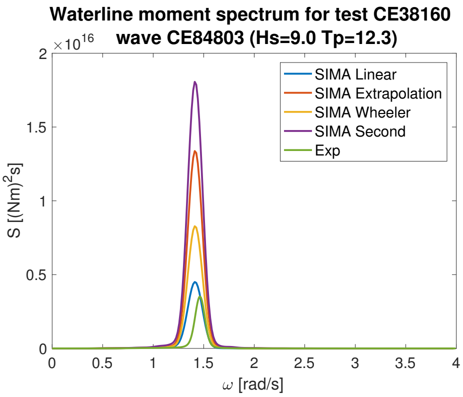

Figure B.100: Waterline moment spectra for the four different simulated wave kinematics models compared to the experimental test. Simulations with damping ratio 0.68%.

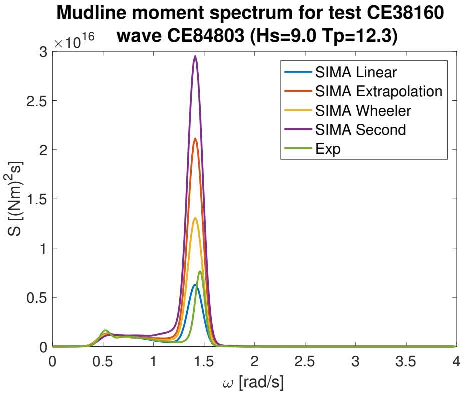

Figure B.101: Mudline moment spectra for the four different simulated wave kinematics models compared to the experimental test. Simulations with damping ratio 0.89%.

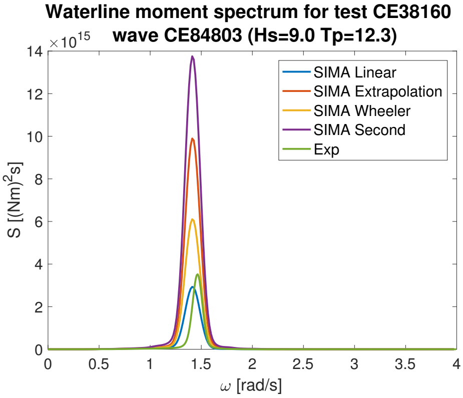

Figure B.102: Waterline moment spectra for the four different simulated wave kinematics models compared to the experimental test. Simulations with damping ratio 0.89%.

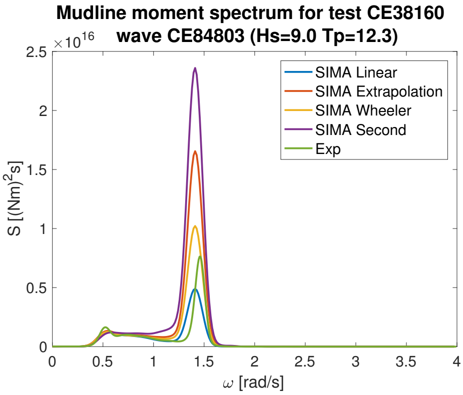

Figure B.103: Mudline moment spectra for the four different simulated wave kinematics models compared to the experimental test. Simulations with damping ratio 1.10%.

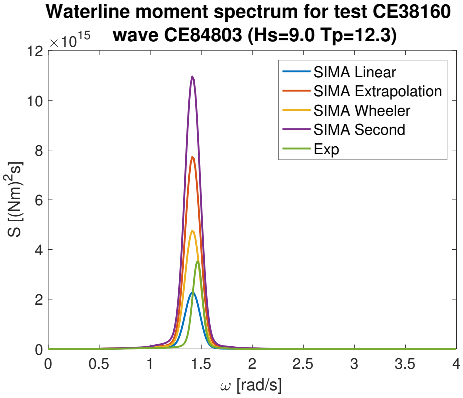

Figure B.104: Waterline moment spectra for the four different simulated wave kinematics models compared to the experimental test. Simulations with damping ratio 1.10%.

B.14 Spectra for Test No. 38170

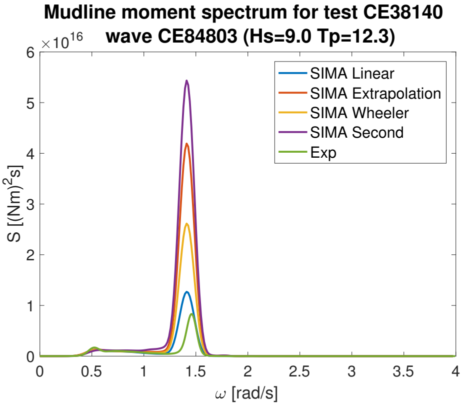

Figure B.105: Mudline moment spectra for the four different simulated wave kinematics models compared to the experimental test. Simulations with damping ratio 0.47%.

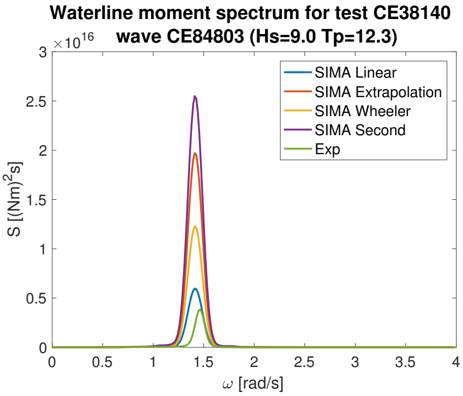

Figure B.106: Waterline moment spectra for the four different simulated wave kinematics models compared to the experimental test. Simulations with damping ratio 0.47%.

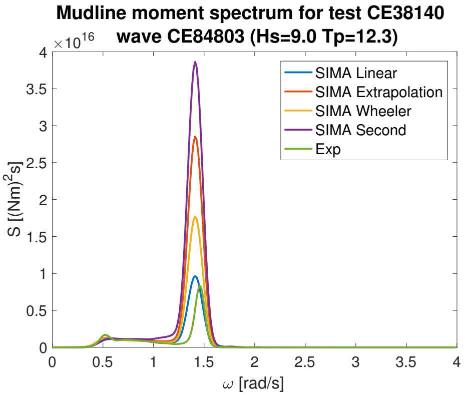

Figure B.107: Mudline moment spectra for the four different simulated wave kinematics models compared to the experimental test. Simulations with damping ratio 0.68%.

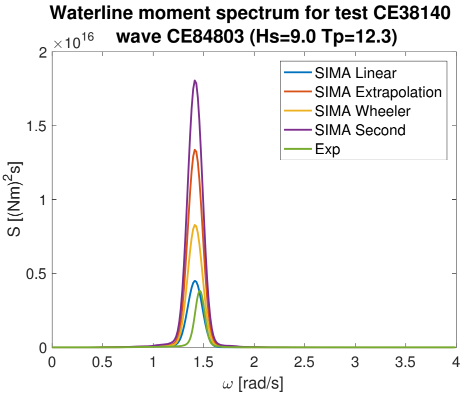

Figure B.108: Waterline moment spectra for the four different simulated wave kinematics models compared to the experimental test. Simulations with damping ratio 0.68%.

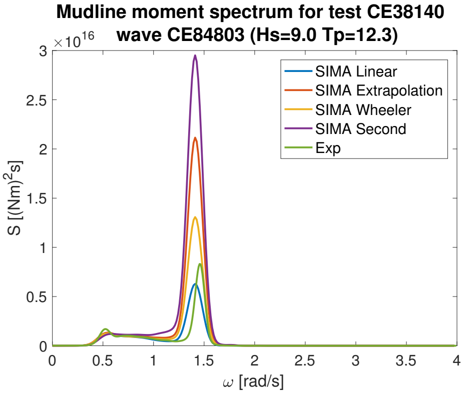

Figure B.109: Mudline moment spectra for the four different simulated wave kinematics models compared to the experimental test. Simulations with damping ratio 0.89%.

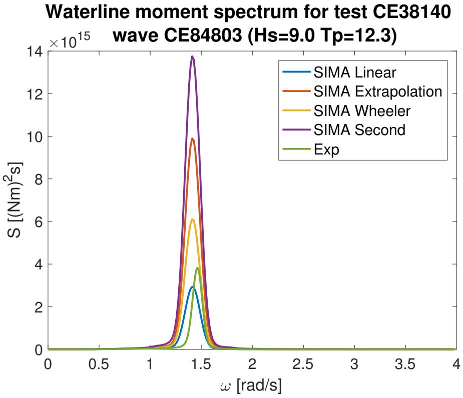

Figure B.110: Waterline moment spectra for the four different simulated wave kinematics models compared to the experimental test. Simulations with damping ratio 0.89%.

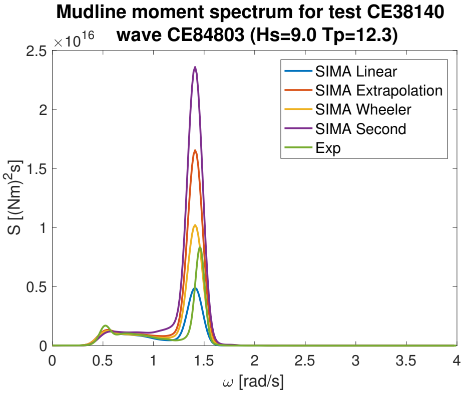

Figure B.111: Mudline moment spectra for the four different simulated wave kinematics models compared to the experimental test. Simulations with damping ratio 1.10%.

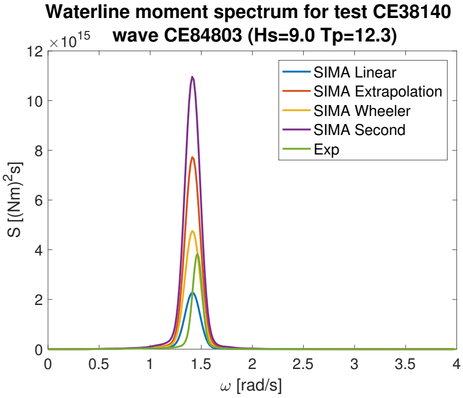

Figure B.112: Waterline moment spectra for the four different simulated wave kinematics models compared to the experimental test. Simulations with damping ratio 1.10%.

B.15 Spectra for Test No. 38180

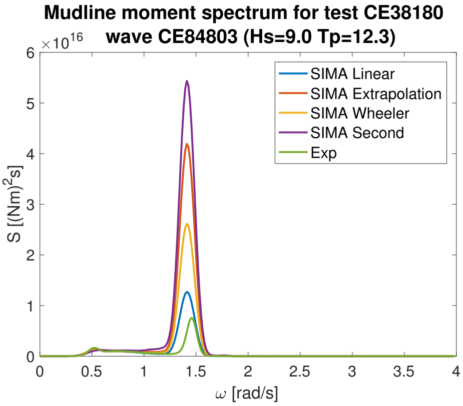

Figure B.113: Mudline moment spectra for the four different simulated wave kinematics models compared to the experimental test. Simulations with damping ratio 0.47%.

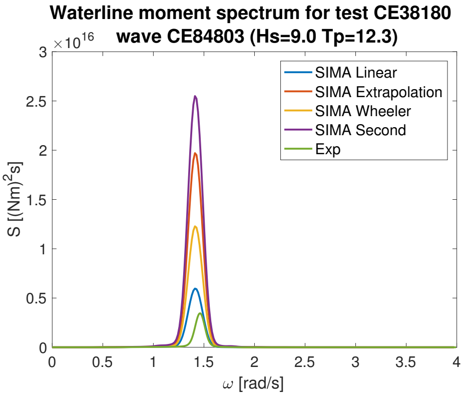

Figure B.114: Waterline moment spectra for the four different simulated wave kinematics models compared to the experimental test. Simulations with damping ratio 0.47%.

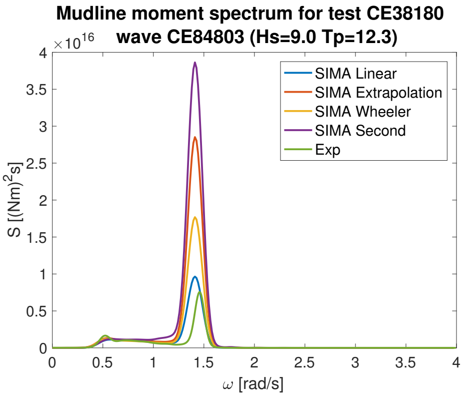

Figure B.115: Mudline moment spectra for the four different simulated wave kinematics models compared to the experimental test. Simulations with damping ratio 0.68%.

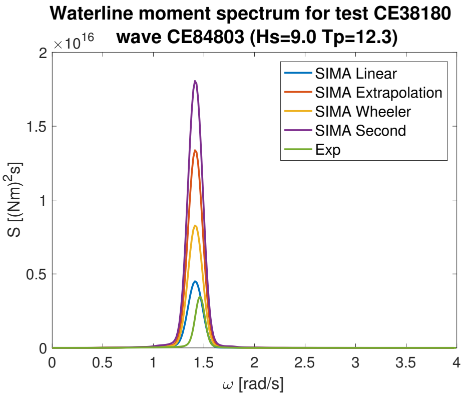

Figure B.116: Waterline moment spectra for the four different simulated wave kinematics models compared to the experimental test. Simulations with damping ratio 0.68%.

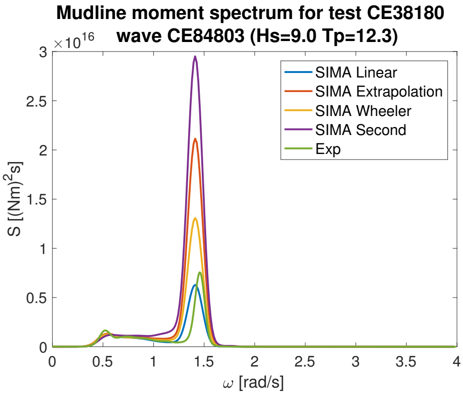

Figure B.117: Mudline moment spectra for the four different simulated wave kinematics models compared to the experimental test. Simulations with damping ratio 0.89%.

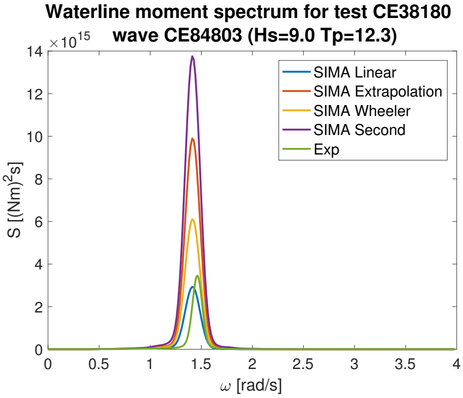

Figure B.118: Waterline moment spectra for the four different simulated wave kinematics models compared to the experimental test. Simulations with damping ratio 0.89%.

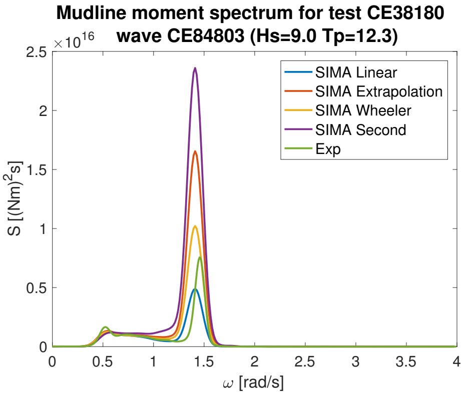

Figure B.119: Mudline moment spectra for the four different simulated wave kinematics models compared to the experimental test. Simulations with damping ratio 1.10%.

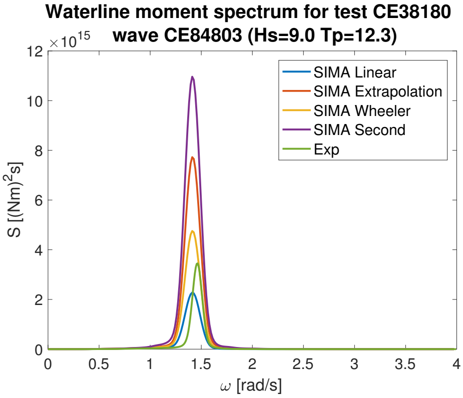

Figure B.120: Waterline moment spectra for the four different simulated wave kinematics models compared to the experimental test. Simulations with damping ratio 1.10%.

B.16 Spectra for Test No. 39010

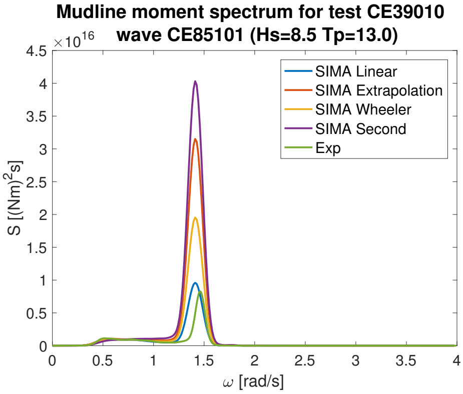

Figure B.121: Mudline moment spectra for the four different simulated wave kinematics models compared to the experimental test. Simulations with damping ratio 0.47%.

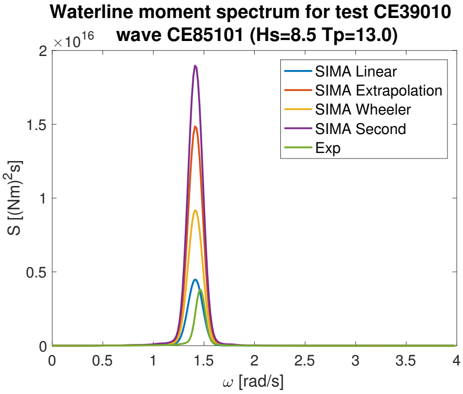

Figure B.122: Waterline moment spectra for the four different simulated wave kinematics models compared to the experimental test. Simulations with damping ratio 0.47%.

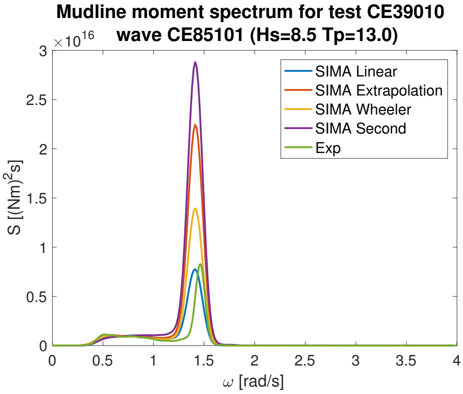

Figure B.123: Mudline moment spectra for the four different simulated wave kinematics models compared to the experimental test. Simulations with damping ratio 0.68%.

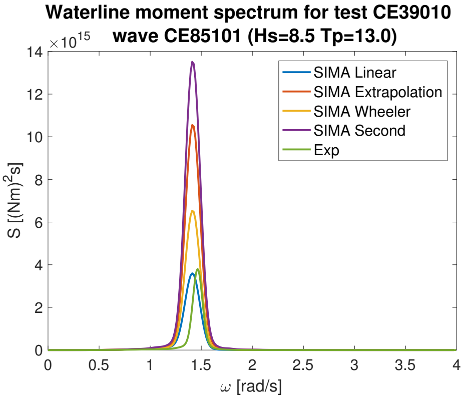

Figure B.124: Waterline moment spectra for the four different simulated wave kinematics models compared to the experimental test. Simulations with damping ratio 0.68%.

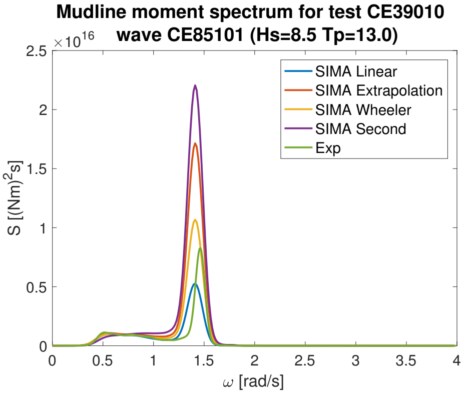

Figure B.125: Mudline moment spectra for the four different simulated wave kinematics models compared to the experimental test. Simulations with damping ratio 0.89%.

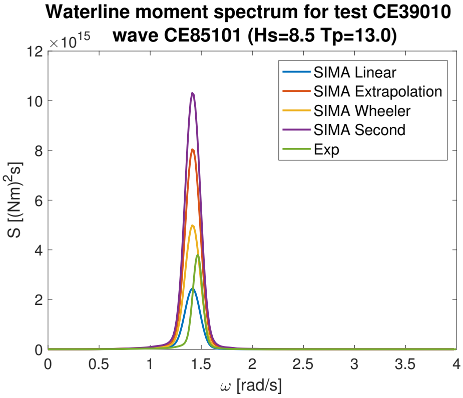

Figure B.126: Waterline moment spectra for the four different simulated wave kinematics models compared to the experimental test. Simulations with damping ratio 0.89%.

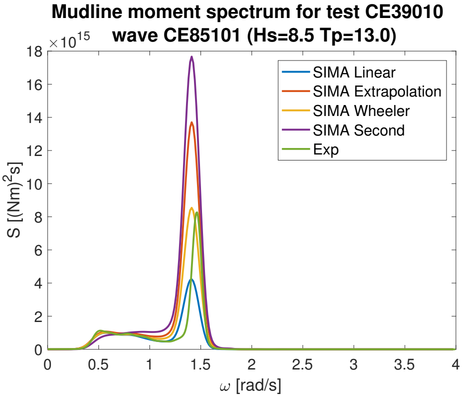

Figure B.127: Mudline moment spectra for the four different simulated wave kinematics models compared to the experimental test. Simulations with damping ratio 1.10%.

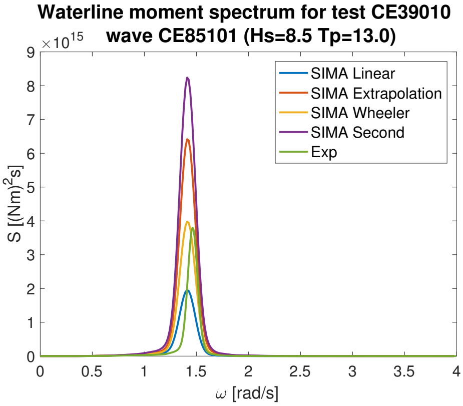

Figure B.128: Waterline moment spectra for the four different simulated wave kinematics models compared to the experimental test. Simulations with damping ratio 1.10%.

Appendix C

Ringing Events

C.1 Ringing Event in Test No. 37010

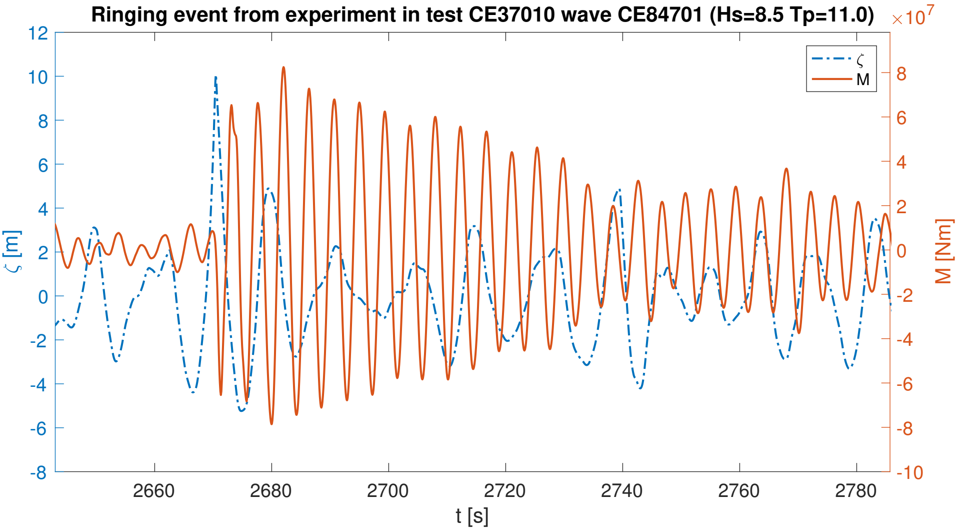

Figure C.1: Surface elevation (blue) and waterline moment (red), showing a ringing event from the experiments in test number 37010

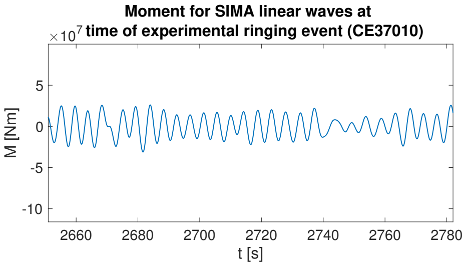

Figure C.2: Waterline moment from simulation with linear theory at the time of the ringing event from the experiments in test number 37010

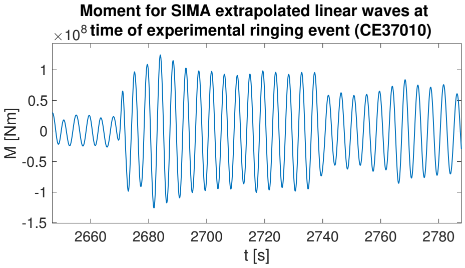

Figure C.3: Waterline moment from simulation with simple extrapolation at the time of the ringing event from the experiments in test number 37010

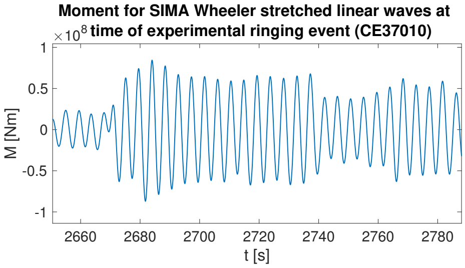

Figure C.4: Waterline moment from simulation with Wheeler stretching at the time of the ringing event from the experiments in test number 37010

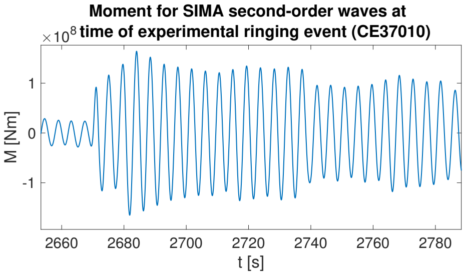

Figure C.5: Waterline moment from simulation with second-order theory at the time of the ringing event from the experiments in test number 37010

C.2 Ringing Event in Test No. 38030

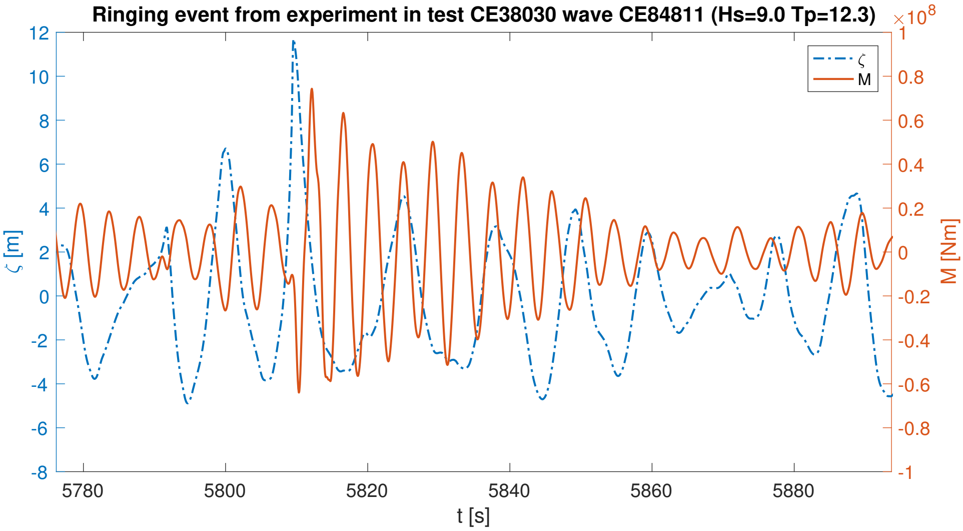

Figure C.6: Surface elevation (blue) and waterline moment (red), showing a ringing event from the experiments in test number 38030

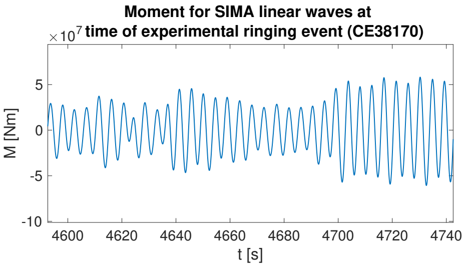

Figure C.7: Waterline moment from simulation with linear theory at the time of the ringing event from the experiments in test number 38030

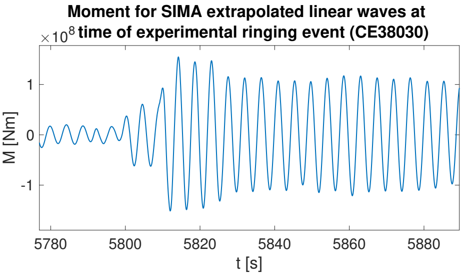

Figure C.8: Waterline moment from simulation with simple extrapolation at the time of the ringing event from the experiments in test number 38030

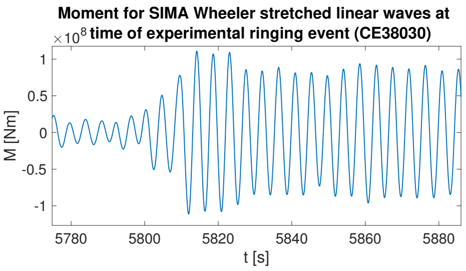

Figure C.9: Waterline moment from simulation with Wheeler stretching at the time of the ringing event from the experiments in test number 38030

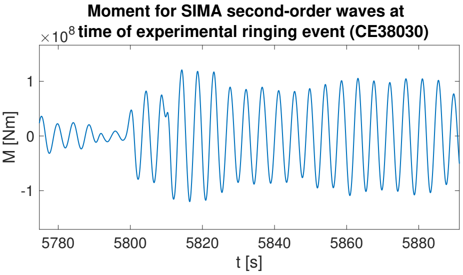

Figure C.10: Waterline moment from simulation with second-order theory at the time of the ringing event from the experiments in test number 38030

C.3 Ringing Event in Test No. 38170

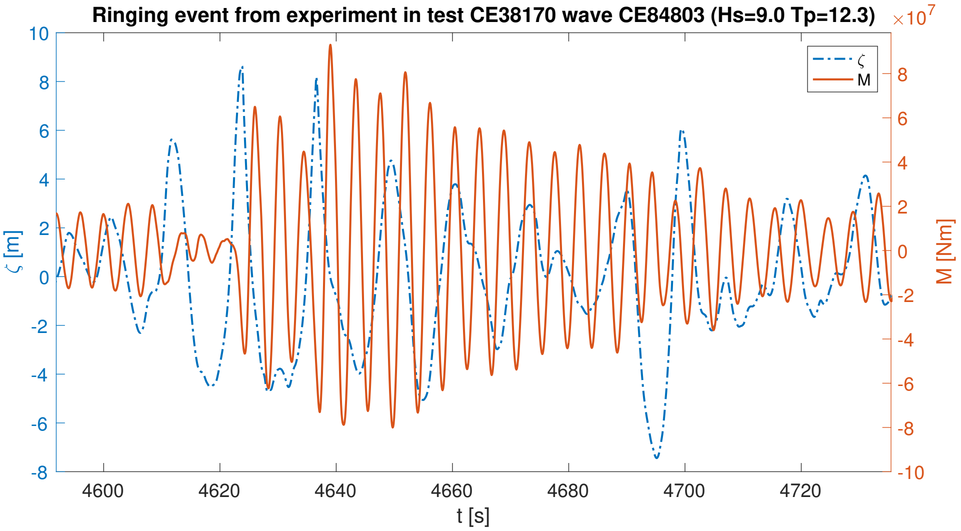

Figure C.11: Surface elevation (blue) and waterline moment (red), showing a ringing event from the experiments in test number 38170

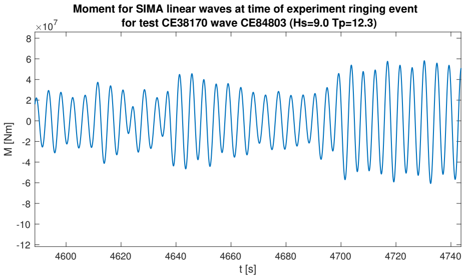

Figure C.12: Waterline moment from simulation with linear theory at the time of the ringing event from the experiments in test number 38170

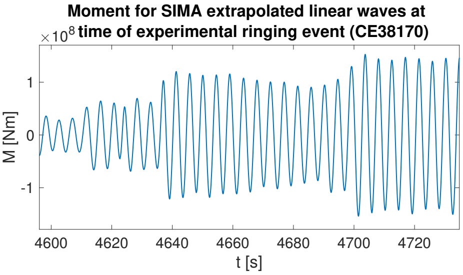

Figure C.13: Waterline moment from simulation with simple extrapolation at the time of the ringing event from the experiments in test number 38170

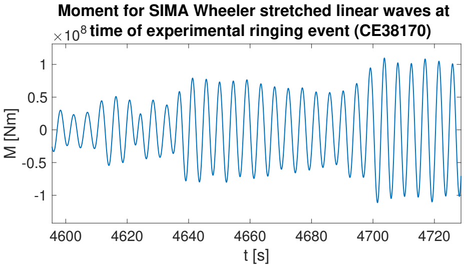

Figure C.14: Waterline moment from simulation with Wheeler stretching at the time of the ringing event from the experiments in test number 38170

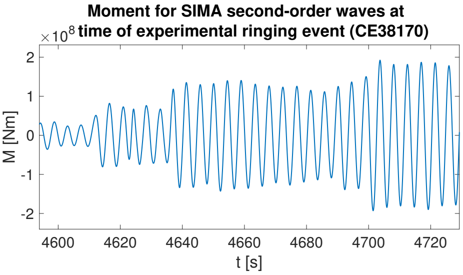

Figure C.15: Waterline moment from simulation with second-order theory at the time of the ringing event from the experiments in test number 38170

C.4 Ringing Event in Test No. 38180

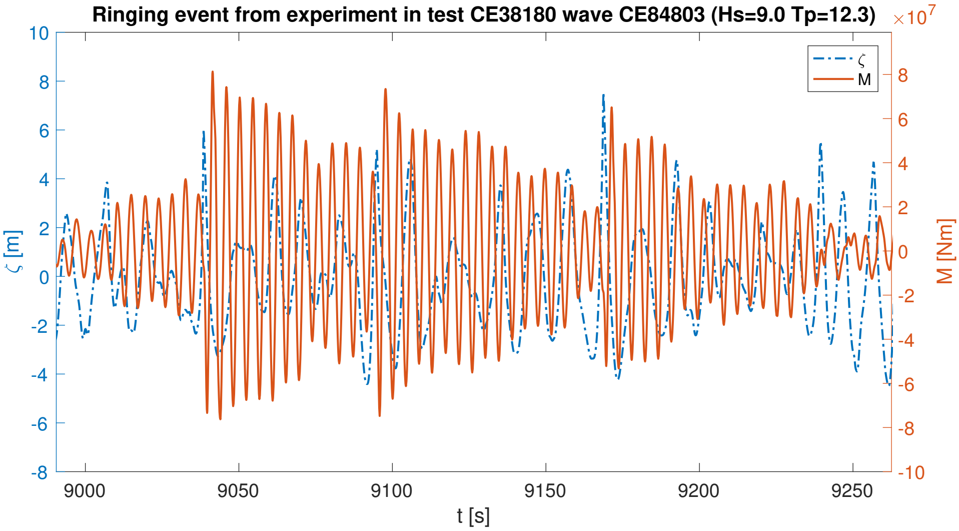

Figure C.16: Surface elevation (blue) and waterline moment (red), showing a series of ringing events the experiments in test number 38180

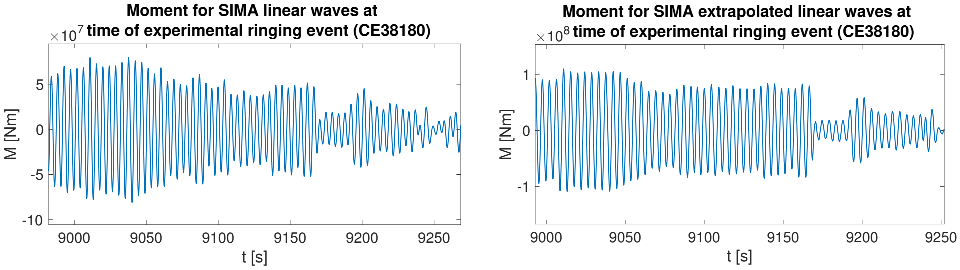

Figure C.17: Waterline moment from simulation with linear theory at the time of the ringing event from the experiments in test number 38180

Figure C.18: Waterline moment from simulation with simple extrapolation at the time of the ringing event from the experiments in test number 38180

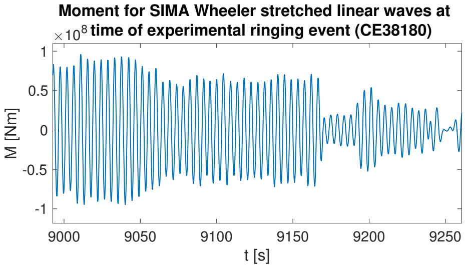

Figure C.19: Waterline moment from simulation with Wheeler stretching at the time of the ringing event from the experiments in test number 38180

C.5 Ringing Event in Test No. 38110

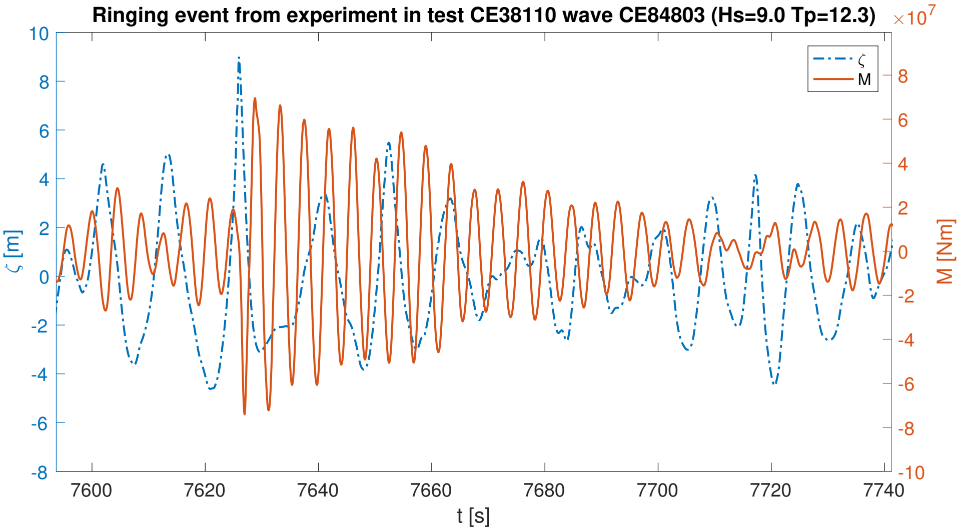

Figure C.20: Surface elevation (blue) and waterline moment (red), showing a series of ringing events the experiments in test number 38110

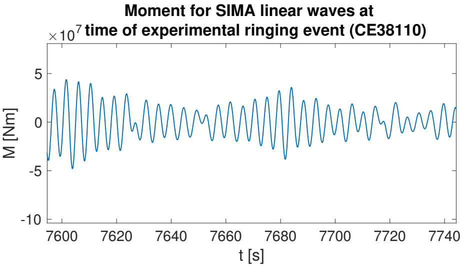

Figure C.21: Waterline moment from simulation with linear theory at the time of the ringing event from the experiments in test number 38110

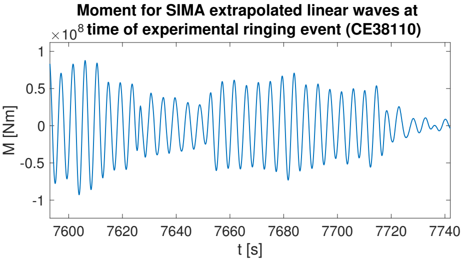

Figure C.22: Waterline moment from simulation with simple extrapolation at the time of the ringing event from the experiments in test number 38110

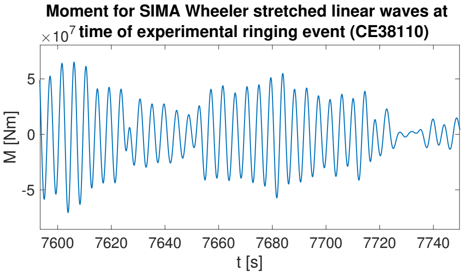

Figure C.23: Waterline moment from simulation with Wheeler stretching at the time of the ringing event from the experiments in test number 38110